Fabricating Dual-Gated 2D CrSBr Devices to Investigate Nonlinear Transport Effects

CNF Summer Student: Calvin Chiu Student Affiliation: Physics, The University of Texas at Austin

Summer Program(s): 2025 Cornell NanoScale Facility Research Experience for Undergraduates (CNF REU) Program

Principal Investigator(s): Dan Ralph, Physics, Cornell University

Mentor(s): Bozo Vareskic, Physics, Cornell University

Primary Source(s) of Research Funding: Center for Energy Efficient Magnonics, funded by the U.S. Department of

Energy, Office of Science, Basic Energy Sciences under Award #DE-AC02-76SF00515

Contact: dcr14@cornell.edu, bv227@cornell.edu, ckc2398@my.utexas.edu

Summer Program Website(s): https://cnf.cornell.edu/education/reu

Primary CNF Tools Used: Zeiss Supra SEM, Nabity NPGS Nanometer Pattern Generator System, CVC SC4500 Odd-

Hour Evaporator, Oxford 81 RIE

Abstract:

The tremendous interest in 2D van der Waals (vdW) materials in condensed matter physics has led to studies on magnetic materials for potential applications in spintronics and quantum information. CrSBr is a magnetic semiconductor that has garnered interest due to its ability to be exfoliated to the 2D limit. However, transport effects in 2D CrSBr such as the nonlinear Hall effect have yet to be explored. In this project, we aim to fabricate functioning dual-gated CrSBr devices and investigate the existence of a nonlinear Hall effect when subjecting the devices to varying parameters.

Summary of Research:

Two-dimensional materials have generated enormous research interest, and the discovery of new materials and ordered phases continues to expand the scope of the field. One category of 2D materials includes van der Waals (vdW) magnets such as chromium sulfur bromide (CrSBr) [1]. CrSBr is particularly interesting from an experimental standpoint, as it is more air-stable compared to other 2D magnetic materials and can be exfoliated relatively easily to the monolayer limit [2].

CrSBr is a magnetic semiconductor exhibiting A-type antiferromagnetic structure; the magnetic moments within a layer are aligned ferromagnetically (same direction) in the plane, while the magnetic moments in adjacent layers are aligned antiferromagnetically (opposite direction). CrSBr also exhibits intriguing electronic and magnetic anisotropies. Due to CrSBr's electronic structure, particularly the orbital composition of its conduction band, electron transport is massively favored along one direction, with the conductivity along the b-axis (σ b) being up to 10,000 times larger than σ a [2, 3]. Moreover, 2D CrSBr can exhibit strong coupling between its electronic and magnetic structure, including exciton-magnon coupling in twisted bilayer CrSBr [2, 4].

Although various studies have been conducted on CrSBr, there has yet to be definitive measurements regarding

a quantum nonlinear Hall effect (NLHE). NLHE is an extension of the classical Hall effect, where a transverse Hall voltage (VH) is induced when a material carrying current is exposed to a perpendicular magnetic field. However, in NHLE, an applied electric field can induce a nonlinear VH, even without introducing a magnetic field. NHLE has been observed and predicted in various materials [5, 6], but we aim to experimentally investigate the NHLE in few-layer CrSBr.

Methods. In this project, we focused on fabricating dual-gated CrSBr transistors for the purposes of investigating whether a nonlinear Hall effect exists, as well as its dependence on temperature, carrier density, and out of plane electric field. To do so, we conducted optimization trials and referenced previous research [5, 7, 8] to develop a working fabrication process, as outlined below:

- 1. Perform Scotch tape exfoliation onto blank silicon substrates for crystals of few-layer graphene (FLG) and hexagonal boron nitride (hBN). Search for clean \sim 40 μ m x 10 μ m FLG and \sim 50 μ m x 50 μ m x 70 μ m hBN flakes.
- **2.** Utilize PDMS viscoelastic stamping to place FLG-hBN on pre-prepared silicon substrates, leaving a segment of FLG exposed for the bottom gate (if convenient).
- **3.** Pattern inner electrodes (e.g. in a double Hall bar geometry) using KLayout and spin-coat substrates with PMMA A4 followed by PMMA A2.
- **4.** Expose/develop samples and deposit 8 nm of platinum using CNF tools, including the Zeiss Supra SEM, Nabity NPGS, and SC4500 Evaporator. Perform lift-off in acetone and tip-based cleaning using an atomic force microscope (Fig. 1).
- 5. In an oxygen- and water-free glove box, exfoliate and search for $\sim \! \! 10~\mu m$ x 5 μm few-layer CrSBr and more hBN flakes. Stamp CrSBr flakes such that the flake contacts all inner electrodes, and stamp hBN to cover all but the exposed FLG.
- **6.** Pattern openings to the inner electrodes. Spin-coat and expose/develop. Etch the exposed segments to remove the



Figure 1: Image of an example of device after step 4 of the fabrication process.

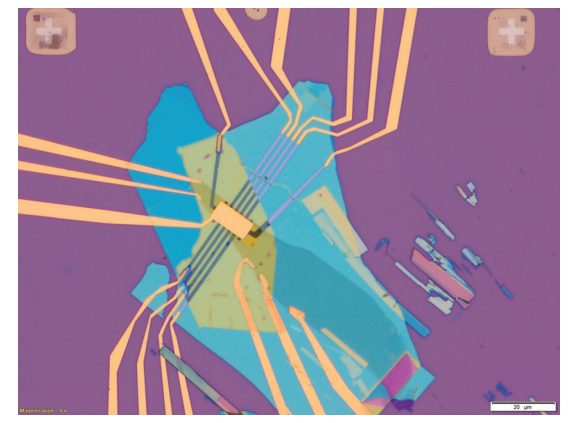


Figure 2: Image of an example device after the full fabrication process.

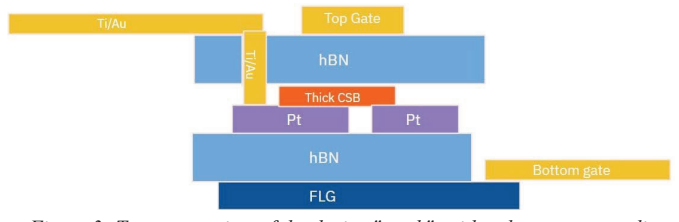


Figure 3: Transverse view of the device "stack", with colors corresponding to Figure 2.

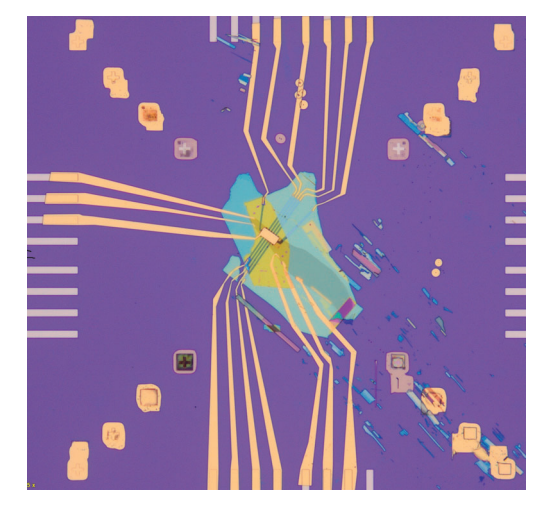


Figure 4: Zoomed-out image of Figure 2.

hBN using the Oxford 81 RIE.

7. Pattern outer electrodes, a top gate, and bottom gate(s) to connect to the pre-prepared bonding pads. Spin-coat, expose/develop, deposit 10 nm Ti/90 nm Au, and perform lift-off (Fig. 2 - 4).

Conclusions and Future Steps:

Through extensive testing and trial-and-error, we have established a working fabrication process for creating dualgated 2D CrSBr devices. Despite the supposed air stability of CrSBr, the exfoliation in the glove box and complete insulation by the top hBN were required to prevent the CrSBr from degrading and losing electrical contact after several hours. Our fabrication process may also apply to other airsensitive 2D materials with transport properties of interest.

With our obtained measurements, we aim to extract the conductivity tensors of few-layer CrSBr in the near future. Further studies can be conducted to verify the obtained results improve the fabrication efficiency

Acknowledgements:

Many thanks to the 2024 Cornell NanoScale Facility Research Experiences for Undergraduates (CNF REU) Program funded by the National Science Foundation under Grant No. NNCI-2025233, and the National Nanotechnology Coordinated Infrastructure. Special thanks to Prof. Dan Ralph and Bozo Vareskic for all of their guidance and support.

- Burch, K. S. et al. https://doi.org/10.1038/s41586-018-0631-z
- [2] Michael E. Ziebel et al. DOI: 10.1021/acs.nanolett.4c00624
- [3] Wu, F. et al. DOI: 10.1002/adma.202109759
- [4] Sun, Y. et al. DOI: 10.48550/arXiv.2506.10080
- [5] Chichinadze, D. V. et al. DOI: 10.48550/arXiv.2411.11156
- [6] Min L et al. DOI: 10.1038/s41467-023-35989-0
- [7] Sun, S. et al. DOI: 10.48550/arXiv.2507.15853
- [8] Bhatia, P. et al. DOI: 10.1016/S0968-4328(24)00164-1

Fabrication of Manhattan-style Josephson Junctions

CNF Summer Student: Gabriele Di Gianluca Student Affiliation: Physics, University of Florida

Summer Program(s): 2025 Cornell NanoScale Facility Research Experience for Undergraduates (CNF REU) Program

Principal Investigator(s): Valla Fatemi

Mentor(s): Simon Reinhardt, Maciej Olszewski, Lingda Kong Primary Source(s) of Research Funding: NORDTECH (SQ Fab)

Contact: vf82@cornell.edu, digianlucag@ufl.edu

Summer Program Website(s): https://cnf.cornell.edu/education/reu

Research Group Website: https://fatemilab.aep.cornell.edu/

Primary CNF Tools Used: Angstrom-Q, JEOL 6300 E-beam Lithography System, Zeiss Ultra SEM, GCA AS200 i-line

Stepper, Heidelberg DWL2000, AJA Sputter 1

Abstract:

Qubits based on superconducting quantum circuits are one of the most promising platforms for quantum computing [1]. The critical component of these superconducting qubits is the Josephson Junction. We use a Josephson Junction which is a superconductor-insulator-superconductor interface that relies on the tunneling of Cooper pairs through the thin insulating barrier [1]. Once below the critical temperature of the superconducting material, the Josephson Junction can now conduct a current without any applied voltage, exhibiting the Josephson Effect. This nonlinear current creates the key anharmonicity needed to create a qubit [2]. In this research, we fabricate Manhattan-style Josephson Junctions in the Angstrom-Q and characterize the oxidation process.

Summary of Research:

The main two types of Josephson Junctions are Dolan and Manhattan-style. Dolan-style junctions rely on a shadow evaporation method where Electron-Beam lithography on the JEOL 6300 is performed onto a PMMA/MMA resist stack. During this lithography, a bridge is defined, and two evaporations are performed at different angles with an oxidation in between. This overlap between the two evaporation defines our junction area, a key factor in determining the properties of the Josephson Junction. The main downside to this style is that the bridge used is fragile and can frequently collapse, therefore halting the fabrication process. Additionally, the bridge can vary between lithography runs due to resist thickness. This inconsistency in the bridge leads to an inconsistency in junction area, which changes the parameters of the qubit. In an effort to increase reproducibility in our qubit fabrication, we began to fabricate Manhattan-style Josephson Junctions using the new Angstrom-Quantum evaporator, designed specifically for this purpose. Manhattan-style junctions (Figure 1) are a bridge-less technique that use a similar PMMA/MMA resist stack, but instead rely on an evaporation into two different trenches [3]. As opposed to Dolan-style junctions, in this case, the area of our junctions is only determined by the lithography. This, coupled with the fact that there is no

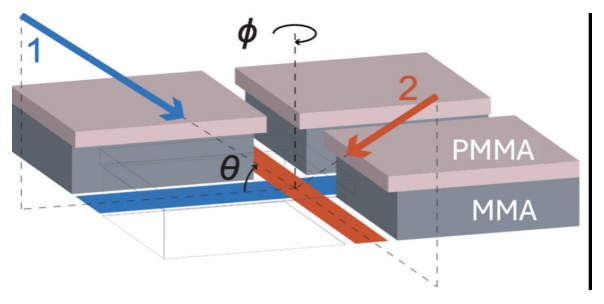


Figure 1:

bridge involved, increases our reproducibility between fabrication runs.

The main reason we care about the area of our junction is that it affects critical current, I_c, the maximum current the junction can hold before returning to a nonzero resistance state. The critical current is given by the Ambegaokar–Baratoff relation (Figure 2a), in which the superconducting gap of Aluminum is known and the normal state resistance, R_n, can be obtained by a room temperature two-probe resistance measurement. From the critical current, we can then determine the Josephson Energy, E_J (Figure 2b). E_J is a key term in the Hamiltonian of our circuit and determines the circuit dynamics, primarily our qubit frequency, a critical

a) b)
$$I_{c}=\frac{\pi\Delta}{2eR_{n}} \qquad \qquad E_{J}=\frac{\Phi_{0}}{2\pi}I_{c} \propto I_{c}$$

$$\Delta=\text{Superconducting gap} \qquad \qquad \text{Magnetic flux quantum: } \Phi_{0}=\frac{h}{2e}=\text{constant}$$

$$R_{n}=\text{Normal state resistance}$$

Figure 2:

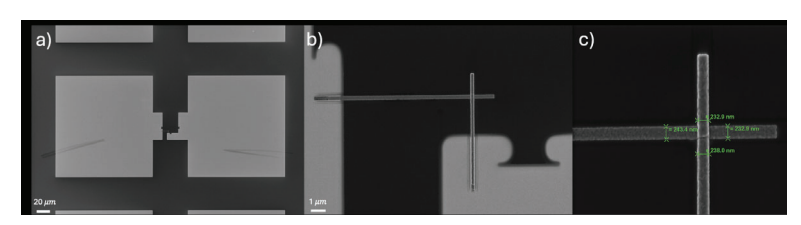


Figure 3:

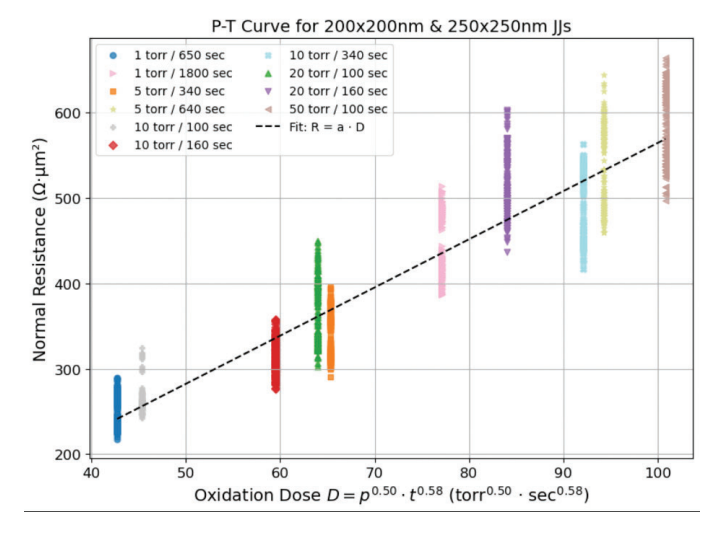


Figure 4:

number in benchmarking qubit performance [1].

Our fabrication process began by doing a standard HF clean of our 100mm Si wafer in order to remove the native oxide layer. Then we spun on a LOR 3A and S1813 photoresist stack before patterning bonds pads using the i-line stepper on a mask written in the Heidelberg DWL2000. After developing on a Hamatech automatic developer, we deposited Ti-seeded Pt using the AJA 1 Sputter tool. The 5nm of Ti acts as an adhesion layer for the 80nm of Pt which does not naturally oxidize, making it compatible with our probe station. After doing lift-off in Remover PG overnight, we spun on a PMMA/MMA e-beam resist stack. This allowed us to pattern our Josephson Junctions in the JEOL 6300 Electron-Beam Lithography system. Onto our wafer, we patterned 100 200x200nm and 100 250x250nm junctions. Before depositing, we cleaved our wafer into chips and developed them in IPA:DI (3:1) for 2 minutes. Once loaded into the Angstrom-Q, we do an in-situ argon milling to remove any unwanted oxide that could prevent poor contact. We then deposit 20nm of Al for our bottom electrode at a rate of 2 A/s and a chamber pressure <5e-8. Our oxidation step varies with pressures from 1 to 50 torr and 1 to 30 minutes. Our top electrode is 70nm of Al and is deposited at a similar chamber pressure as the bottom electrode. Before taking our sample out, we do a post-oxidation step instead of letting the sample oxidize arbitrarily in atmosphere. Then we do lift-off in heated DMSO at 80-90 C overnight. Finally, we measure room temperature resistance using a Keithley SourceMeter and a probe station with Tungsten tips. After probing resistance,

SEM images were taken on the Zeiss Ultra SEM in order to calculate the area of our junctions and evaluate the success of lift-off (Figure 3).

We iterated on our fabrication many times in order to produce 20 data points across JJs with a 20nm bottom electrode. With this data, we plotted the normal resistance, resistance of our junctions times the area, versus the oxidation dose, a combination of the pressure and time of the oxidation. The value of the exponents assigned to pressure and time and the linear fit to our data was optimized (Figure 4). We observe our data aligns with our linear fit and with previous work [4]. We also compute the variability of junction resistance across a die and observe a variance <5%, which is acceptable for qubit devices.

Conclusions and Future Steps:

We successfully demonstrated the fabrication of Manhattan-style Josephson Junctions in the Angstrom-Q. We also characterized and optimized the fabrication process by constructing a pressure-time curve. This curve will allow us to determine the oxidation dose necessary to obtain a junction of a desired resistance with minimal trial and error.

The next step will be move away from Dolanstyle junctions and incorporate Manhattan-style Josephson Junctions into our qubit fabrication process. As we do multiple fabrication runs, we will see whether the junction properties are reproducible and whether Manhattan junctions have any advantage over Dolan junctions. Another possibility will be to do an aging study of Josephson Junctions. This would involve measuring the resistance of junctions over at least a month and observing how the resistance changes over time.

- Rasmussen et al., "Superconducting Circuit Companion---an Introduction with Worked Examples."
- [2] Krantz et al., "A Quantum Engineer's Guide to Superconducting Qubits."
- [3] Kreikebaum et al., "Improving Wafer-Scale Josephson Junction Resistance Variation in Superconducting Quantum Coherent Circuits."
- [4] Zeng et al., "Direct Observation of the Thickness Distribution of Ultra Thin AlOx Barriers in Al/AlOx/Al Josephson Junctions."

Domain Switching in Twisted Double Bilayer Graphene

CNF Summer Student: Peter Golemis

Student Affiliation: Physics and Electrical & Computer Engineering, University of Illinois Urbana-Champaign

Summer Program(s): 2025 Cornell NanoScale Facility Research Experience for Undergraduates (CNF REU) Program

Principal Investigator(s): Kenji Yasuda

Mentor(s): Daniel Brandon

Primary Source(s) of Research Funding: National Science Foundation under Grant No. NNCI-2025233)

Contact: kenji.yasuda@cornell.edu, db923@cornell.edu, golemis3@illinois.edu

Summer Program Website(s): https://cnf.cornell.edu/education/reu

Research Group Website: https://www.yasudalab.org/home

Primary CNF Tools Used: Oxford 81 RIE, SC4500 Odd-Hour Evaporator, Zeiss Supra SEM, Nabity Nanometer Pattern

Generator System

Abstract:

For over two decades, the properties of two-dimensional (2D) graphene films have been rigorously explored, exhibiting a variety of profound electronic phenomena [1]. Few-layer graphene has received great attention due to the wide range of electronic band structures realized across its various stacking orders [2]. Different coexisting stacking orders are obtained by precisely controlling the twist angle between two bilayer graphene flakes, generating Bernal (ABAB) and rhombohedral (ABCA) domains. In this work, we obtain transport measurements of small-angle twisted double bilayer graphene (TDBG) Hall bar devices with this domain structure, which exhibit gate-tunable domain switching. This platform enables the observation of the interplay between domain switching and the electronic properties of Bernal and rhombohedral graphene.

Summary of Research:

Device Fabrication:

Bernal (Fig. 1a) and rhombohedral (Fig. 1b) ordered graphene are two possible stacking configurations of four-layered graphene systems. Introducing a small twist angle between two bilayer graphene films enables the formation of large coexisting Bernal and rhombohedral domains. The electronic properties of small-angle TDBG are probed in double-gated stacks (Fig. 1c) constructed using a PDMS/PC dry transfer process. High- quality uniform gates consisting of a thin hexagonal boron nitride (hBN) dielectric and conducting graphite flake are used to tune the carrier density and out-of-plane displacement field through the TDBG. Initially, the bottom gate is stacked and placed onto a pre-patterned Si/SiO2 substrate (Fig. 1d). Mechanically exfoliated bilayer graphene flakes are then identified using optical

microscopy and cut into two pieces by applying a high-frequency alternating voltage to a conductive atomic force microscope (AFM) tip [3].

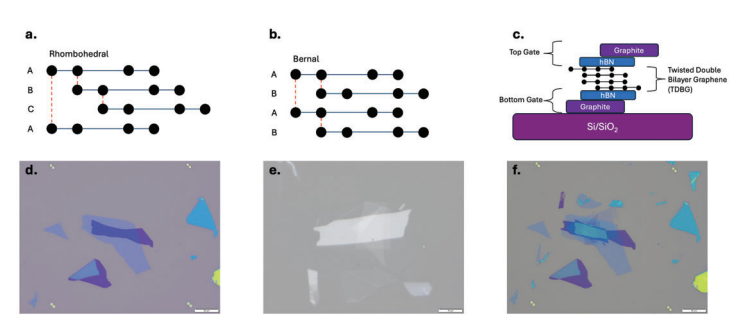


Figure 1: a,b, Visualization of rhombohedral and Bernal stacking orders in TDBG. c, Profile schematic of a double gated TDBG stack. d, Bottom gate placed on a pre-patterned chip. e, Complete top stack on PDMS/PC stamp. f, Complete stack consisting of a bottom gate (Fig. 1d) and top stack (Fig. 1e).

Scanning the conductive AFM tip over a graphene flake in a humid environment drives an anodic oxidation process to selectively remove regions of the flake with minimal induced strain on the crystal lattice. Implementing the dry transfer process, a top gate is fabricated separately by stacking graphite on top of a thin hBN flake. The first half of the bilayer graphene flake is stacked beneath the top gate, and the other half is rotated by $\theta = 0.03^{\circ}$. Finally, the rotated graphene is stacked beneath the graphene on the top gate (Fig. 1e), which is then released onto the bottom gate on the prepatterned chip (Fig. 1f).

After stacking the double-gated TDBG structure, a Hall bar etching mask with 1D graphene contacts is designed on a clean region of the device. The device is coated with PMMA 950K

A4 resist, and the etching mask is written using e-beam

lithography. Exposed graphite and hBN regions are etched completely using low-power $\rm O_2$ and $\rm CHF_3/O_2$ plasma, respectively. After the Hall bar geometry has been defined (Fig. 2a), the device is coated with PMMA 495K A4 and PMMA 950K A2 to write the electrode pattern connecting to the TDBG contacts. After writing the pattern using electron beam lithography, the exposed contact regions of the Hall bar are then etched completely to expose a 1D TDBG contact region.

Finally, chromium, palladium, and gold contacts are deposited onto the chip, and the remaining resist is removed in an acetone bath (Fig. 2b).

Results:

Sweeping the top and bottom gate voltages of the device at T = 1.5K gave rise to gate-dependent signatures in the hole-doped region (Fig. 3a). This implies a gateinduced change in the structure being measured, in which graphene layers slide between a Bernal and rhombohedral stack ordering. By applying an external magnetic field, the magnitude of the switching response varies dramatically from the B = 0T case. After applying an external field B = 2T, the switching response in the higher hole density region is emphasized, whereas the switching response closer to charge neutrality is emphasized in the zero-field case (Fig. 3a,c). Having defined part of the switching region, the measurement scheme demonstrated in Fig. 3b is conducted, in which the device switches deep into the rhombohedral phase. From the rhombohedral-dominated phase, two measurements of the switching response Rxx(n, D) are made by ramping Vtg (Vbg) and then sweeping Vbg (Vtg) to map out the entire switching region. The sum of these plots highlights multiple boundaries in the holedoped region (Fig. 3d). These distinct equipotential lines correspond to the free energy required to overcome the domain wall pinning energy to switch from one order to another.

Conclusions and Future Steps:

These results demonstrate the transport behaviors of domain switching in multi-layer 2D materials. Domain switching can be used to gain new insights into exotic transport phenomena. Future experiments may involve domain switching in platforms with different stacking configurations, twist angles, and crystals. It would also be of great interest to explore emergent transport properties unique to these different stacking orders and their interactions in a domain switching platform.

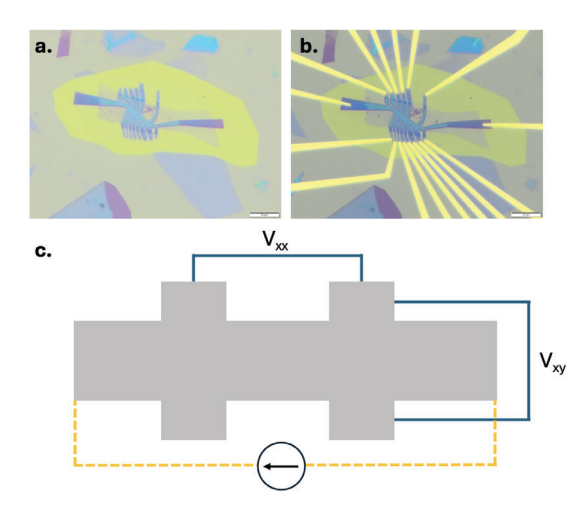


Figure 2: a, Complete stack (Fig. 1f) etched into a Hall bar geometry. b, Cr/Pd/Au contacts deposited on 1D TDBG contacts. c, Hall bar measurement configuration.

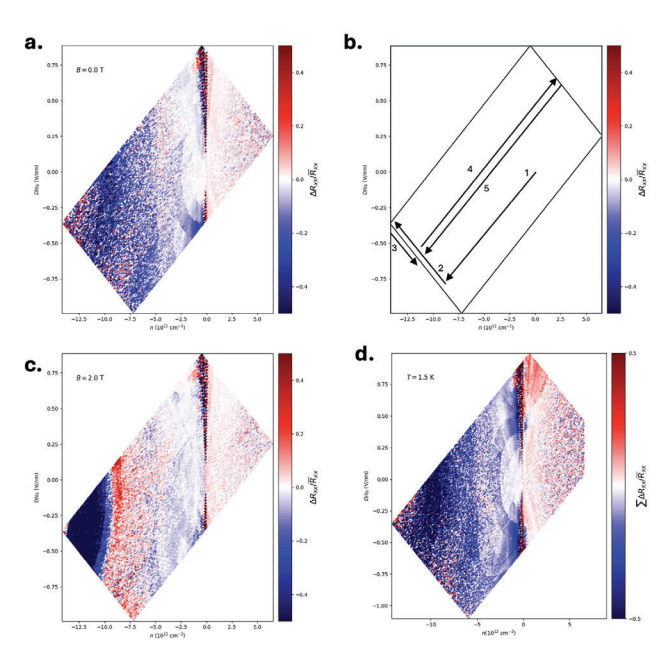


Figure 3: a, Switching boundary between Bernal and rhombohedral phases. This is defined by the mean normalized difference between the forward and backward bottom gate sweeps. b, Measurement scheme to define switching boundary in Fig. 3a. c, Same measurement as Fig. 3a under B=2T. d, Sum of the mean normalized differences from the bottom and top gate sweeps. This plot maps the entire rhombohedral-Bernal switching region.

- [1] K. S. Novoselov et al., Electric Field Effect in Atomically Thin Carbon Films.Science306,666-669(2004). https://doi. org/10.1126/science.1102896
- [2] Lui, C., Li, Z., Mak, K. et al. Observation of an electrically tunable band gap in trilayer graphene. Nature Phys 7, 944–947 (2011). https://doi.org/10.1038/nphys2102
- [3] Electrode-Free Anodic Oxidation Nanolithography of Low-Dimensional Materials Li, H. et al. Nano Letters 2018 18 (12), 8011-8015 DOI: 10.1021/acs.nanolett.8b04166

Structure and Dynamics of the Compression Induced Polycrystalline-Glass Transition

CNF Summer Student: Sylvie Shaya Student Affiliation: Wellesley College Department of Physics

Summer Program(s): 2025 Cornell NanoScale Facility Research Experience for Undergraduates (CNF REU) Program, SUPREME REU

Principal Investigator(s): Julia Dshemuchadse, Erin Teich

Mentor(s): Katherine Wang

Primary Source(s) of Research Funding: National Science Foundation award NNCI- 2025233 Contact: jd732@cornell.edu, et106@wellesley.edu, xw682@cornell.edu, ss131@wellesley.edu

Summer Program Website(s): https://cnf.cornell.edu/education/reu Research Group Website: https://capecrystal.mse.cornell.edu/

Abstract:

When polycrystal grain size is sufficiently reduced, materials undergo a solid-to-glass transition that is distinct from the more commonly studied liquid-to-glass transition and is critical to understanding the behavior of ultrafine-grained polycrystals. These materials hold promise in microelectronics and thermoelectrics, yet their behavior at and beyond the glass transition is not well understood. We simulate a binary system of hard and soft particles under compression to investigate the structure and dynamics of the polycrystalline-to-glass transition. Our results reveal a strong relationship between local structural features and dynamical behavior and indicate that soft particles play an outsized role in the glass transition, as they are associated with areas of strong dynamics and disorder.

Summary of Research:

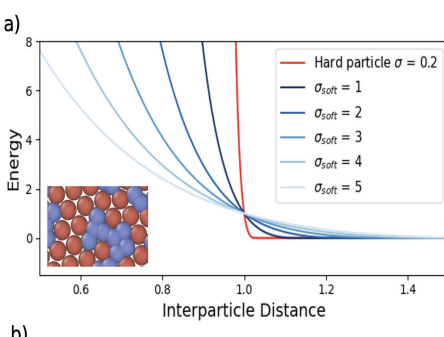
Background:

Polycrystals are known to exhibit Hall–Petch behavior, which describes how materials strengthen as grain size is reduced. As grain size is further decreased and grain boundary behavior dominates, polycrystals soften and become glassy [1]. Ultrafine-grained polycrystals display properties of interest for materials applications, including high electrical conductivity and reduced thermal conductivity, and understanding the polycrystalline-to-glass transition is critical for further development of these materials [2].

Simulation Methods:

We perform molecular dynamics simulations on a binary system of 6400 hard and 6400 soft discs using the simulation toolkit HOOMD-blue [3]. Particle interactions were defined by Weeks—Chandler—Andersen potentials shifted radially to ensure all particles have the same effective diameter of d=1, with Lorentz—Berthelot mixing rules applied to cross-interactions, described in Fig. 1(b). Particle softness was denied via σ , which varies the shape of the potential well. Hard-particle softness was defined as $\sigma=0.2$ and held constant for all systems, and soft-particle softness was varied between

 $\sigma_{\text{soft}} = 1$ and 5, as shown in Fig. 1(a).



$$U(r) = \begin{cases} 4\epsilon ((\frac{\sigma}{r-\Delta})^{12} - (\frac{\sigma}{r-\Delta})^6) - \epsilon & r < 2^{1/6}\sigma + \Delta \\ 0 & r \ge 2^{1/6}\sigma + \Delta \end{cases}$$
 (1)

$$\Delta = \frac{(d_{hard} + d_{soft})}{2} - \sigma \tag{2}$$

$$\sigma_{ij} = \frac{\sigma_{ii} + \sigma_{jj}}{2} \qquad \epsilon_{ij} = (\epsilon_{ii}\epsilon_{jj})^{1/2}$$
 (3)

Figure 1: Model setup. (a) Particle interactions via Weeks—Chandler—Andersen potentials for various softnesses σ . (b) Equations describing particle interactions. 1.) Weeks—Chandler—Andersen potentials, shifted radially by a factor Δ , defined in equation 2.). 3.) Lorentz—Berthelot mixing rules.

The system was initialized at low density, then randomized and compressed to a density between $\phi = 0.8$ and $\phi = 1.1$. Following compression, the system was equilibrated to account for artifacts from the compression step, then run for 10^8 molecular dynamics timesteps to collect data. Simulation temperature was fixed at kT = 0.2.

Results:

To establish the system's glassiness, we investigate the mean squared displacement (MSD) and the non-Gaussian parameter $\alpha(t)$, an indicator of dynamical heterogeneity. Glassy systems feature a plateau in MSD and a peak in $\alpha(t)$ at intermediate time scales, due to particles being trapped in cages of their neighbors before moving collectively at long time scales [4]. At low σ_{soft} , the system is crystalline and shows neither of

these features. We chose to focus on σ soft = 4, where we observe these behaviors at ϕ -values above 0.9, indicating that the system is glassy.

The compression of the system can be seen in the radial distribution functions (RDFs), where hard–soft and soft–soft RDF peaks are broader and located at smaller distances r than hard–hard peaks, seen in Fig. 2(a), as soft particles overlap under compression. There are clear peaks in the RDF at low ϕ , which disappear under compression, as shown in Fig. 2(b), reflecting the existence and subsequent breakdown of long-range order as the system transitions into a glass.

Lattice structure was characterized through the hexatic order parameter ψ_6 . Global ψ_6 is maximal (at 1) when the system is crystalline, and decreases at higher ϕ , shown in Fig. 2(c). At high densities, the distribution of soft particle ψ_6 is flatter than that of hard particles, seen in Fig. 2(d), indicating that soft particles tend to be more disordered than hard particles.

To characterize the dynamics of the system, we calculate the Lindemann parameter L, a measure of the strength of particle dynamics, and D^2 min, an indicator of irreversible rearrangements [1, 5]. At low densities, particles with large L and D^2 min exist primarily along grain boundaries. As density increases, high L and D^2 min particles form clusters throughout the system, as seen in Figs. 3(a)-(b). The distribution of soft-particle Ls and D^2 min is higher than those of hard particles, seen in Figs. 3(d)-(e), indicating that soft particles display stronger dynamics than hard particles.

To understand the relationship between dynamical parameters and structure, we calculated the covariances of D2min with the number of soft neighbor particles and L with ψ_6 , shown in Fig. 4(a)-(b). For $\sigma_{soft} = 4$, there is a peak at $\phi = 0.9$ for both covariances. The peak of the covariance of L and ψ^6 has been shown to correlate to the polycrystalline-to-glass transition [1]. We observe a peak in the same location in the covariance of D²min and number of soft neighbors, in Fig. 4(b), demonstrating a clear relationship between structure and dynamics at the glass transition.

As σ_{spft} increases, the peak of the covariance, and in turn the glass transition, shifts lower in density, seen in Fig 4(b). The global average ψ_6 shifts similarly, as seen in Fig. 2(c), as the breakdown in structure associated with the glass transition shifts.

Conclusion and Future Steps:

Under compression, binary systems of hard and soft particles display interesting behavior as they undergo a polycrystalline-to-glass transition. There is a strong relationship between the structure and dynamics of the system, seen in the covariances of dynamical and structural properties. Soft- particle softness impacts the location of the glass transition in density space, and soft particles appear to play an outsized role in this transition, as they tend to have stronger dynamics and disorder than hard particles.

Future steps include improved characterization of the

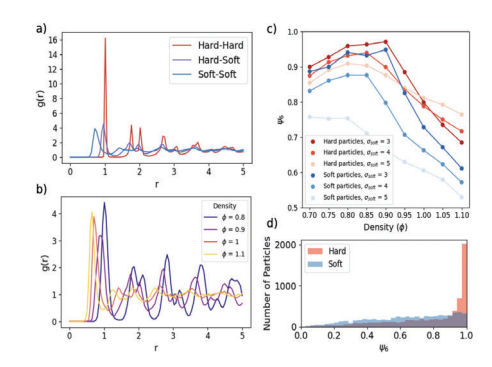


Figure 2: Structural parameters. (a) Type-wise RDFs for the 100th frame of simulations with $\sigma_{soft} = 4$ and $\phi = 1$. (b) Soft-soft RDFs for $\sigma_{soft} = 4$ over various ϕ values. (c) Global average ψ_6 for hard and soft particles. (d) Distributions of $\psi 6$ by particle type at the 100th frame of simulations with σ soft = 4 and $\phi = 1$.

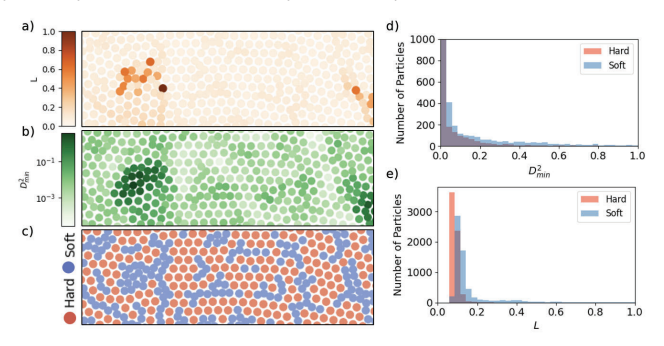


Figure 3: Dynamical characterizations, calculated over the first 100 frames of simulations with $\sigma_{soft} = 4$ and $\phi = 1$. (a) Heatmap of L. (b) Heatmap of D^2_{min} with a logarithmic colormap. (c) Particle identities at the 100th frame of simulation. (d) Histogram of L by particle type. (e) Histogram of D^2_{min} by particle type.

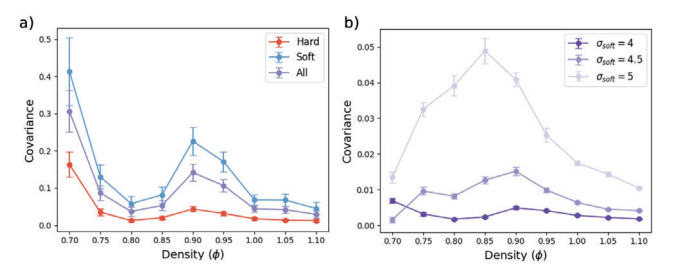


Figure 4: Covariances of dynamics and structure. (a) Typewise covariances of D^2_{min} and number of soft particle neighbors for $\sigma_{soft} = 4$. (b) All particle covariances of disorder, defined as $1 - \psi_{\theta}$ and L over various σ soft values.

relationship between structure and dynamics through statistical analysis, and descriptions of the collective motion of particles. Qualitative observation of the system indicates the existence of string- and loop-like cooperative motion, which in future work could be related to the structure of the system.

- [1] Zhang, H. & Han, Y. Physical Review X 8, 041023 (2018).
- [2] Lu, L. et al. Science 304, 422–426 (2004).
- [3] Anderson, J.A. et al. Computational Materials Science 173, 109363 (2020).
- [4] Teich, E.G. et al. Nature Communications 10, 64 (2019).
- [5] Falk, M.L. & Langer, J.S. Physical Review E 57, 7192 (1998).

Probing Spin Dynamics in Exfoliated van der Waals Ferromagnet Fe₅GeTe₇ Using Superconducting Resonators

CNF Summer Student: Matthew Willard Student Affiliation: Physics, SUNY Geneseo

Summer Program(s): 2025 Cornell NanoScale Facility Research Experience for Undergraduates (CNF REU) Program,

SUPREME REU

Principal Investigator(s): Gregory D. Fuchs

Mentor(s): Julie Soho Shim

Primary Source(s) of Research Funding: National Science Foundation award NNCI- 2025233, Center for Energy Efficient Magnonics (DE-AC02- 76SF00515), Department of Energy Office of Science, Basic Energy Sciences (DE-SC0019997)

Contact: gdf9@cornell.edu, jss545@cornell.edu, mtw14@geneseo.edu

Summer Program Website(s): https://cnf.cornell.edu/education/reu

Primary CNF Tools Used: AJA Orion Sputtering Systems, Heidelberg MLA 150 Maskless Aligner, Oxford 81/82, PT770 Etcher, DISCO Dicing Saw, Westbond 7400A Ultrasonic Wire Bonder

Abstract:

Two-dimensional (2D) magnetic materials offer a rich landscape for exploring spin dynamics and topological textures, with tunable properties and compatibility with heterostructure engineering. Among these, a 2D ferromagnet Fe₅GeTe₂ (F5GT) has emerged as a promising candidate due to its high Curie temperature and low Gilbert damping. However, bulk measurements are often limited by structural inhomogeneities. Here, we present a single-flake ferromagnetic resonance (FMR) study of exfoliated F5GT nanoflakes using high-Q superconducting resonators ($Q > 10^4$) to probe intrinsic damping properties with enhanced sensitivity. We observed ferromagnetic resonance in an F5GT flake transferred onto a 4 GHz superconducting resonator, demonstrating magnetic coupling between the flake and the resonator. The extracted upper bound for the Gilbert damping parameter is slightly lower than bulk values, indicating reduced damping in exfoliated samples. To further resolve damping contributions, we have also fabricated quarter-wavelength resonators with overtone modes and Q-factors exceeding 106, enabling frequencyresolved separation of viscous and inhomogeneous linewidth broadening. This work can offer new insights into the dynamical properties of van der Waals magnets.

Experimental Procedure:

Two-dimensional (2D) magnets have garnered significant attention for hosting exotic magnetic phenomena and topological spin textures, arising from strongly enhanced intrinsic spin fluctuations [1]. Their magnetic properties are readily tunable through external fields, strain, or chemical modifications, and their cleavable

nature enables seamless integration into engineered heterostructures [1]. These features position 2D magnets as versatile platforms for probing fundamental spin interactions and developing multifunctional devices that integrate electronic, optical, and magnetic properties. Despite their intriguing properties, many two-dimensional ferromagnetic materials exhibit Curie temperatures significantly below room temperature, restricting their practical use. Recently, a promising candidate—Fe_sGeTe₂ (F5GT)—has been identified [2], demonstrating a Curie temperature of up to 332 K in bulk [3] and 280 K in exfoliated thin flakes (~10 nm) [2]. A recent ferromagnetic resonance (FMR) study reported that bulk F5GT crystals exhibit effective Gilbert damping coefficient of $\alpha \approx 0.01$ —comparable to permalloy (NiFe)—although the measurements revealed substantial inhomogeneous linewidth broadening beyond viscous (Gilbert) damping contributions [3].

To better assess the intrinsic damping properties, we perform FMR measurements at the single- flake level using exfoliated F5GT, which are expected to be more structurally pristine. For this purpose, we design and fabricate high-Q superconducting resonators ($Q > 10^4$) and transfer exfoliated F5GT flakes onto them, enabling sensitive detection of their dynamic magnetic response (Fig. 1).

Fabrication:

Niobium (Nb) films were sputtered onto highresistivity Si (100) wafers using AJA Orion Sputtering Systems. Superconducting resonators were fabricated by patterning the Nb layer with the Heidelberg MLA 150 Maskless Aligner, followed by cleaning with Oxford 81/82 and dry etching using a PT770 Etcher. The patterned wafers were subsequently diced using a

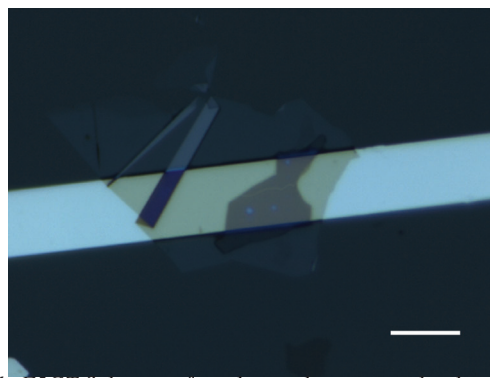


Figure 1: F5GT flake transferred onto the patterned inductor line of the 4 GHz superconducting resonator. A larger, close-to-transparent flake is the hBN flake capping the F5GT flake. The scale bar represents 10 µm.

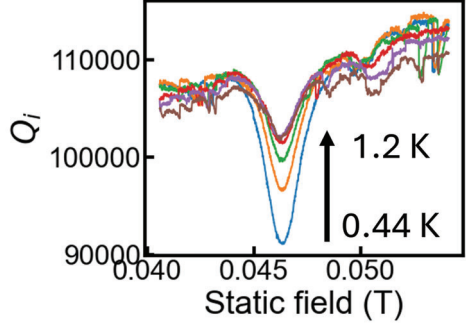


Figure 2: Ferromagnetic resonance (FMR) line at various temperatures.

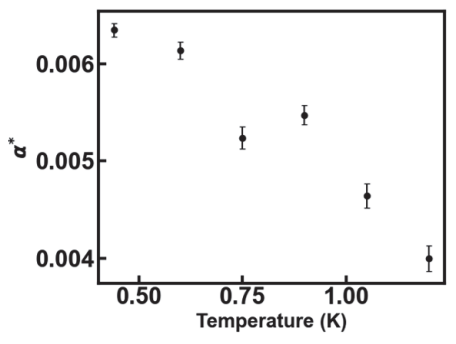


Figure 3: Estimated upper limit in Gilbert damping α^* at various temperatures..

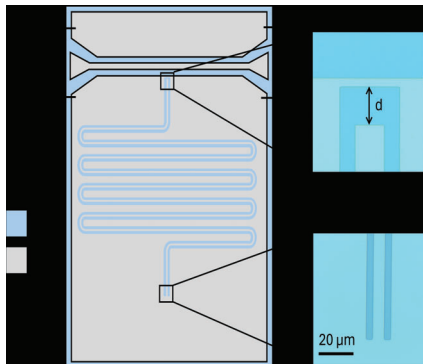


Figure 4: Schematic of the quarter-wavelength superconducting resonator. The zoomed-in optical images show the capacitive end and the inductive end of the resonator. The gap distance d in the capacitive end is 20 µm.

DISCO Dicing Saw. A nanoflake of Fe₅GeTe₂ (F5GT), capped with hexagonal boron nitride (hBN), was transferred onto the inductor line of the superconducting

resonator (Fig. 1). For ferromagnetic resonance (FMR) measurements, the Westbond 7400A Ultrasonic Wire Bonder was used to wirebond the resonator to an electrical circuit component.

Conclusions and Future Steps:

We performed ferromagnetic resonance (FMR) measurements on a 25 nm F5GT flake capped with a 10 nm hBN flake that is transferred onto a 4 GHz lumped-element superconducting resonator. As shown in Fig. 2, we observe a decrease in the intrinsic Q-factor (Qi) at a static magnetic field of 0.046 T. This reflects that as the F5GT flake comes into resonance, it is drawing energy out of the superconducting resonator, which results in an apparent decrease in Qi. This measurement confirms the coupling between the flake and the resonator and demonstrates successful single-flake FMR detection.

To estimate an upper bound for the Gilbert damping parameter (α^*) , we analyze the FMR linewidth under the assumption of negligible inhomogeneous broadening. The extracted α^* values are slightly lower but comparable to bulk values reported at 10 K ($\alpha \approx$ 0.007), suggesting reduced damping in the exfoliated sample (Fig. 3). Interestingly, we observe that α decreases with temperature in the range of 0.4 - 1.2 K. To further investigate damping properties at the singleflake level, we have designed and fabricated quarterwavelength superconducting resonators with optimized Q-factors, targeting values exceeding 106 (Fig. 4). A key advantage of this approach is that we will use the many overtone resonances, each as a separate frequency probe, which will allow us to distinguish viscous Gilbert damping from inhomogeneous linewidth broadening. The zoomed-in optical images show one representative device from a set of resonators we fabricated with varied gap distances, all of which are ready for FMR characterization. We plan to measure each resonator's Q-factor, transfer F5GT nanoflakes, and utilize overtone modes to extract the intrinsic damping parameters of F5GT with enhanced spectral resolution.

- K. S. Burch, D. Mandrus, and J.-G. Park, Nature, 563, 47-52 (2018). J. M. Bartell, D. H. Ngai, Z. Leng, G. D. Fuchs, Nat. Commun., 6, 8460 (2015).
- [2] A. F. May et al, ACS nano, 13, 4436-4442 (2019). C. Zhang,
 J. M. Bartell, J. C. Karsch, I. Gray, and G. D. Fuchs, Nano
 Lett., 21, 4966-4972 (2021).
- [3] L. Alahmed et al, 2D Mater. 8, 045030 (2021).Mater. Quantum. Technol. 4(2), 025801 (2024).https://doi.org/10.1088/2633-4356/ad4b8c
- [4] 1 M.P. Bland, F. Bahrami, J.G.C. Martinez, et al. "2D transmons with lifetimes and coherence times exceeding 1 millisecond," (2025).

Out-of-plane spin component produced by magnetic ordering

CNF Project Number: 598-96

Principal Investigator(s): Daniel C. Ralph

User(s): Xiaoxi Huang

Affiliation(s): Department of Physics, Cornell University
Primary Source(s) of Research Funding: Department of Energy

Contact: dcr14@cornell.edu, xh384@cornell.edu

Primary CNF Tools Used: Heidelberg MLA 150 Maskless Aligner, AJA Sputter Deposition

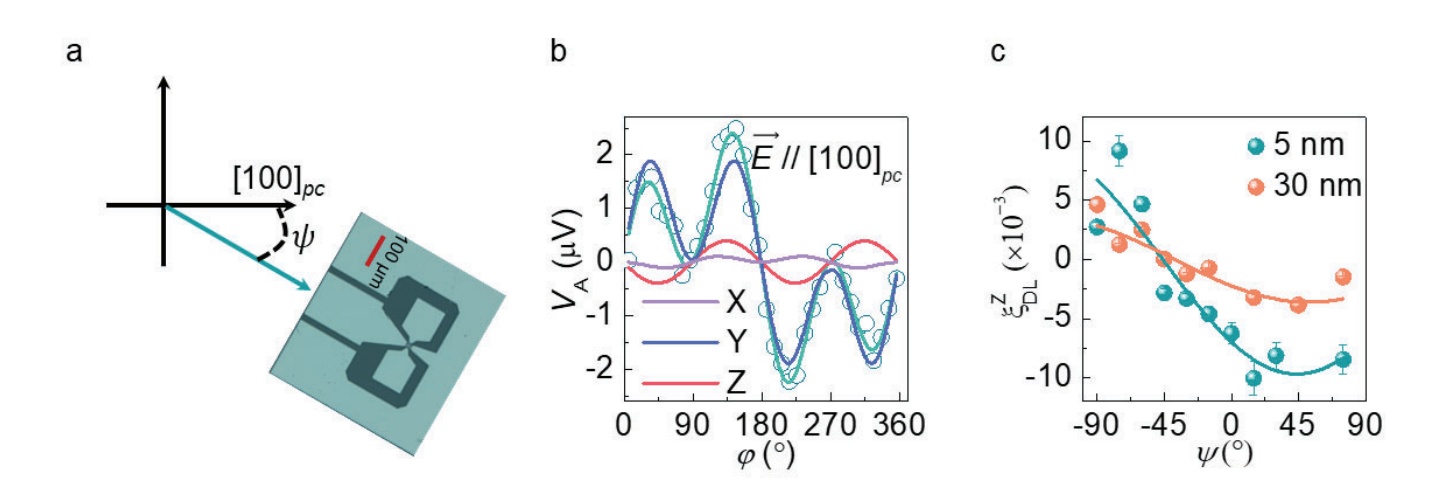


Figure 1:Out-of-plane anti-damping torque generation. a) A schematic demonstration of the in-plane crystallographic study. b) A signature of the out-of-plane anti-damping torque, $\sin 2 \Psi$ component. c) $\xi z/DL$ as a function of in-plane electric field angle. Figure 2 | Non-local excitation and detection of coherent magnons.

Abstract:

Micron-sized devices made with the Heidelberg MLA maskless laser direct writer and AJA sputter system were used to study spin currents and magnon currents generated as a consequence of magnetic ordering. We experimentally observed that a canted magnetic moment produces an out-of-plane damping-like torque from SrRuO3 thin films.

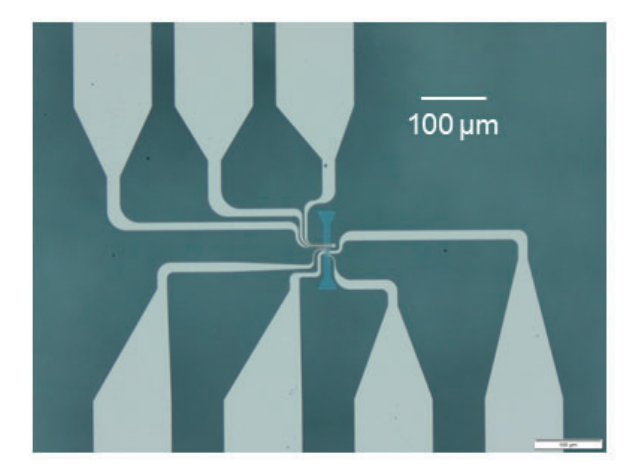
Summary of Research:

Magnetic materials with perpendicular magnetic anisotropy (PMA) are the most promising materials for high-density magnetic memory; and the efficient magnetization switching of PMA-magnets is enthusiastically pursued by Spintronics researchers because it has the potential to realize energy-efficient high-density information storage. Fortunately, an out-of-plane spin component borne by a spin current is theoretically predicted and experimentally demonstrated to be able to drive efficient anti-damping switching of the magnetization of a PMA magnet [1]. Our primary

research goal is to find materials that efficiently produce spin currents or magnon currents with an out-of-plane spin component and ultimately to demonstrate the efficient switching of magnetization of PMA-magnet pillars with diameters as small as 100 nm. Our search for such materials has been centered around materials that have magnetic order, including both ferromagnetic and anti-ferromagnetic order. To detect spin current generation and the specific spin orientations that are allowed for these materials, micron-sized devices such as spin-torque ferromagnetic resonance (ST-FMR) devices and non-local magnon excitation and detection devices are patterned using these materials.

The ST-FMR device is shown in Fig. 1a. Bar structures with dimension of 20 μ m \times 70 μ m are patterned with the Heidelberg MLA maskless laser direct writer. Then contacts made of Ti/Pt are deposited on the patterns in an AJA sputtering system. An example of spin current generated because of magnetic order is the unconventional spin-orbit torque generation from SrRuO3. SrRuO3 thin films when grown on (001)-oriented SrTiO3 substrates

a



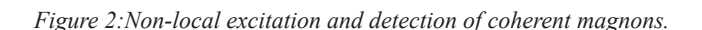
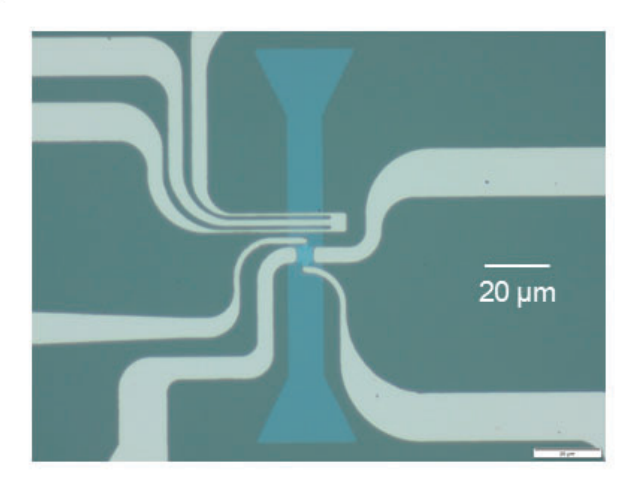


exhibit canted magnetization and ferromagnets with magnetic moment canted out of the plane are predicted to be able to produce tilted spin currents with tilted spin polarization [2]. We measured the spin-orbit torque generated by SrRuO3 is on ST-FMR devices (Fig. 1a). When the rf current and oscillating magnetoresistance are mixed together, a dc mixing voltage is produced. The anti-symmetric component of the mixing voltage is contributed by the out-of-plane torques. A signature of the out-of-plane anti-damping torque is observed for electric field applied along [100]pc (Fig. 1b). To investigate the origins of out-of-plane anti-damping torque, the ST-FMR measurements were repeated on devices with intermediate Ψ angles for the orientation of the applied electric field relative to the [100]pc crystal direction (Fig. 1a). The out-of-plane anti-damping torque efficiency ξz/DL has the angular dependence shown in Fig. 1c, which indicates that two different mechanisms contribute to the out-of-plane toque (the spin anomalous Hall effect and the planar Hall spin current) This is the most exciting and important finding of our work so far and this work is currently under review.

Another pathway to produce out-of-plane spin component is to utilize coherent magnons, as a circularly polarized magnon in a magnetic material will have a net spin angular momentum aligned with magnetization b



[3]. We study the excitation and detection of coherent magnons on devices shown in Fig. 2, where coherent magnons are excited by a microwave-current-induced Oersted field and detected by spin-torque-induced harmonic Hall voltages. The ground-signal-ground waveguide on the excitation side has a minimum dimension of 1 μ m and the Hall device on the detection side is of dimension 4 μ m ×1 μ m.

Conclusions and Future Steps:

Magnetic ordering plays a crucial role in producing out-of-plane damping-like torques. We plan to publish the work on SrRuO3 and to study the out-of-plane spin component produced by coherent magnons.

- [1] David MacNeill et al, Nat. Phys. 13, 300 (2017).
- [2] Tomohiro Taniguchi et al, Phys. Rev. Lett. 3, 044001 (2015).
- [3] Jiahao Han et al, Science 366, 1121 (2019).

Gate-tunable electroresistance in a sliding ferroelectric tunnel junction

CNF Project Number: 598-96

Principal Investigator(s): Daniel C. Ralph

User(s): Bozo Vareskic

Affiliation(s): Laboratory for Atomic and Solid State Physics, Cornell University

Primary Source(s) of Research Funding: National Science Foundation (NSF) grant DMR-2104268

Contact: dcr14@cornell.edu, bv227@cornell.edu

Primary CNF Tools Used: Zeiss Supra SEM, Nabity Nanometer Pattern Generator System, Angstrom E-Beam

Evaporator, Oxford 81 Etcher

Abstract:

Ferroelectric tunnel junctions are an attractive platform next-generation memory applications due to their capacity for non-volatile operation and non-destructive readout of the electrical polarization. Generating a tunneling current that is sensitive to the polarization state requires a tunneling potential profile that is mirror asymmetric. This asymmetry has been engineered in previous work by using electrode layers with mismatched densities of states [1] or dielectric spacer layers directly within the tunnel barrier [2]. Here, we show that by fabricating ferroelectric tunnel junctions with an electrostatic gate, the tunneling conductance can be sensitive to the polarization state even when the two electrode layers are both monolayer graphene and there is no dielectric spacer layer. The magnitude and sign of the resulting tunneling electroresistance can be controlled by the bias and gate voltage of the junction.

Summary of Research:

In a ferroelectric tunnel junction (FTJ), two conducting layers sandwich an insulating ferroelectric tunnel barrier. Achieving appreciable readout currents with conventional ferroelectrics is challenging since depolarization fields, which increase with decreasing film thickness, can destabilize ferroelectric order in ultra-thin layers. Van der Waals ferroelectric materials, however, can sustain ferroelectric polarizations with no critical thickness limit. Recently discovered van der Waals sliding ferroelectrics offer a novel mechanism for ferroelectric switching that also promises higher endurance compared to non-sliding ferroelectrics [3-5].

In our devices, we mechanically assemble parallel bilayer boron nitride (P-BBN) with graphene electrodes on either side. The heterostructure is encapsulated by hexagonal boron nitride dielectric layers with a bottom graphitic gate. Figure 1 shows a schematic of the device geometry. To make electrical contact to the graphene

electrode and graphite gate layers, we perform electron beam lithography (Zeiss Supra SEM and Nabity Nanometer Patter Generator System) and reactive ion etching (Oxford 81 Etcher) to first expose edges of the conducting layers. We then deposit Ti/Au contacts with electron beam deposition (Angstrom Evaporator). Figure 2 shows a micrograph of a completed device.

Transport measurements are performed at T=4.2K. We measure the differential conductance dI/dV of the junction by applying a small AC bias (1 mV) as we sweep the DC bias, V, and read out the resulting AC current. The gate voltage, V_G , is fixed during each bias sweep. The left panel of Figure 3 shows the tunneling conductance on a forward and backward sweep of the DC bias. The tunneling conductance is nonlinear and increases with bias voltage, indicating that the P-BBN acts as a good insulating barrier. Step-like features in the conductance are likely due to inelastic electron tunneling assisted by phonons in the barrier or electrode layers. The tunneling conductance is hysteretic with the bias and can be quantified by the tunneling electroresistance

TER =100
$$\times \frac{G_f - G_b}{G_f + G_b}$$
 where $G_{f(b)}$ is the conductance of

the forward (backward) bias sweep.

Notably, the magnitude and sign of the TER vary strongly with DC bias. At $V_G = -1.0$ V, Figure 3 right panel, a positive peak appears at negative bias while a negative peak is present at positive bias. By varying the gate, the bias dependence of the TER can be controlled. Figure 4 shows the same data as Figure 3 but now taken at $V_G = 5.4$ V. Now, a negative (positive) peak is present at negative (positive) bias, which is opposite the signal at $V_G = -1$ V (Figure 3 right panel).

In summary, we have shown that the conductance graphene/P-BBN/graphene tunnel junction is sensitive

to the polarization state of ferroelectric P-BBN. The magnitude and sign of the resulting TER can be tuned by the bias and gate voltage.

- [1] M. Y. Zhuravlev, R. F. Sabirianov, S. S. Jaswal, and E. Y. Tsymbal, Physical Review Letters 94, 246802 (2005).
- [2] M. Y. Zhuravlev, Y. Wang, S. Maekawa, and E. Y. Tsymbal, Applied Physics Letters 95, 052902 (2009).
- [3] K. Yasuda, X. Wang, K. Watanabe, T. Taniguchi, and P. Jarillo-Herrero, Science 372, 1458 (2021).
- [4] C. R. Woods, P. Ares, H. Nevison-Andrews, M. J. Holwill, R. Fabregas, F. Guinea, A. K. Geim, K. S. Novoselov, N. R. Walet, and L. Fumagalli, Nature Communications 12, 347 (2021).
- [5] M. Vizner Stern, Y. Waschitz, W. Cao, I. Nevo, K. Watanabe, T. Taniguchi, E. Sela, M. Urbakh, O. Hod, and M. Ben Shalom, Science 372, 1462 (2021).

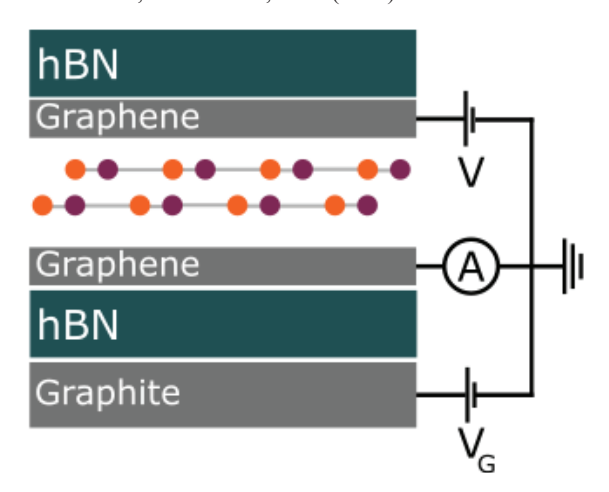
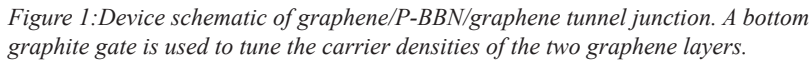


Figure 4:Same as Figure 3 but at $V_G = -5.4 \text{ V}$.



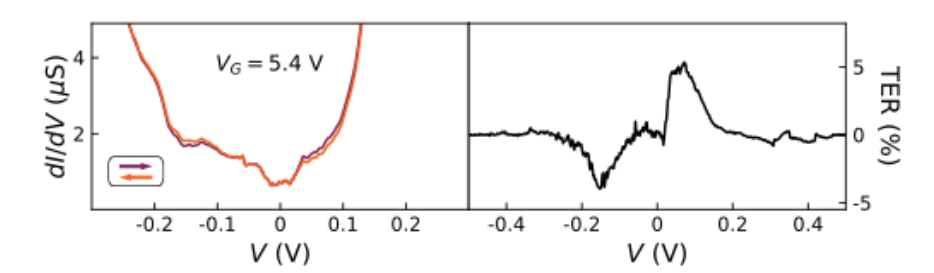


Figure 2:Micrograph of device. The graphene electrodes, P-BBN, and graphite gate electrode are outlined in dashed white, black, and orange lines, respectively. The scale bar is $10 \, \mu m$

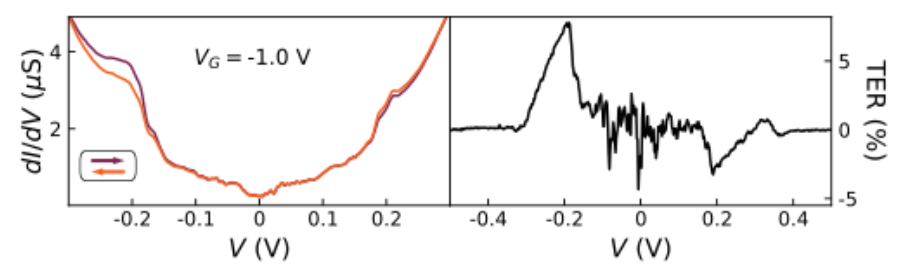


Figure 3: Left: Tunneling conductance as a function of bias voltage at constant gate voltage $V_G = -1.0 V$ The forward (backward) sweep is shown in purple (orange). Right: TER calculated from the data on the left panel.

Quantum-Limited Measurement as a Tool for Entanglement in Superconducting Circuits

CNF Project Number: 173508

Principal Investigator(s): Ivan Pechenezhskiy, Britton Plourde

User(s): Jadrien Paustian

Affiliation(s): Syracuse University

Primary Source(s) of Research Funding: Syracuse University

Contact: ivpechen@syr.edu, jtpausti@syr.edu

Primary CNF Tools Used: Anatech Oxygen Descum, PlasmaTherm 770 Reactive Ion Etch, Photoresist Processing,

DISCO Dicing Saw

Abstract:

As part of the Materials Characterization and Quantum Performance: Correlation and Causation project, we tuned up the niobium base layer recipes for fabrication of quantum superconducting devices while carefully documenting correlations between process changes and resonator internal quality factors. We find significant correlations between internal quality factors and the deposition conditions, the photoresist stripping chemistry, and the dose of post-fabrication hydrofluoric acid treatment.

Summary of Research:

We performed in-house photolithography before moving on to fabrication at the CNF, where we make use of the Anatech as an oxygen descum prior to a reactive ion etching with the PlasmaTherm 770 using a chlorine-based reactive ion etch. We then stripped off the photoresist in the hot strip baths in the photoresist section, before an additional descum with the Anatech tool and spinning protective resist on the sample for dicing. Dicing was performed using the DISCO dicing saw. Then, at Syracuse University, we performed additional HF treatments afterwards. The resonator devices are measured in an adiabatic demagnetization refrigerator. A packaged sample is shown in Figure 1. 20 minutes of buffered oxide etch provides the best quality factors for our samples, as shown in Figure 2. We solved significant issues created by the resist stripping process, demonstrating an optimal resist strip using AZ300T, shown in Figure 3. Additionally, after noticing anomalies in our temperature-dependent measurements, we began varying our sputter parameters. This altered our film stress by changing the deposition environment, and we found that film stress creates an anomalous increase in thermal losses, as shown in Figure 4.

Conclusions and Future Steps:

We observe that the interplay between treatments at different fabrication steps can have unintuitive effects on sample quality. We find distinct correlations between hydrofluoric acid treatment, resist stripping, and internal quality factors of superconducting resonators. We additionally find that sputter deposition parameters can alter the film stress, which can produce anomalous temperature dependence in loss.

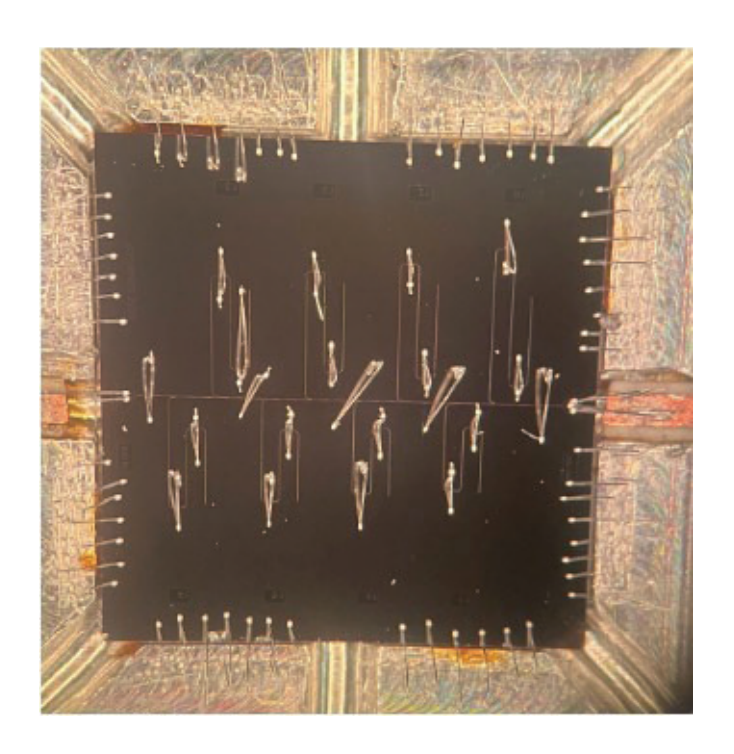


Figure 1: Fully packaged sample

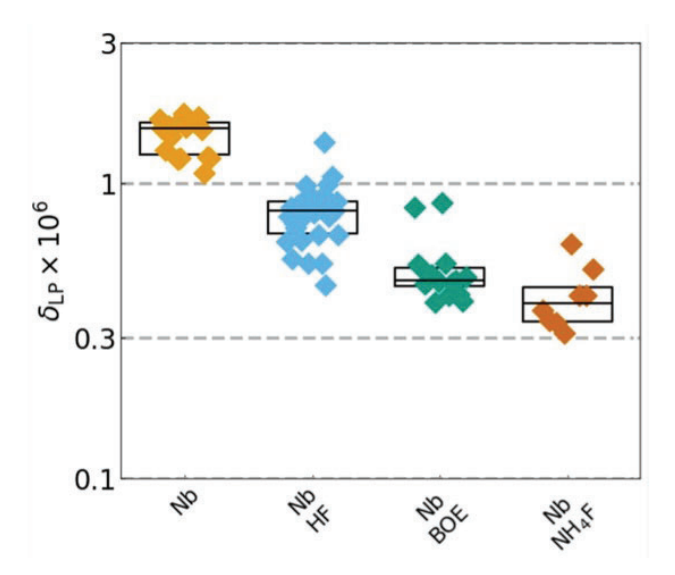


Figure 2: Loss tangents achieved with optimal HF treatment using buffered oxide etch, and a further improvement with ammonium fluoride.

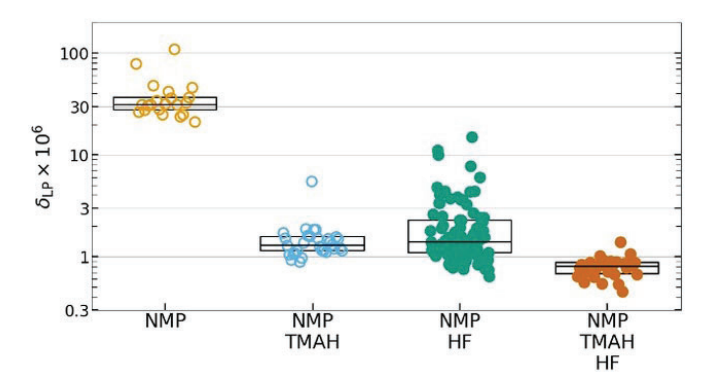


Figure 3: Loss tangents achieved with AZ300T resist stripping, a solution of n-methyl-2-pyrrolidone and tetramethyl-ammonium-hydroxide.

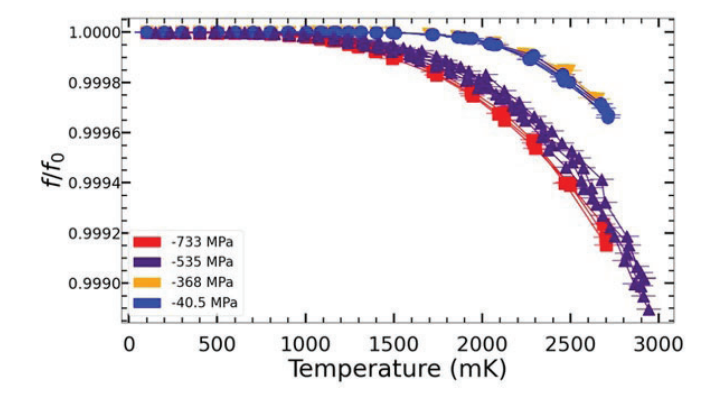


Figure 4: Relative resonator frequency shifts with anomalous temperature dependent frequency shifts for samples with average room temperature film stress beyond -500 MPa.

References:

[1] Maciej W. Olszewski et al. Low-loss Nb on Si superconducting resonators from a dual-use spin-tronics deposition chamber and with acid-free post-processing. 2025. arXiv: 2503.13285 [quant-ph]. url: https://arxiv.org/abs/2503.13285.

Deposition of Gold Films as a Sample Surface Coating for Magnetic Resonance Force Microscopy

CNF Project Number: 212512

Principal Investigator(s): John Marohn

User(s): George Du Laney

Affiliation(s): Chemistry & Chemical Biology, Cornell University

Primary Source(s) of Research Funding: National Institutes of Health, Cornell University

Contact: gdf9@cornell.edu, jam99@cornell.edu, grd44@cornell.edu

Website: https://marohn.chem.cornell.edu/

Primary CNF Tools Used: CVC SC4500 Odd-Hour E-beam evaporator

Abstract:

We employ e-beam evaporation of gold to prepare a surface noise-reducing coating for applications in magnetic resonance force microscopy. By transferring the deposited gold film from a sacrificial polymer to our samples of interest, we ensure we have a sample with the benefits of a gold coating while avoiding sample damage from direct exposure to e-beam evaporation.

Summary of Research:

Magnetic resonance force microscopy (MRFM) is a scanning-probe technique used to resolve the locations of nuclear and electronic spins using principles of magnetic resonance. To accomplish this, we bring an attonewton-sensitive magnet-tipped microcantilever in proximity to a spin-polarized sample. The sample's polarization is modulated and the resulting changes to the cantilever's vibrational amplitude and frequency are recorded as the signal. A challenge in MRFM is achieving an optimal cantilever-sample separation while avoiding surface noise-induced frequency fluctuations. It has been shown that applying a conductive layer over a polymer sample can reduce this surface noise. [1] Previous work has employed e-beam evaporated gold films to reduce surface noise in MRFM measurements. [2-4] Radical-doped polymer films which had gold directly e-beam evaporated onto them had a reduced electron spin resonance (ESR) signal due to a suspected "dead layer" within the sample from excess heating. [5] A novel film transfer approach was developed whereby the gold was e-beam evaporated onto a sacrificial layer and then transferred onto the sample obviated this issue, recovering a factor of 20 in enhancement was achieved. [6]

Despite this 20-fold enhancement, there is still a factor of 17 difference between experimental ESR-MRFM signal and predicted signal. As we adjust our experimental parameters to recover this remaining factor of 17, we

continue to use this gold laminate coating to reduce sample surface noise.

Figure 1 shows a representative gold-laminate sample prepared for MRFM. The vertical column in the center is 20 nm of e-beam-evaporated gold sitting atop a ~520 nm film of tempamine-doped polystyrene. The ensemble of films sits atop the centerline of a custommade waveguide for delivering radiofrequency and microwave radiation to the polystyrene film. A strip of gold was achieved by masking the sacrificial substrate with Kapton tape during e-beam evaporation. Masking allows the preparation of gold films that are small enough to stay over the centerline without covering the tapered regions of the waveguide, which would make the waveguide very lossy. To transfer the gold to the polymer-coated waveguide, the strip is aligned to the centerline, pressed together, and then the sacrificial substrate is allowed to dissolve, leaving the gold laminated to the polymer-coated waveguide.

This procedure of predefining the shape of the gold and aligning to the waveguide before dissolving the sacrificial polymer marks an improvement over a previously used version of this procedure, whereby strips were cut with a razor from a gold film that spanned the substrate, the sacrificial polymer was dissolved in water. [6] The cut-out flecks of gold were left to float on the water's surface, and the waveguide was stamped onto the flecks, which had a tendency to laminate imperfectly or in an incorrect location on the waveguide. This new transfer procedure affords the user more control over gold positioning, and

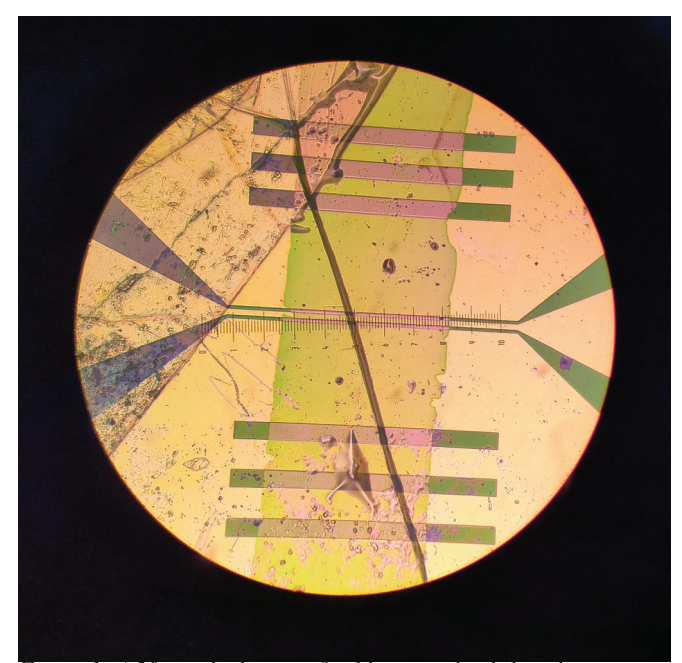


Figure 1: A 20 nm-thick strip of gold on a radical-doped polystyrene film, located over the centerline of a waveguide. Centerline dimensions are 10 µm by 500 µm. The roughness in the top left of the image is excess polystyrene film that did not laminate flatly during the transfer step. This image was taken using the Cornell Center for Materials Research's Olympus BH-2 optical microscope with IC20 objective. The graticule in the image is 500 µm across.

a single attempt is usually sufficient per waveguide.

Conclusions and Future Steps:

The implementation of e-beam evaporated gold films as a surface coating in our experiments continues to improve. Previous work developed a transfer procedure that avoided sample damage, and our latest procedure affords greater control over positioning the gold coating during the transfer. In the future, we may employ lithographically-defined masks to make precisely-defined regions of gold, but Kapton tape affords us the precision we need for the time being.

- [1] Kuehn, S.; Loring, R.F.; Marohn, J.A. Phys. Rev. Lett. 2006, 96 (15), 156103.
- [2] Garner, S.R.; Kuehn, S.; Dawlaty, J.M.; Jenkins, N.E.; Marohn, J.A. Appl. Phys. Lett. 2004, 84 (25), 5091–5093.
- [3] Moore, E.W.; Lee, S-G.; Hickman, S.A.; Wright, S.J.; Harrell, L.E.; Borbat, P.P.; Freed, J.H.; Marohn, J.A. Proc. Natl. Acad. Sci. U.S.A. 2009, 106 (52), 22251–22256.
- [4] Hickman, S.A.; Moore, E.W.; Lee, S-G. Longenecker, J.G.; Wright, S.J.; Harrell, L.E.; Marohn, J.A. ACS Nano 2010, 4 (12), 7141–7150.
- [5] Isaac, C.E. Ph.D. thesis, Cornell University/Cornell University, Ithaca, NY, 2018.
- [6] Boucher, M.C.; Isaac, C.E.; Sun, P.; Borbat, P.P.; Marohn, J.A. ACS Nano 2023, 17 (2), 1153–1165.

Perfect Coulomb Drag in a Dipolar Excitonic Insulator

CNF Project Number: 263318

Principal Investigator(s): Jie Shan, Kin Fai Mak

User(s): Raghav Chaturvedi, Phuong X. Nguyen, Jinwoo Yu

Affiliation(s): Laboratory of Atomic and Solid State Physics, School of Applied and Engineering Physics; Cornell University

Primary Source(s) of Research Funding: DOE, NSF, AFOSR, Moore Foundation

Contact: jie.shan@cornell.edu, kinfai.mak@cornell.edu, rc669@cornell.edu, pxn2@cornell.edu, jy968@cornell.edu

Website: https://sites.google.com/site/makshangroup/

Primary CNF Tools Used: Zeiss Supra SEM, Nabity Nanometer Pattern Generator System (NPGS), Angstrom E-Beam Evaporator, SC4500 Odd/Even- Hour Evaporator, Oxford 81/82 RIE, YES Asher, Autostep i-line Stepper, Hamatech Wafer Processor Develop, Heidelberg Mask Writer - DWL2000, Photolithography Spinners, Dicing Saw - DISCO

Abstract:

Exciton is a quasiparticle made of one electron and one hole bound by Coulomb attraction. In systems where the exciton binding energy exceeds the single particle band gap, excitons spontaneously form, and the new ground state is an excitonic insulator (EI): conducting for excitons but insulating for free electrons or holes. In this work, we realize a dipolar EI in MoSe2/WSe2 double layers. The formation of excitons results in perfect Coulomb drag, that is, driving a charge current in one layer induces an equal and opposite drag current in the other layer. Upon increasing exciton density beyond the critical Mott density, excitons dissociate into an electron-hole plasma and the drag current becomes negligible. Our work opens pathways to realize exciton superfluidity and other exotic phases of correlated excitons.

Summary of Research:

Excitonic insulators (EIs) [1] form when the binding energy of bound electron-hole pairs exceeds the single particle bandgap in a semiconductor. Unlike charge insulators, where the charges are immobile, excitons can flow. However, excitons are charge neutral which makes driving an exciton current impossible in bulk EIs. Using van der Waals (vdW) semiconductors it's possible to fabricate independent electron and hole contacts by separating the electrons and holes to dilerent layers of material. This approach has been used to flow an exciton current in coupled GaAs quantum wells [2] and graphene double layers [3], however, only in the quantum Hall regime. In our work, we use dipolar EIs observed in Coulomb-coupled double layers [4] to flow an excitonic current in the absence of magnetic field [5].

Figure 1A and 1B show a schematic cross-section and

an optical image of our device, respectively. The device consists of WSe2/MoSe2 double layers separated by a thin hexagonal boron nitride (hBN) barrier. WSe2 and MoSe2 form a type-II band alignment as shown in Figure 1C, that is, the lowest (highest) energy conduction (valence) band lies in the MoSe2 (WSe2) layer. The double layer is further encapsulated by two gates made of hBN and graphite. We use Pt and Bi electrodes that make Ohmic contacts to holes in the WSe2 layer and electrons in the MoSe2 layer, respectively. An interlayer bias, V_b , is applied between the layers to tune electronhole pair density, n_p , and the gate voltages allow to tune electronhole density imbalance. Our experiment is performed at equal electron and hole densities.

Figure 2A shows the configuration for the Coulomb drag measurement. An electron current is driven in the MoSe₂ layer while WSe2 layer is connected to an ammeter. In this configuration, when an exciton current flows in the system, it's expected that the drive current in the MoSe₂ layer will induce an equal and opposite drag current in the WSe₂ layer. This is because a flowing electron in the MoSe₂ layer will drag along a hole in the WSe2 layer.

The results for the Coulomb drag measurement are shown in Figure 2B. Drive current in the $MoSe_2$ layer (black line) is observed when V_b crosses a threshold value and injects electron-hole pairs into the double layer. At low n_p , the drag current (red line) in the WSe_2 layer exactly traces the drive current. The ratio of the drag and drive current (blue line) persists to 1 for exciton density up to $\sim 4 \times 10^{11}$ cm⁻². Upon further increasing N_p beyond this density, the drag current abruptly drops to zero. This corresponds to the Mott limit, beyond which excitons unbind into an electron-hole plasma due to larger screening of the electron-hole interaction at higher densities.

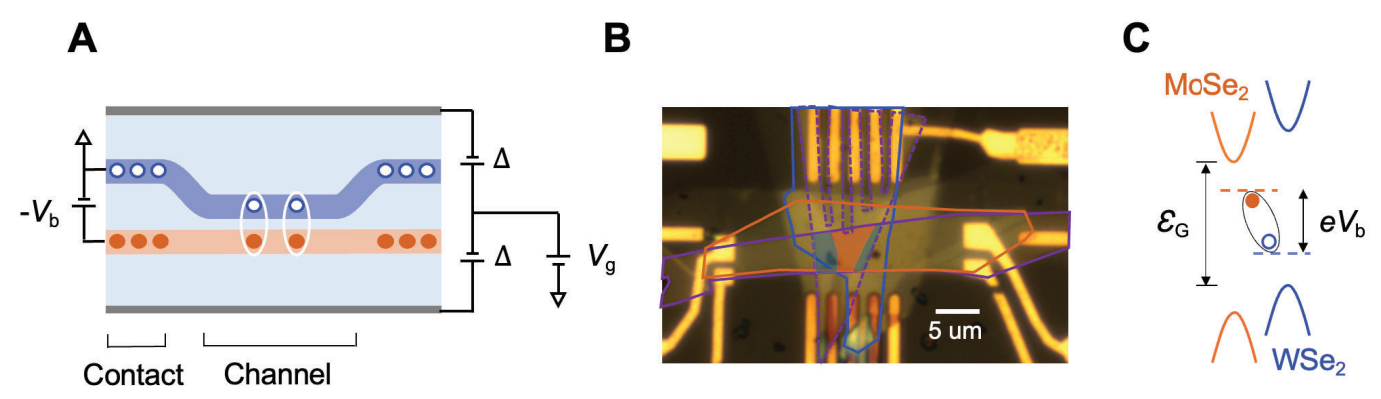


Figure 1: a, Schematic cross-section of the device. b, Optical microscope image of a double layer device. Scale bar is 5 μm. c, Type-II band alignment of MoSe, and WSe,.

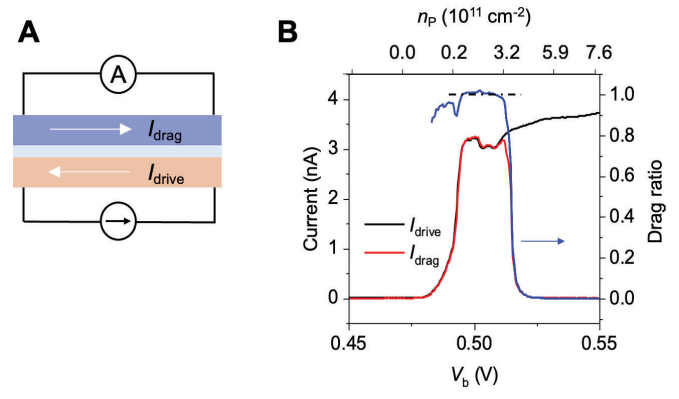


Figure 2: a, Circuit for Coulomb drag measurement. b, Drive (black line) and drag (red) currents in the MoSe2 and WSe2 layers respectively measured as a function of V_b . The ratio of the currents is plotted in blue. The black dashed line marks drag ratio = 1.

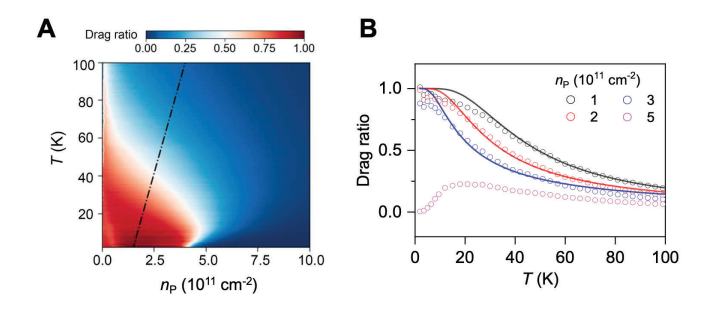


Figure 3: a, Drag ratio as a function of temperature and n_p . Black dashed line corresponds to the degeneracy temperature. b, Linecuts of drag ratio as a function of temperature for dilerent n_p . Solid lines are fit to the Saha equation.

We measure the temperature dependence of the drag ratio for varying n_p as shown in Figure 3. The drag ratio remains above 0.9up to 20 K at low n_p. When excitons are dissociated above the Mott limit, only frictional drag is observed with a characteristic quadratic temperature dependence as expected for two independent Fermi liquids. Furthermore, the temperature dependence of the drag ratio can be largely captured by a simple ionization model (solid lines in 3B) based on the Saha equation. We also plot the degeneracy temperature (black dashed line) obtained through compressibility measurements for each density in Fig 3A. Below the degeneracy temperature, the exciton fluid is expected to become a quantum fluid.

Our work successfully realizes exciton circuitry in the absence of a magnetic field and enables future studies of exciton transport, including a four-terminal measurement of the exciton chemical potential that can directly detect exciton superfluidity.

- 1] D. Jérome, T.M. Rice & W. Kohn, Excitonic Insulator, Physical Review 158, 462–475 (1967).
- [2] D. Nandi, A. D. K. Finck, J. P. Eisenstein, L. N. Pfeiler & K. W. West, Exciton condensation and perfect Coulomb drag. Nature 488, 481–484 (2012).
- [3] X. Liu, K. Watanabe, T. Taniguchi, B. I. Halperin & P. Kim, Quantum Hall drag of exciton condensate in graphene. Nat. Phys. 13, 746–750 (2017).
- [4] L. Ma, P. X. Nguyen, Z. Wang, Y. Zeng, K. Watanabe, T. Taniguchi, A. H. MacDonald, K. F. Mak & J. Shan, Strongly correlated excitonic insulator in atomic double layers. Nature 598, 585–589 (2021).
- [5] P. X. Nguyen, L. Ma, R. Chaturvedi, K. Watanabe, T. Taniguchi, J. Shan & K. F. Mak, Perfect Coulomb drag in a dipolar excitonic insulator. Science 388, 274–278 (2025).

Superconductivity in twisted bilayer WSe,

CNF Project Number: 263318

Principal Investigator(s): Jie Shan, Kin Fai Mak User(s): Zhongdong Han, Yiyu Xia, Yichi Zhang

Affiliation(s): Laboratory of Atomic and Solid State Physics, School of Applied and Engineering Physics; Cornell University

Primary Source(s) of Research Funding: DOE, NSF, AFOSR, Moore Foundation

Contact: jie.shan@cornell.edu, kinfai.mak@cornell.edu, zh352@cornell.edu, yx579@cornell.edu, yz2662@cornell.edu Website: https://sites.google.com/site/makshangroup/

Primary CNF Tools Used: Zeiss Supra SEM, Nabity Nanometer Pattern Generator System (NPGS), Angstrom E-Beam Evaporator, SC4500 Odd/Even-Hour Evaporator, Oxford 81/82 RIE, YES Asher, Autostep i-line Stepper, Hamatech Wafer Processor Develop, Heidelberg Mask Writer - DWL2000, Photolithography Spinners, Dicing Saw - DISCO

Abstract:

Semiconductor moiré materials have emerged as a highly tunable platform for simulating the Hubbard model [1,2], which is believed to capture the essential physics of high-temperature superconductors [3]. However, the experimental evidence for superconductivity in these systems remains elusive. Here, we report the observation of robust superconductivity in twisted bilayers WSe₂. Our results reveal its unconventional nature rooted in strong electron correlations.

Summary of Research:

The Hubbard model [4], a simplest model describing interacting electrons on a lattice, provides profound insights into the physics of strongly correlated particles. Tuning the effective interaction strength to the moderate correlation regime is expected to stabilize a variety of exotic phases near the Mott transition. A well-known example is the idea that doping a Mott insulator captures the essential physics underlying high transition temperature (Tc) superconductors [5,6]. Developing a controllable platform to simulate Hubbard model physics and high-Tc phenomenology is highly desirable, as it could offer new perspectives on the high-Tc problem and guide the design of next-generation high-temperature superconductors.

In this study, we investigate the electrical transport properties of a 3.65° twisted bilayer WSe2 (tWSe2) device with tunable carrier density n and out-of-plane electric field E. Our measurements establish the electrostatic phase diagram for tWSe2 at moderate correlation regime. At half-band filling, a Mott insulator is observed, with its correlation strength effectively controlled by the electric field. Upon approaching the metal-insulator transition near zero E field—where the hopping amplitude t becomes comparable with the onsite interaction U—we observe robust superconductivity.

The optimal superconducting temperature is about 200 mK, corresponding to about 1-2% of the effective Fermi temperature. This ratio is comparable to that of high-temperature cuprate superconductors and suggests strong pairing.

Figure 1 shows the device schematics (a) and its optical image (b). The encapsulated twisted bilayer WSe2 is directly transferred onto prepatterned Pt electrodes. The dual-gated geometry enables independent tuning of n and E. Additional contact and split gates, deposited atop the full stack, are implemented to achieve low contact resistances and eliminate unwanted parallel conduction channels. The Hall-bar geometry is defined by all four gates, including the top, bottom, contact and splitting gates. Electrical transport measurements are performed in a dilution refrigerator, equipped with low-temperature resistor-capacitor and radiofrequency filters mounted on the mixing chamber plate to attenuate electrical noise from about 65 kHz to tens of gigahertz. Low-frequency (5.777 Hz) lock-in techniques are employed to measure sample resistance using a small excitation current (<10 nA) to avoid sample heating.

Figure 2 shows the longitudinal resistance R measured as a function of moiré filling factor v and E (a) and a zoom-in phase diagram near half-band filling (v=1) and zero E field (b). In the electrostatic phase diagram, the layer-shared (inner) and layer-polarized (outer) regions are delineated by dashed lines. In the layer-shared region, the van Hove singularity (vHS), characterized by a diverging density of states (DOS), is identified as a high-resistance feature traced by the red curve. Overall, the phase diagram aligns well with the single-particle expectation, except for the correlated insulating states observed at commensurate fillings v=1/4,1/3,1. Notably, at v=1, a robust zero-resistance phase emerges at the verge of the correlated insulator near zero E field.

140 Cornell NanoScale Facility

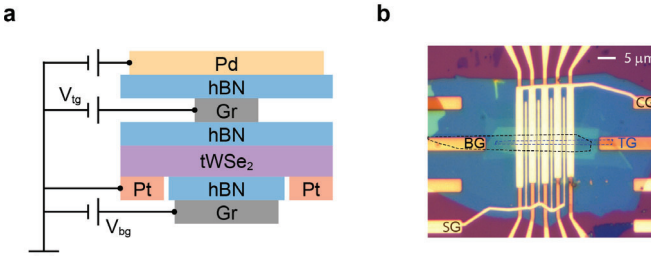


Figure 1: a, Schematic of the device structure. b, Optical microscope image of a 3.65° tWSe2 device. Scale bar is 4 µm.

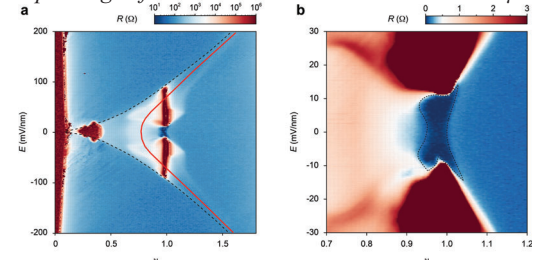


Figure 2: a, Longitudinal resistance R as a function of moiré filling factor v and electric field E. b, Zoom-in phase diagram near half-band filling and zero E field.

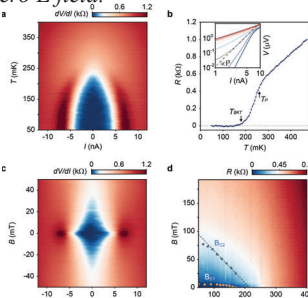


Figure 3: a, Differential resistance dV/dI as a function of current bias I and temperature T. b, Zero-bias resistance R as a function of T Insert: I-V characteristics at varying T c, Differential resistance dV/dI as a function of I and magnetic field B d, Zero-bias resistance R as a function of T and B.

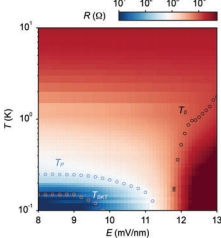


Figure 4: Zero-bias resistance R as a function of E and T, showing an electric-field-induced superconductor-insulator transition at v=1.

Figure 3 further investigates the differential conductance of the zero-resistance phase under applied perpendicular magnetic fields at elevated temperature. Figure 3a shows the differential resistance dV/dI as a function of bias current I and temperature T. The critical current is I_c=5 nA at T=50 mK and gradually decreased to zero near 250 mK. The corresponding zero-bias resistance R as a function of T is shown in Figure 3b, revealing

a Berezinskii–Kosterlitz–Thouless (BKT) transition temperature T_{BKT} =180 mK and a pairing temperature T_p =250 mK. Figure 3c shows dV/dI as a function of I and magnetic field B. Figure 3d shows zero-bias resistance R as a function of B and T, from which the critical fields B_{c1} and B_{c2} are identified.

A linear fit to
$$B_{c2} = \frac{\Phi_0}{2 \pi \xi^2} \left(1 - \frac{T}{T_p} \right)$$

shown as the dashed line, gives rise to a superconducting coherence length $\xi \approx 52$ nm, which is about 10 times the moiré period $a_M \approx 5$ nm (Φ_0 denotes the magnetic flux quantum).

Figure 4 shows R as a function of E and T, revealing an electric-field-induced superconductor-insulator transition at v=1. The critical temperatures $T_{\rm BKT}$ and $T_{\rm p}$ are indicated on the superconducting side and the extracted thermal activation gaps $T_{\rm 0}$ are plotted on the insulating side. All characteristic temperature scales vanish continuously as E approaches the critical field $E_{\rm c}{\approx}11.7~{\rm mV}$ / nm, indicating a continuous quantum phase transition.

Conclusions and Future Steps:

We observe robust superconductivity in tWSe₂, emerging at the verge of correlated insulating state at v=1. The continuous superconductor-insulating transition highlights the delicate interplay between the kinetic energy t and on-site interaction U, resembling the physics of high- T_c cuperate superconductors. A superconducting transition temperature to Fermi temperature ratio (T_c/T_f) of 1-2%, along with a short coherence length $\xi/a_M \approx 10$ (both comparable to values in cooperate superconductors), further suggest strong pairing. Our findings motivate further investigations into questions such as the superconducting pairing symmetry and underlying pairing mechanism.

- [1] Tang, Y. et al. Nature 579, 353-358 (2020)
- [2] Regan, E. C. et al. Nature 579, 359-363 (2020)
- [3] Anderson, P. W. Science 235, 1196-1198 (1987)
- [4] Hubbard, J. Proc. R. Soc. A 276, 237-257 (1963)
- [5] Lee, P. A., Nagaosa, N., Wen, X.-G. Reviews of Modern Physics 84, 1383-1417 (2012)
- [6] Imada, M., Fujimori, A., Tokura, Y. Reviews of Modern Physics 70, 1039-1263 (1998)

Thermodynamic evidence of fractional Chern insulator in moiré MoTe,

CNF Project Number: 263318

Principal Investigator(s): Kin Fai Mak, Jie Shan

User(s): Zhengchao Xia, Yihang Zeng, Kaifei Kang, Bowen Shen, Jiacheng Zhu,

Patrick Knüppel, Chirag Vaswani

Affiliation(s): Laboratory of Atomic and Solid State Physics, School of Applied and Engineering Physics, Kavli Institute at Cornell for Nanoscale Science; Cornell University

Primary Source(s) of Research Funding: DOE, NSF, AFOSR, GBMF

Contact: jie.shan@cornell.edu, kinfai.mak@cornell.edu, zx287@cornell.edu, yz425@cornell.edu, kk726@cornell.edu, bs792@cornell.edu, jz969@cornell.edu, pk439@cornell.edu, cv246@cornell.edu

Website: https://sites.google.com/site/makshangroup/

Primary CNF Tools Used: Zeiss Supra SEM, Nabity Nanometer Pattern Generator System (NPGS), Angstrom E-Beam Evaporator, SC4500 Odd/Even-Hour Evaporator, Autostep i-line Stepper, Hamatech Wafer Processor Develop, Heidelberg Mask Writer - DWL2000, Photolithography Spinners, Dicing Saw – DISCO, Yes Asher

Abstract:

Fractional Chern insulators are the lattice analogues of the fractional quantum Hall effects, characterized by Hall conductance quantized to rational fractional multiples of e²/h in the absence of external magnetic field or Landau levels [1, 2, 3]. By employing a new technique to optically readout the local thermodynamics [4], we discover thermodynamic evidence of both integer and fractional Chern insulators in a 3.4° twisted homobilayer MoTe, moiré device. Specifically, we obtain local electronic compressibility through a monolayer semiconductor sensor capacitively coupled to the tMoTe2 moiré and show that the correlated insulators at hole filling factors v = 1 and 2/3 spontaneously break time-reversal symmetry. We further demonstrate that they are integer and fractional Chern insulators with Chern numbers 1 and 2/3, respectively, from the dispersion of the insulating states in moiré filling with applied magnetic field. Our findings pave pathways for uncovering other new fractional topological phases and demonstrating the fractional statistics in moiré semiconductor materials.

Summary of Research:

Fractional topological phases represent a unique class of quantum states that combine strong interactions with nontrivial band topology. Transition-metal dichalcogenide (TMD) semiconductor moiré materials, which support tunable topological flat bands, provide a highly tunable platform for realizing fractional topological phases [5, 6]. Our experiment demonstrates that, in 3.4° tMoTe2 moiré, the correlated-insulating states at hole filling v = 1 and 2/3 are integer and fractional Chern insulators.

Figure 1 illustrates the schematic of a dual-gated 3.4°

twisted homo-bilayer MoTe2 device with a monolayer WSe2 sensor for thermodynamic measurements. Inset shows the schematic of tMoTe2 lattices. The twisted bilayers form a honeycomb moiré superlattice, with two sublattices (red and blue) residing in two different layers. Mo atoms in the top layer are aligned with Te atoms in the bottom layer at the red sublattice sites, and the arrangement is reversed at blue sublattice sites.

We employ our newly developed technique to optically readout the local thermodynamics of tMoTe2 moiré. Figure 2(a) exhibits a simplified measurement scheme. A monolayer semiconductor sensor (green) is capacitively coupled to the sample (blue), allowing an interlayer bias Vs to be applied between sample and sensor. For each measurement, sensor chemical potential is actively adjusted through a feedback circuit to lock the reflection count at a chosen reference point. The amount of adjustment directly reads the chemical potential μ of the sample.

Figure 2(b) shows an example reflectance spectrum as a function of WSe_2 sensor chemical potential (tuned by V_{bg}). The neutral exciton resonance peak quenches rapidly upon electron doping near 4.69V. In Figure 2(c) the integrated photon count drops sharply upon electron doping, enabling accurate determination of WSe2 band edge, making it a natural reference point. During each measurement, V_{bg} is tuned through a feedback loop to lock the reflection count the chosen reference point (vertical dashed line). As shown in Figure 2(d), under this arrangement, sensor chemical potential (dashed green line) is kept at sensor conduction band edge, while sample chemical potential (dashed blue line) is at eVs below it, with μ =0 defined at the moiré band edge. Therefore, sample's chemical potential is given by

$$\mu/e = , \ \left(1 + \frac{C_{\text{bg}}}{C_{\text{s}}}\right) V_{\text{S}}, - \ \frac{C_{\text{bg}}}{C_{\text{s}}} \ V_{\text{bg}},$$

where $C_{\rm bg}$ and $C_{\rm s}$ are the bottom-gate-to-sensor and sensor-to-sample geometrical capacitances, respectively.

We apply this technique to the 3.4° tMoTe₂ moiré device shown in Figure 1. Figure 3(a) and (b) show moiré chemical potential (μ) and incompressibility ($d\mu/dv$) as a function of doping density (v), respectively, when the moiré is tuned to near zero interlayer potential dfference (E \approx 0). The steps in chemical potential, or peaks in incompressibility, correspond to insulating states at v = 1, 2/3 and 2. Figure 3(c) and (d) shows the magnetic circular dichroism (MCD) as a function of perpendicular magnetic field (B) at v = 1 (c), and v = 2/3 (d). Spontaneous magnetization and magnetic hysteresis can be clearly identified for both states, indicating that correlated insulators at v = 1 and 2/3 spontaneously break time reversal symmetry.

Figure 4(a) shows the electronic incompressibility as a function of v and B at $E \approx 0$. We observed that the incompressible states at v = 1 and 2/3 disperse linearly with B. Empty circles denote the center of mass of the incompressibility peaks. Filled circles in Figure 4(b) mark the corrected dispersion with respect to a trivial Mott insulator at large E. Linear fits to the corrected dispersions are denoted by the solid lines in Figure 4(b), which yield the quantum numbers (t, s) according to the Diophantine equation

$$\mathbf{v} = \mathbf{t}^{\frac{e}{h}\frac{B}{n_{M}}} + \mathbf{s}$$

We conclude that for v = 1, $t = 1.0 \pm 0.1$ (corresponding to Chern number 1), while for v = 2/3, $t = 0.63 \pm 0.08$ (corresponding to Chern number 2/3).

Conclusions and Future Steps:

By employing the optical readout of local chemical potential on a 3.4° tMoTe2 device, we obtain thermodynamic evidence of fractional Chern insulators at v = 2/3, with Chern number 2/3. Our results indicate that TMD moiré flat bands can host topologically ordered states carrying fractionalized excitations in the absence of magnetic fields.

References:

Tang, Y. et al. Nature 579, 353-358 (2020) 2. Regan, E. C. et al. Nature 579, 359-363 (2020) 3. Anderson, P. W. Science 235, 1196-1198 (1987) 4. Hubbard, J. Proc. R. Soc. A 276, 237-257 (1963) 5. Lee, P. A., Nagaosa, N., Wen, X.-G. Reviews of Modern Physics 84, 1383-1417 (2012) 6. Imada, M., Fujimori, A., Tokura, Y. Reviews of Modern Physics 70, 1039-1263 (1998).

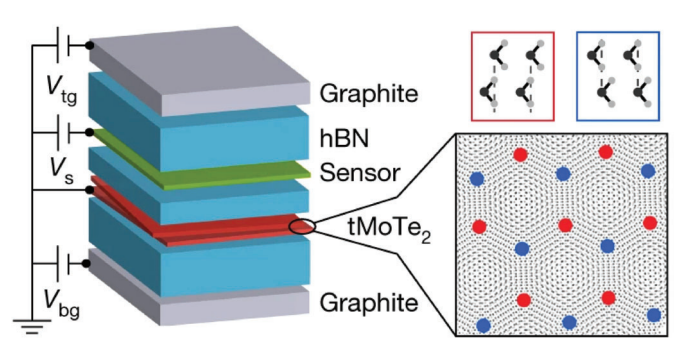


Figure 1: Device schematic. Inset: schematic representation for tMoTe, moiré lattice.

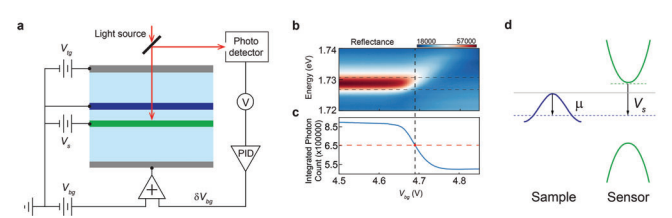


Figure 2: a, schematic for optical measurement of thermodynamics in a typical dual-gated device. b, $V_{\rm bg}$ dependence of reflectance contrast near monolayer WSe2 sensor's neutral exciton resonance. c, spectrally integrated photon counts over the window in b horizontal dashed lines) as a function of $V_{\rm bg}$. d, schematic of the band alignment.

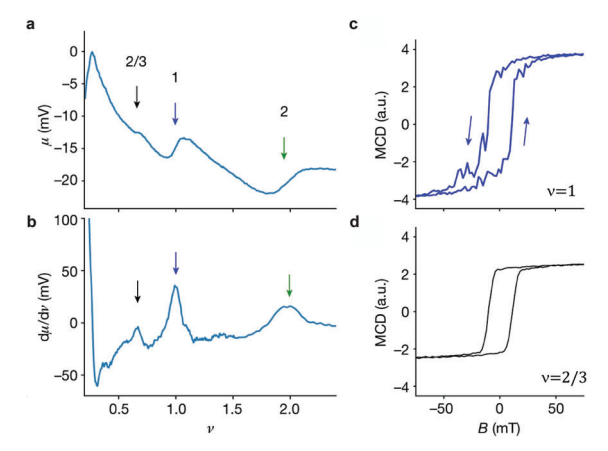


Figure 3: a, b, chemical potential (a) and charge incompressibility (b) as a function of tMoTe₂ moiré filling (v). c, d, MCD as a unction of B at v = 1 (c) and v = 2/3 (d). All measurements performed at $E \approx 0$.

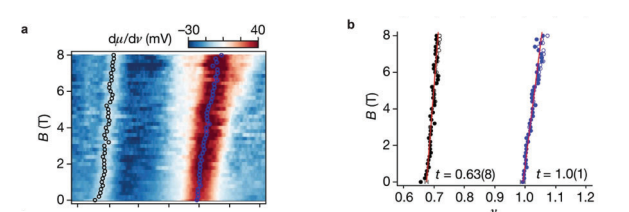


Figure 3: a, b, chemical potential (a) and charge incompressibility (b) as a function of tMoTe, moiré filling (v). c, d, MCD as a unction of B at v = 1 (c) and v = 2/3 (d). All measurements performed at $E \approx 0$.

Investigating the Impact of an External Electric Field on Thermal Behavior

CNF Project Number: 275819

Principal Investigator(s): Zhiting Tian User(s): Amelia Schaeffer, Aloyse Maille

Affiliation(s): Sibley School of Mechanical and Aerospace Engineering; Cornell University

Primary Source(s) of Research Funding: Office of Naval Research Contact: zt223@cornell.edu, afs97@cornell.edu, aam299@cornell.edu

Website: https://ztgroup.org/

Primary CNF Tools Used: ABM Contact Aligner, SUSS MA6-BA6 Contact Aligner, SC4500 Odd-Hour Evaporator, Glen 1000 Resist Strip, Everbeing EB-6 DC Probe Station

Abstract:

As electronics continue to scale to smaller dimensions and increased power densities, understanding how electric fields impact the thermal properties of materials becomes important for accurate thermal budgeting. In this work, we fabricate structures to study how thermal properties of hexagonal boron nitride (hBN) change when a cross-plane electric field is applied to the material. Microscale capacitors with Ti/Au contacts were fabricated using dry transfer, contact photolithography, electron-beam evaporation, and liftoff processing. Thermal measurements of the devices under applied external fields are ongoing.

Summary of Research:

To perform thermal measurements, a lateral hBN flake dimension of at least 80 μm is desirable, and thicker flakes are selected to help limit the influence of the interfaces on thermal measurements. (Bulk samples are not used since a single-crystal domain is necessary to eliminate the effect of grain boundaries.) Compared to typical 2D material flakes used for device fabrication, these flakes have much larger lateral dimensions (~100 μm x ~100 μm) and are thicker (~100 nm or thicker). This, combined with the electrode dimensions, allows us to utilize contact photolithography to pattern our electrodes, a technique not typically used for 2D flakes.

Mask design, mask writing, and photolithography dose testing were all performed as initial steps in the device development process. To make a wafer of devices, the bottom electrodes are patterned, metal is deposited, and liftoff is performed. After the bottom electrode is set, dry transfer is used to precisely place hBN flakes. Then, the top electrode is patterned on top of the flake, and deposition and liftoff are repeated. Sonication cannot be used at any step once the flakes are placed, as it can lead to delamination. An example of a fully fabricated device is shown in Fig. 1.

Some iteration on this general process was necessary to ensure repeatable and high quality results. The initial wafer of devices run showed contaminants on the flake that affected the top electrode, and atypical aging of the gold used for both the top and bottom electrodes was observed. An oxygen plasma resist strip and a more aggressive substrate clean prior to processing resolved these two issues, respectively. A comparison of a device from the first wafer and one from the second wafer, after these changes have been implemented, is shown in Fig. 2.

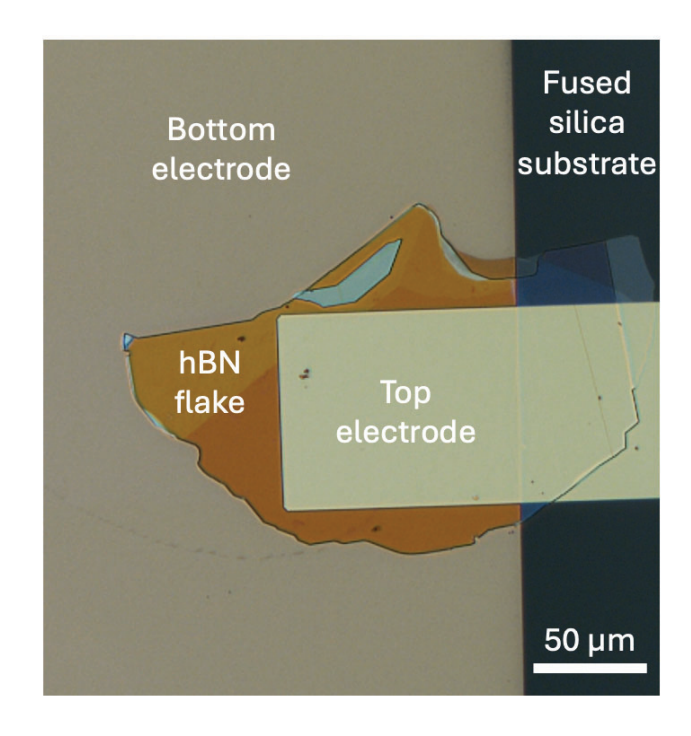
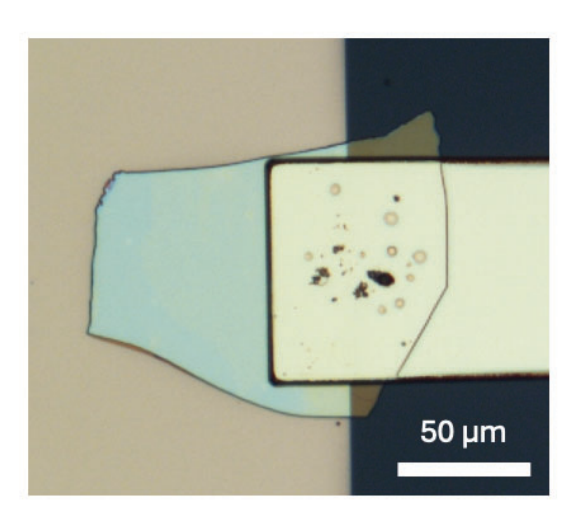


Figure 1: An optical microscope image of a fully-fabricated device with structures labelled for clarity. Both the top and bottom electrodes are Au with a Ti adhesion layer, but the difference in appearance is due to different thicknesses of Au.

First Wafer



Second Wafer

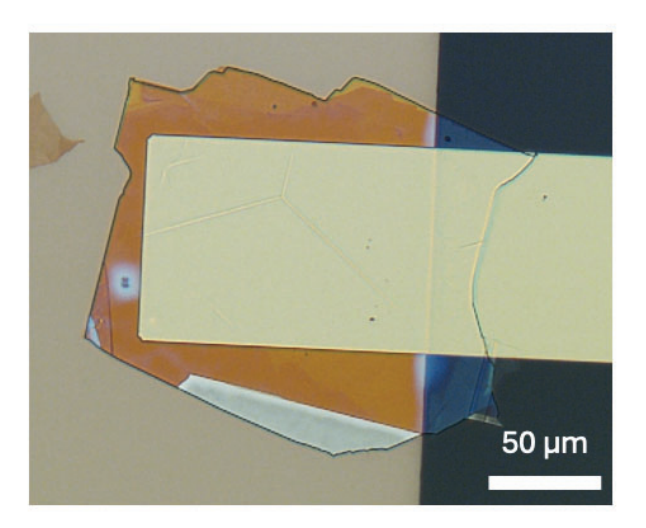


Figure 2: Two optical microscope images showing a device on the first wafer fabricated without additional cleaning steps and a device on the second wafer where more robust substrate cleaning and an oxygen plasma clean immediately prior to top electrode deposition helped to eliminate residues present on the first wafer.

Conclusions and Future Steps:

A repeatable and effective fabrication method has been developed for these devices that ensures well-defined contacts and clean surfaces. These devices are now undergoing thermal measurements while fields are applied, and future steps will be informed by the experimental results obtained from these measurements.

Thin-Film Deposition for Surface Characterization Studies for Superconducting Radio Frequency Cavity Application

CNF Project Number: 2779-19

Principal Investigator(s): Matthias Liepe

User(s): Nathan Sitaraman

Affiliation(s): Cornell Laboratory for Accelerator-based Sciences and Education, Cornell University

Primary Source(s) of Research Funding: The U.S. National Science Foundation under Award PHY-1549132, the

Center for Bright Beams

Contact: mul2@cornell.edu, nss87@cornell.edu Website: https://physics.cornell.edu/matthias-liepe Primary CNF Tools Used: AJA Sputter Deposition 1 & 2

Abstract:

Superconducting radio-frequency (SRF) cavities are a key component of particle accelerators (with applications ranging from fundamental physics research to synchrotron X-ray sources, to e-beam microscopy and lithography) and are also being developed for applications in dark matter detection and quantum computing. We are developing next-generation surface treatments to enhance the performance of niobium superconducting surfaces. By using facilities at the CNF, we investigate the effect of metallic doping on the niobium surface. We highlight our recent success in growing Nb3Al and Nb-Zr superconducting alloys.

Summary of Research:

We used CNF's AJA sputter deposition tools to deposit zirconium on niobium samples for Nb-Zr alloy growth. This builds on our earlier development of a zirconium oxide capping layer recipe using the same CNF tool. We are still working to develop a recipe that achieves the optimal composition for superconducting performance. Additionally, we used the same tools to deposit aluminum on niobium samples for Nb3Al layer growth. We were able to verify the presence of Nb3Al on samples by Tc measurement and x-ray diffraction at CCMR.

Conclusions and Future Steps:

We prepared a large sample plate with Nb3Al, following the same recipe that was successful on small samples, and this sample plate has successfully been assembled into our RF testing setup for data collection. The results of this test will help guide future work on Nb3Al for SRF applications. In parallel, we will continue development of an Nb-Zr alloy recipe.

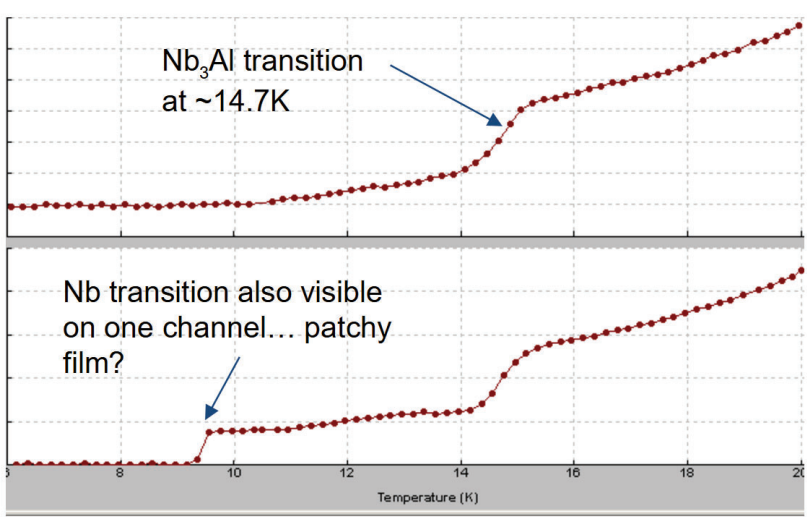


Figure 1: Resistance vs temperature data on first successful Nb3Al-on-Nb sample.

Enhancement of laser plasma driven ion acceleration using dielectric metasurfaces

CNF Project Number: 2979-21

Principal Investigator(s): Gennady Shvets

User(s): Samyobrata Mukherjee

Affiliation(s): School of Applied and Engineering Physics, Cornell University

Primary Source(s) of Research Funding: Carbon Ion Radiation Therapy (E903324), NSF project: "Interaction of Ultra-

Intense Laser Pulses with Structured Targets in the Multi-Petawatt Regime" (E71-8417)

Contact: gshvets@cornell.edu, sm2575@cornell.edu

Website: http://shvets.aep.cornell.edu

Primary CNF Tools Used: JEOL 6300, SC4500 Evaporator, Unaxis 770 Etcher, SUSS MA6-BA6 Contact Aligner, Oxford 82 Etcher, Oxford PECVD, KLA P7 Profilometer, Zeiss Supra SEM, Heidelberg Mask Writer DWL-2000, Hamatech Mask Processor, E-beam and Photolithography Spin Coaters, Resist Hot Strip Bath, Hamatech Wafer Processor, Anatech Resist Strip, FilMetrics.

Abstract:

We aim to study the acceleration of heavy ions generated by the interaction of high-power ultrashort laser pulses with structured solid targets. We compare the yield of heavy ions produced by laser pulses incident on thin flat silicon oxide (SiO2) membranes with the yield from structured silicon metasurfaces resting on similar SiO2 membranes. Simulations as well as preliminary experiments carried out at the ALEPH laser facility in Colorado State University reveal that we obtain a greater flux of higher energy ions from the structured targets. Such high charge/flux heavy ion beams may have applications in diverse areas including cancer therapy and high-flux neutron generation.

Summary of Research:

Ultrashort, high intensity pulsed lasers have enabled the creation of tabletop ion accelerators which rely on a driving electron component and the resulting electric field created by charge separation. A typical mechanism involves target normal sheath acceleration (TNSA) where a laser beam incident on a solid thin foil target creates an electron sheath on the rear of the target which generates highly energetic ions. The incident laser pulse generates hot electrons which penetrate the foil and while a few electrons escape, the target's capacitance traps most of the electrons which end up forming a charge-separation field. At the rear surface, the electric field is strong enough to ionize atoms, and it accelerates the ions in a direction normal to the surface.

We are investigating a scheme to enhance the acceleration of the heavy ions compared to standard TNSA from a foil target by structuring the target. Specifically, we create arrays by patterning a silicon layer which lies on a thin (~1 µm) silicon oxide membrane. Blocks of silicon comprising the array are separated from each other by high aspect ratio trenches. A laser pulse polarized perpendicular to the trench will draw electrons out of the silicon blocks into the trench (see Fig. 1a) and accelerates them to relativistic energies which are far greater than the energies obtained in traditional TNSA, leading to a stronger sheath electric field [1]. Simulations predict that the structured targets will enhance both the energy and flux of the ions produced (see Fig. 1b).

Our targets are produced at the CNF. We start with a buried oxide silicon on insulator wafer and deposit 3 µm SiO2 on the handle layer which will be patterned as a hard mask to etch the substrate. We carry out e-beam lithography on PMMA deposited on the device layer and evaporate Al2O3 on the PMMA after development. The PMMA is then lifted off in acetone and the remaining Al2O3 acts as a hard mask for the anisotropic etching of the device silicon layer in the Unaxis 770 using a customized recipe based on a modified Bosch process. After that we remove the Al2O3 in Al etch and remove polymer coatings on the sidewall using EKC polymer strip. The SiO2 on the handle layer is then patterned via backside aligned photolithography on the MA6 mask aligner followed by etching in the Oxford 82. Finally, the substrate below the silicon arrays is etched on the Unaxis 770 using the standard Bosch process.

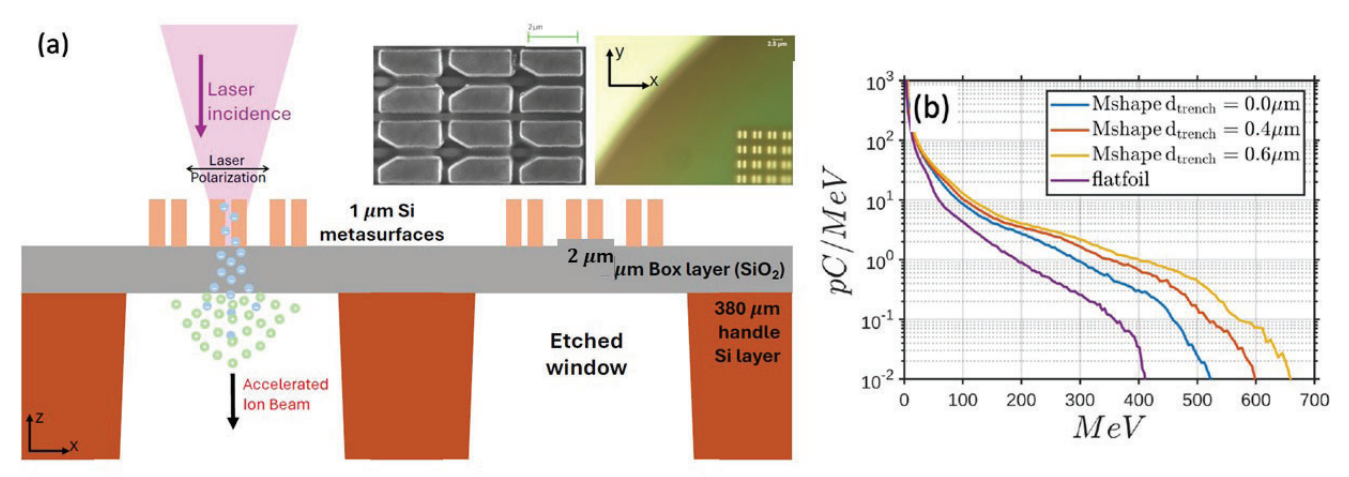


Fig. 1: (a) Schematic showing the laser incident on a structured target on a membrane. The insets show optical and SEM images of two different structured targets. (b) Simulation results predicting higher energy ions from structured targets.

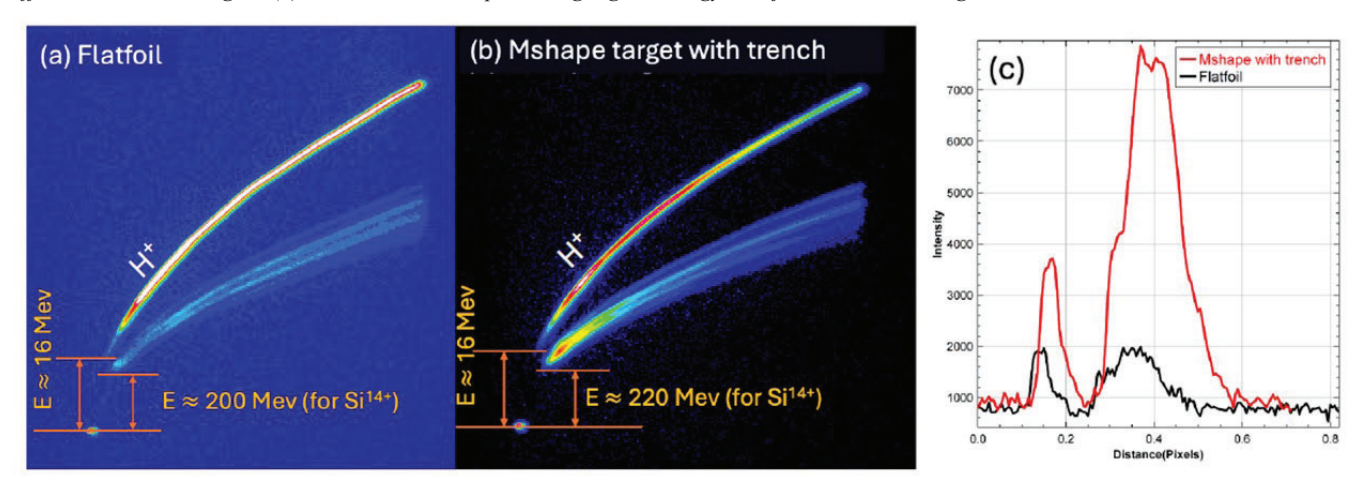


Fig. 2: Thompson parabola spectrometer output showing traces for different ion species with laser incident on (a) flat foil and (b) structured target. (c) Comparison of image intensity at a fixed energy.

Conclusions and Future Steps:

Our proposal was evaluated in a competitive process, and we were awarded beam time at multiple laser facilities across the US (ALEPH at Colorado State University, SCARLET at Ohio State and ZEUS at the University of Michigan). Preliminary results from experiments carried out at the ALEPH facility have shown that the structured targets produce a higher flux of heavy ions at higher energies as recorded on Thompson parabola spectrometers (see Fig. 2). We are currently preparing for further experimental campaigns to confirm our results. To this end we are also updating our target design based on feedback from previous experiments.

References:

[1] Shcherbakov, M. R. et al. Nanoscale reshaping of resonant dielectric microstructures by light-driven explosions. Nat Commun 14, 6688 (2023).

Sensing superconducting film loss via flip chip

CNF Project Number: 299822

Principal Investigator(s): Valla Fatemi

User(s): Haoran Lu

Affiliation(s): Applied and Engineering Physics, Cornell University

Primary Source(s) of Research Funding: AFOSR Contact: vf82@cornell.edu, hl2396@cornell.edu Website: https://fatemilab.aep.cornell.edu/

Primary CNF Tools Used: Heidelberg MLA 150 Maskless Aligner, DWL2000, PT770, ABM contact aligner, SC4500

Even-Hour Evaporator

Abstract:

Superconducting quantum circuits are a leading platform prospective for achieving quantum computation. One bottleneck is the low lifetimes of individual qubits, partially related to the microwave loss associated with the superconducting films. This project focuses on developing a benchmarking scheme that enables detecting the loss of different superconducting thin films (target film) without the involvement of the fabrication on the target film. The scheme is also capable of sensing specific losses in the metal-air interface and in the conductor itself (e.g., due to quasiparticles) before any fabrication steps are taken, thereby isolating these

losses in the 'pristine' state of the material. This serves as a useful benchmark for subsequent work testing devices after nanofabrication.

Summary of Research:

Sensing resonator: In this project, we use a high quality factor superconducting resonator (sensing resonator) to probe a target film. The sensing resonator is fabricated from niobium or tantalum thin films at CNF.

SU8 pillar: To sense the loss of the target film, the sensing resonator must be a few microns away from the target film, with an uncertainty less than half a micron. In this project, we use 4 μ m SU8 pillar. The resist coating, exposure, and development are done in CNF as well.

Target film and measurement: The target film involved in this study includes SiO2 layers on Nb films. The SiO2 layers are deposited using the even-hour evaporator. Preliminary data shows a similar power-dependent quality factor as resonators deposited directly onto SiO2. This is encouraging, as it indicates our novel approach will be able to sense any elevated losses in target films without exposing those films to fabrication processes.

Conclusions and Future Steps:

We developed a scheme combining SU8 and superconducting resonators for target film loss sensing. In the coming months, we will test different materials and share this technique to the community as a better platform to evaluate loss.

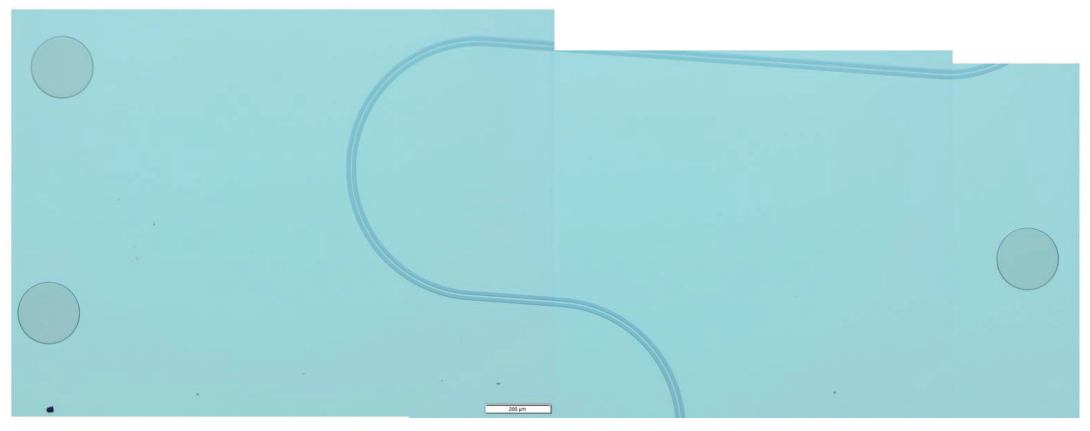


Figure 1: Resonator and pillar (partial).

Improving Quality Factors in Superconducting Resonators

CNF Project Number: 299822

Principal Investigator(s): Valla Fatemi

User(s): Maciej Olszewski (1), JT Paustian (2), Tathagata Banerjee (3), Haoran Lu (3)

Affiliation(s): (1) Cornell University Department of Physics, (2) Syracuse University Department of Physics, (3) Cornell University Applied and Engineering Physics

Primary Source of Research Funding: Air Force Research Laboratory, Laboratory for Physical Sciences

Contact: vf82@cornell.edu, mwo34@cornell.edu Website: https://fatemilab.aep.cornell.edu/

Primary CNF Tools Used: G-Line Stepper, Oxford 81, PT 770, DISCO Dicing Saw, Heidelberg 2000 Mask WriterEven-

Hour Evaporator

Abstract:

Superconducting microwave circuits are one of the leading candidate platforms for enabling quantum computing technology, and Nb on Si is a commonly implemented materials set. Currently one of the main bottlenecks for improving device performance and technological prospects is elimination of defects from the materials and interfaces within the superconducting circuits resulting from nanofabrication processing. In this report, we demonstrate compact (3 µm gap) coplanar waveguide resonators with low-power internal quality factors near one million. We achieve this using a resist strip bath with no post-fabrication acid treatment, which results in performance comparable to previous strip baths with acid treatments. Avoiding post-fabrication acid treatments reduces the aging in our devices by reducing oxide regrowth. We correlate improved performance with a reduction of post-etch contamination as shown by XPS. This work in based on our manuscript [1].

Summary of Research:

Superconducting transmon qubit fabrication involves many steps which have a profound impact on device performance. To better understand how each step impacts the final device quality we use superconducting coplanar resonators as a proxy for full qubit devices. Both devices share many fabrication steps including substrate preparation, superconductor growth, photolithography patterning, metal etching, photoresist removal, and device cleaning.

In this report, we focus on improving superconducting resonator performance by testing various solvents used for resist removal post dry reactive ion etching. To best isolate the impact of resist removal on resonator performance, we prepare devices with identical recipes, except we change the solvent used for resist removal. For this work we focus on comparing MICROPOSIT 1165 (1165) and Integrated Micro Materials AZ 300T (AZ 300T). Both solvents are N-methyl-2-pyrrolidinone based solvents while AZ 300T also contains propylene glycol and tetramethyl ammonium hydroxide (TMAH). Based on our discussions with the vendor, we believe that the addition of TMAH is the key difference in device performance.

After preparing devices with two different nanofabrication recipes, we test our resonators with cryogenic RF measurements at milli-Kelvin temperatures. We extract the internal loss tangents of resonators prepared with both methods. As shown in figure 1, we find a very significant difference in resonator performance between the samples prepared with 1165 and the ones with AZ 300T. This gap in performance is much larger than the fluctuations between devices and is statistically significant.

To better understand the reason behind this gap in performance, we look for physical differences between these devices. Using x-ray photoemission spectroscopy (XPS) we find that the two devices have significant differences in contaminants present on both niobium and silicon surfaces. As shown in figure 2, we find a significant difference in carbon contamination, as well as residue chlorine percentage. These indicate that AZ 300T is better at removing etch residue as compared to 1165, leading to better device performance.

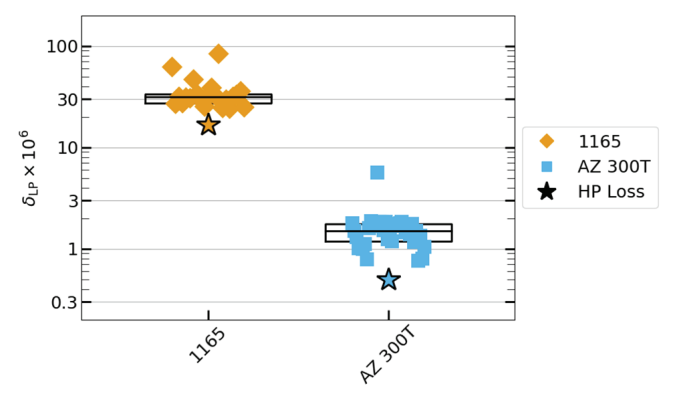


Figure 1 Caption: Boxplot comparing resonator performance with samples made with 1165 and samples made with AZ 300T, with otherwise identical fabrication.

Conclusions and Future Steps:

Our current fabrication procedure yields state of the art resonators as compared to other work in the literature. We plan to continue to further improve the quality of our devices by debugging other areas of our nanofabrication process, including using other materials, trying new etching recipes, and exploring new resist removers.

Further, we also plan on incorporating our improved devices into full transmon qubit devices by incorporating Josephson junctions into our recipe. The improvements in resonator performance should directly translate to better qubit performance, improving lifetimes. We plan to conduct a similar study on improving qubit performance through optimizing our nanofabrication procedure.

References:

[1] https://arxiv.org/abs/2503.13285

Surface	Si						Nb			
Element	С	Ca	Cl	N	Na	F	С	Na	Si	F
Pre-strip	10.3	-	1.4	0.8	-	-	/	/		
AZ300T	6.5	_	-	_	-	-	11.5	0.2	-	-
NMP	8.9	_	1.1	0.9	-	-	18.0	-	1.0	-
PGMEA	6.8	0.4	1.0	_	0.3	1	33.9	-	-	-
1165	7.9	-	1.0	1.0	-	-	19.3	-	1.0	-

Figure 2 Caption: XPS data with contamination of various surfaces post-resist removal with various solvents

Manufacturing SiN Bullseye Cavities & SOI Photonic Crystal Nanobeam Cavities

CNF Project Number: 300822

Principal Investigator(s): Professor Pablo A. Postigo User(s): Christopher (Christer) Everly, Martin Sanchez

Affiliation(s): Institute of Optics, University of Rochester

Primary Source of Research Funding: UoR Startup, URA Award 2023-2024 from University of Rochester

Contact: ppostigo@ur.rochester.edu, ceverly@ur.rochester.edu, msanch23@ur.rochester.edu

Website: https://www.postigolab.com

Primary CNF Tools Used: JEOL 6300, JEOL 9500, E-beam Spin Coaters, Olympus MX-50 Microscopes, Oxford 82, Oxford 100, PT770 RIE, Oxford Cobra ICP, Plasma Therm Tikachi HDP-CVD, Oxford PECVD, Primaxx Vapor HF Etcher, Yes EcoClean Asher, Yes Asher, Filmetrics systems, Zeiss Ultra SEM, Zeiss SEM Supra, Veeco AFM, Disco Dicer Saw

Abstract:

Our group is interested in quantum research on photonic platforms. Some topics we are currently exploring include: on-chip lasing and single-photon emission enhancement with circular Bragg gratings, and room temperature single phonon quantum sensing using phononic crystal enhanced optomechanical cavities. We have designed, fabricated, and tested Purcell enhanced Bragg cavities, as well as various photonic crystal optical nanocavities, and phononic crystal enhanced mechanical resonators.

Summary of Research:

Users have done diligent work to refine the fabrication process for the circular Bragg grating (CBG) cavity, colloquially referred to as a bullseye cavity. A deposition recipe was developed on the Oxford PECVD that achieves repeatable SiO2 followed by SiN deposition thicknesses. Experimentation was completed on different gas pressures during inductively coupled plasma (ICP) etching of silicon nitride in order to achieve the high aspect ratio, anisotropic etches required for the silicon nitride (SiN) bullseye cavities.

Additionally, the group has created our first fabrication procedure for creating suspended structures including: photonic crystal nanobeams, photonic crystal L and H cavities, and megahertz phononic crystal arrays. Due to the fine transverse structures required to make photonic crystal nanobeam cavities specifically, experimentation has been done with E-beam resist type, thickness, and dosage applied in lithography machines to match designed requirements. Experimentation was also completed on applying a varied bias to different regions in pattern files in order to account for reactive ion

etch lag (RIE lag) affecting the transverse dimensions of nanostructures differently than larger structures. Different chemistries have been attempted in the lab to create anisotropic silicon etches during pattern transfer with great successes being achieved with a Hydrobromic Acid (HBr) inductively coupled plasma (ICP) etch, instead of the sulfur hexafluoride and oxygen (SF6/O2) chemistry frequently seen in literature for silicon etches. Finally, experimentation was completed with vapor hydrogen fluoride (HF) etching to successfully create suspended structures free of stiction. This was successful for suspended features in the tested range of tens to hundreds of microns. Photonic crystal cavities from these fabrications have been successfully tested and are undergoing further experiments.

Conclusions and Future Steps:

Optical characterization of bullseye cavities has been conducted with great success indicating that our fabrication process is adequate to achieve the desired sub 100nm dimensions required for our designed bullseyes cavities.

We are constantly modifying and improving our designs of the photonic crystal cavities for optomechanics. Many of these designs push the limits of transverse dimensions achievable these types of cavities. Next steps would include fabricating the modified photonic crystal cavities and testing the limits of transverse dimensions achievable in our transverse structures.

Cornell NanoScale Facility

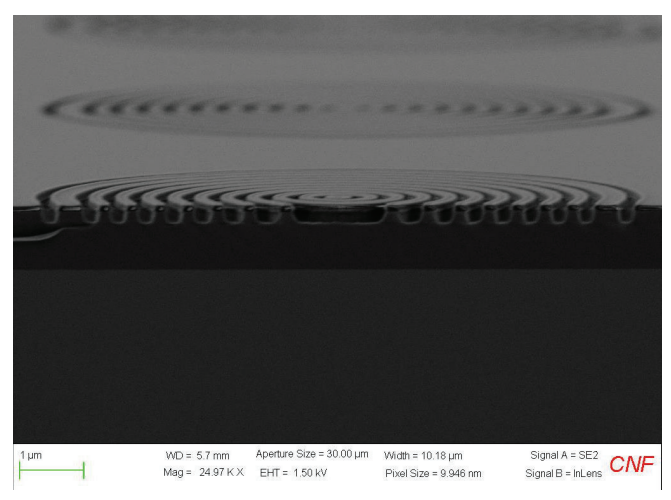


Figure 1: Cross-section of a bullseye cavity.

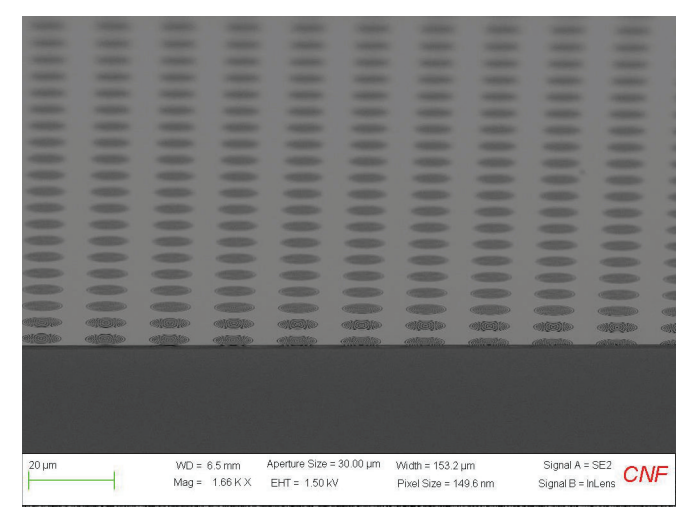


Figure 2: Array of bullseye cavities

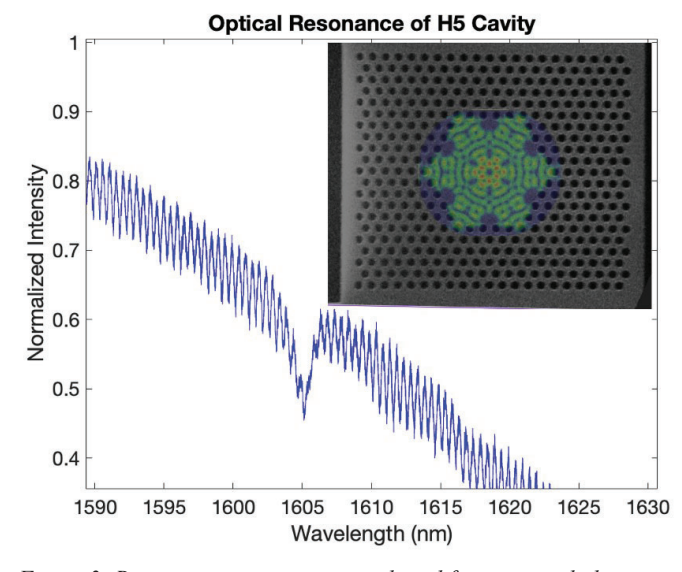


Figure 3: Resonant scatter spectrum plotted for measured photonic crystal H5 cavity, inset: microscope image of H5 cavity taken with Zeiss SEM Ultra, overlayed by simulated resonant mode profile of electromagnetic field norm.

- [1] Room-Temperature Lasing in Colloidal Nanoplatelets via Mie-Resonant Bound States in the Continuum
- [2] Mengfei Wu, Son Tung Ha, Sushant Shendre, Emek G. Durmusoglu, Weon-Kyu Koh, Diego R. Abujetas, Jose A. Sánchez-Gil, Ramón Paniagua-Domínguez, Hilmi Volkan Demir, and Arseniy I. Kuznetsov Nano Letters 2020 20 (8), 6005-6011 DOI: 10.1021/acs.nanolett.0c01975
- [3] Enhanced Emission from WSe2 Monolayers Coupled to Circular Bragg Gratings Ngoc My Hanh Duong, Zai-Quan Xu, Mehran Kianinia, Rongbin Su, Zhuojun Liu, Sejeong Kim, Carlo Bradac, Toan Trong Tran, Yi Wan, Lain-Jong Li, Alexander Solntsev, Jin Liu, and Igor Aharonovich ACS Photonics 2018, 3950-3955 DOI: 10.1021/ acsphotonics.8b00865
- [4] Exploring Regenerative Coupling in Phononic Crystals for Room Temperature Quantum Optomechanics Lukas M. Weituschat, Irene Castro, Irene Colomar, Christer Everly, Pablo A. Postigo, & Daniel Ramos Scientific Reports 14, Article number: 12330 (2024) DOI: https://doi.org/10.1038/ s41598-024-63199-1
- [5] Resolved-sideband cooling of a micromechanical oscillator A. Schliesser, R. Rivière, G. Anetsberger, O. Arcizet, & T.J. Kippenberg Nature Physics 4, 415-419 (2008) DOI: 10.1038/nphys939



Figure 4: Microscope images taken with Zeiss SEM Ultra (left) image of dual nanobeams showing some transverse dimensions (right) dual nanobeams intentionally broken to show fully etched photonic crystal holes with intact suspended nanobeams in the background

Fabrication of Fluxonium-Like Qubits

CNF Project Number: 301022

Principal Investigator(s): Ivan Pechenezhskiy User(s): Benjamin Byrd, Kesavan Manivannan

Affiliation(s): Department of Physics, Syracuse University

Primary Source of Research Funding: Syracuse University, Army Research Office

Contact:ivpechen@syr.edu

Website: https://www.postigolab.com, babyrd@syr.edu, kmanivan@syr.edu

Primary CNF Tools Used: ASML DUV Stepper, JEOL 6300, PT770 Plasma Etcher, Oxford81

Etcher, Heidelberg DWL2000 Mask Writer

Abstract:

We fabricate fluxonium qubits to probe the behavior of broken cooper pairs (quasiparticles) in superconducting circuits and to study the effect of measurement-induced state transitions (MIST) [1]. To probe the quasiparticle population in our qubits, we fabricate Josephson junctions on the perimeter of the devices, which are biased beyond their superconducting gap, controllably generating a reproducible population of quasiparticles in the sample. Probing the qubit state with large numbers of photons can force the qubit outside of it's computational subspace, inducing the aforementioned MIST. The fluxonia for this project are fabricated using a previously reported recipe [2].

Summary of Research:

A fluxonium qubit (Fig. 1) is a superconducting circuit which is comprised of a 2-D capacitor shunted by a small Josephson junction and a 2-D inductor formed of a chain of larger Josephson junctions (Fig. 2). This device forms a loop through which a magnetic field is applied. At specific amounts of magnetic flux passing through this loop, various loss mechanisms which negatively impact qubit performance are suppressed. These qubits are capacitively coupled to a microwave resonator, whose fundamental mode shifts conditional on the state of the qubit. We measure microwave transmission near this frequency as a proxy for the measurement of the qubit state. Our devices are fabricated on Si wafers. All large features, capacitors, coplanar waveguides, and microwave resonators, are patterned into a \sim 70nm niobium base layer using the ASML DUV stepper and the PT770. After initial processing, the devices are cleaned in the CNF hot strip bath, the Glen1000, then in a bath of buffered oxide etch. To form Josephson junctions for both the inductive shunt and the small junction, electron beam lithography using the JEOL 6300 is required. The small junctions for our fluxonia are on the order of $\sim 100 \, \text{nm} \times 100 \, \text{nm}$, and $\sim 1 \, \text{um} \times 1 \, \text{um}$ for 1 each of the ~ 200 junctions in the chain. After electron beam patterning is complete, the junctions are formed by electron beam evaporation using the Dolan bridge technique at Syracuse University.

In the last year, we developed a new fluxonium design with the primary goal of increasing readout fidelity enormously. These design changes are also intended to enable improved characterization of measurementinduced state transitions (MISTs) in our qubits by enabling discrimination between states outside of the typical computational subspace. To achieve this, we increased the coupling between the microwave resonators used for readout and the transmission line used for S21 measurements. We also increased the qubit/ resonator coupling from previous generations of samples fabricated at the CNF. Both of these changes, in addition to minor tweaks to various other circuit parameters, were implemented on our most recent generation of devices. Fabrication quality plays a direct role in our understanding of MIST, in that defects referred to as two-level systems contribute strongly to MIST effects, and give us a window to compare our fabrication quality to the state-ofthe-art. To fully leverage the new design, additional fine-tuning of the fabrication and preliminary characterization are required.

156 Cornell NanoScale Facility

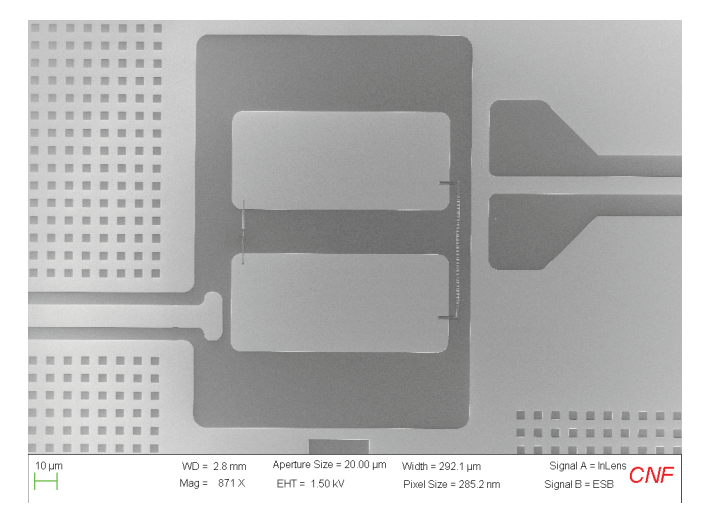


Figure 1: Scanning electron microscopy (SEM) image of one of the fluxonium qubits taken at CNF.

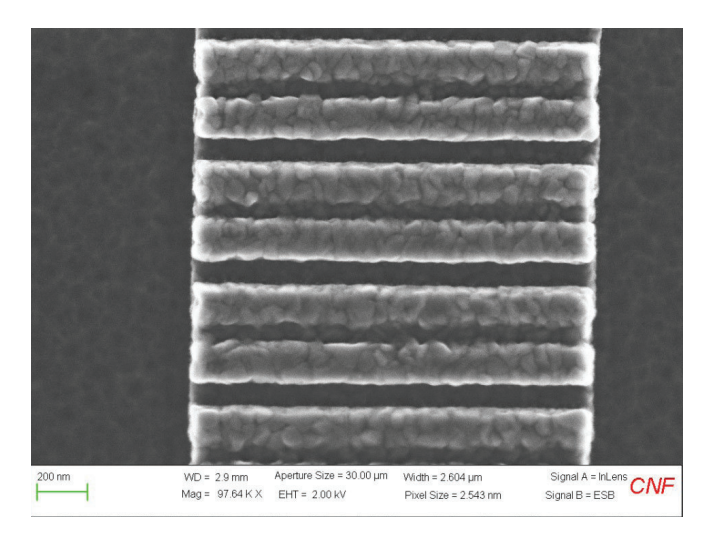


Figure 2: SEM image of a Josephson junction chain, taken at CNF.



Figure 3: Photograph of a sample set into the holder wire-bonded for low-temperature measurements.

- K. Nesterov et al. Measurement-Induced State Transitions in Dispersive Qubit-Readout Schemes.
 Phys. Rev. Appl. 22, 064038 (2024). https://doi.org/10.1103/ PhysRevApplied.22.064038
- [2] V. Iaia et al. Phonon downconversion to suppress correlated errors in superconducting qubits. Nature Communications 13, 6425 (2022). https://doi. org/10.1038/s41467-022-33997-0
- [3] M. Randeria et al. Dephasing in Fluxonium qubits from Coherent Quantum Phase Slips. arXiv:2404.02989
- [4] I. V. Pechenezhskiy et al. The superconducting quasicharge qubit. Nature 585, 368 (2020). https://doi.org/10.1038/s41586-020-2687-9

Weak Link Superconducting Quantum Interference Devices for High-Resolution Scanning Magnetometry

CNF Project Number: 301722

Principal Investigator(s): Katja Nowack

User(s): Alex Striff

Affiliation(s): Laboratory of Atomic and Solid State Physics, Cornell University

Primary Source of Research Funding: AFOSR MURI FY21 Tunneling, Phenomena in Interface Superconductors

FA95502110429 (Subaward ID 134400-5118001) Contact: kcn34@cornell.edu, abs299@cornell.edu

Website: https://nowack.lassp.cornell.edu/
Primary CNF Tools Used: AIA Sputter 1. Bruker DektakXI

Primary CNF Tools Used: AJA Sputter 1, Bruker DektakXT Profilometer, Heidelberg MLA 150 Maskless Aligner, JEOL JBX-6300FS, E-beam Lithography System, Oxford 82 RIE, SC4500 Even-Hour Evaporator, SC4500 Odd-Hour Evaporator, Unaxis 770 Deep Silicon Etch, Zeiss Gemini SEM, Zeiss Supra SEM, Zeiss Ultra SEM,

Abstract:

Magnetic imaging is a powerful tool for studying quantum materials. To make a sensitive magnetometer for use in a scanning probe microscope, a small superconducting loop is interrupted by two Josephson junctions to create a superconducting quantum interference device (SQUID), which converts the magnetic flux coupled into the loop into a measurable signal [1]. This research explores one way to increase the spatial resolution and maximum operating field of a SQUID, which is to replace conventional superconductor-insulatorsuperconductor (SIS) Josephson junctions with narrow constrictions (weak links) in the superconducting loop, which allow the size of the loop to be less than 1 μ m [2]. Initial measurements have demonstrated the sensitivity of test SQUIDs to magnetic flux, with improvements in progress.

Summary of Research:

Figure 1(c) depicts a weak link SQUID, made of a patterned 50 nm niobium film on a silicon substrate with thermal oxide. For the weak links to behave like Josephson junctions, they must have dimensions comparable to the superconductor's coherence length [3], which necessitates the use of electron beam lithography to pattern a hard mask for the SQUID loop. A bilayer lift-off process patterns the SQUID loop in 20 nm of aluminum, and the pattern is then transferred to the niobium by dry etching in CF4 and O2. In order to raster the SQUID loop across the surface of a sample like in Figure 1(a), a Bosch process deep etch (Figure 1(b)) defines the corner of the scanning probe where the SQUID will be patterned. This approach has been successfully applied to scan conventional SQUIDs [4].

A key parameter for the performance of these SQUIDs

is the maximum current that can flow through the weak links while they remain superconducting, which is known as the SQUID's critical current. Cryogenic measurements of several SQUIDs revealed an up to 50 variations in the patterned widths and lengths of the weak links. Since the critical current is expected to be a function of only the resistance of the weak link [3], the variation is likely due to differences in the thickness of the niobium grain where the weak link happens to be patterned. Such niobium grain size differences are depicted in Figure 2(a).

When a weak link SQUID is operated in the readout scheme used for conventional SQUIDs, heating of the weak links occurs, and as such the thermal as well as electrical characteristics of the SQUID become important to the design. As such, we are changing the silicon dioxide film under the niobium to be a bare silicon film instead, in order to increase the thermal conductivity from the SQUID to the substrate. Doing so required the development of a new dry etch that would not undercut the silicon or niobium weak links, as seen in Figure 2(b). Another avenue to reduce the noise and electrothermal behavior of these SQUIDs is to add an onchip resistive shunt in parallel with the SQUID (Figure 3). As the shunt value must be comparable to the weak link resistance of a few Ohms, we optimized in-situ argon backsputtering in the AJA 1 sputtering system to completely remove the native niobium pentoxide layer before sputtering the platinum. Weakly cleaned shunts had insulating contacts at cryogenic temperatures, while partially cleaned shunts had a contact resistance of a few Ohms, and fully cleaned shunts could reach 100-200 $m\Omega$. The addition of a resistive shunt is also expected to eliminate destruction of the weak links by electrostatic discharge, as in Figure 4.

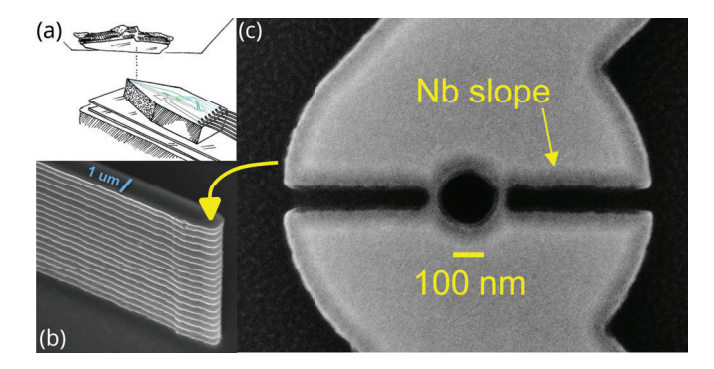


Figure 1: (a) A SQUID is a sensitive magnetometer that may be rastered over the surface of a sample. (b) By performing a deep silicon etch, a scanning probe at the etched tip may be brought within 1 µm of the sample. (c) Scanning electron microscope (SEM) image of a niobium (Nb) weak link SQUID. The narrow superconducting constrictions by the niobium slope make the device a sensitive tool for measuring the local magnetic flux through the loop.

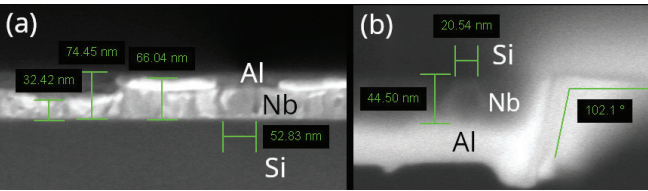


Figure 2: (a) SEM image of a cleaved niobium line, nominally 50 nm thick, with aluminum mask on top. Niobium grains as thin as 32 nm are visible. (b) Edge of an etched niobium line, with no undercutting of the niobium or silicon substrate, and little overetching into the silicon.

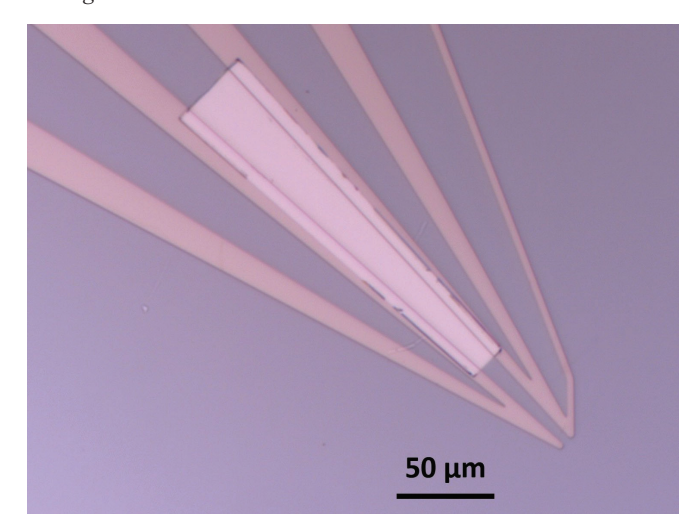


Figure 3: Bright-field microscope image of a platinum shunt center) on niobium traces. A SQUID would normally be patterned at the bottom right, but was omitted for testing the shunt. As the relevant contact occurs primarily through the covered niobium sidewall, the fencing along the perimeter of the platinum shunt has little impact on the shunt resistance.

We are continuing to optimize the design and fabrication of these weak link SQUIDs. Future work will investigate managing a heat budget during the deposition of the platinum shunt and of the mask for deep silicon etching, as these process steps partially degrade the superconductivity of the niobium. Empirical optimization of the SQUID and shunt design is also in progress.

- [1] Huber, M. E., et al. Review of Scientific Instruments 79, 053704 (2008).
- [2] Vasyukov, D., et al. Nature Nanotech 8, 639-644 (2013).
- [3] Likharev, K. K. Rev. Mod. Phys. 51, 101-159 (1979).
- [4] Pan, Y. P., et al. Supercond. Sci. Technol. 34, 115011 (2021).

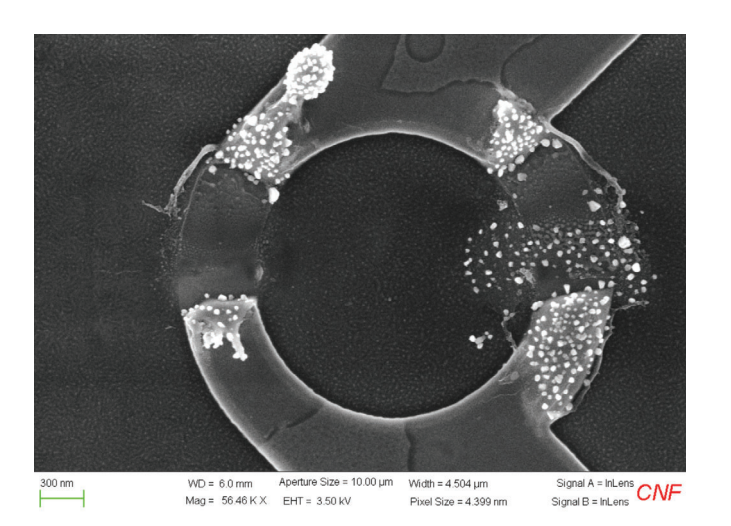


Figure 4: SEM image of a SQUID loop after a low-voltage electrostatic discharge event destroyed the weak links during electrical testing.

Resistivity scaling in Weyl semimetal NbAs nanowires and thin slabs

CNF Project Number: 303222 Principal Investigator(s): Judy Cha

User(s): Yeryun Cheon

Affiliation(s): Department of Physics, Cornell University

Primary Source of Research Funding: Semiconductor Research Corporation JUMP 2.0 SUPREME

Contact: jc476@cornell.edu, yc2458@cornell.edu

Website: https://cha.mse.cornell.edu/

Primary CNF Tools Used: Zeiss Supra SEM, Nabity NPGS Nanometer Pattern Generator System, Oxford 81 RIE,

SC4500 Odd-Hour Evaporator, Westbond 7400A Ultrasonic Wire Bonder

Abstract:

Topological semimetals possess topologically protected surface states that can enhance electrical conduction at reduced dimensions. Theory predicts certain topological semimetals, such as niobium arsenide (NbAs), can exhibit unusual resistivity scaling, i.e., decreasing resistivity with decreasing size, highlighting their potential as next-generation interconnects. However, experimental studies over a wide size range remain limited, particularly for 1D-confined nanostructures relevant to practical applications. In this work, we synthesize NbAs nanowires and thin slabs using thermomechanical nanomolding and focused ion beam (FIB) milling, respectively. Electrical measurements on nanomolded NbAs nanowires show that 40 nm-diameter wires exhibit a room-temperature resistivity of 10.5 \pm 2.4 $\mu\Omega$ ·cm, which is ~3 times lower than bulk. This is attributed to the suppressed surface electron scattering, corroborated by theoretical simulations showing a substantially longer carrier lifetime for surface states than for bulk states. In contrast, FIB-prepared NbAs thin slabs with larger cross-section areas and ion-beam induced damage show higher resistivity, suggesting the impact of surface damage on electrical transport.

Summary of Research:

Previous approaches for synthesizing NbAs nanostructures have employed bottom-up methods such as chemical vapor deposition or molecular beam epitaxy, as well as top-down methods like FIB milling. However, these approaches have been limited in either crystal quality or accessible sample sizes. Here, we use thermomechanical nanomolding to synthesize single-crystal NbAs nanowires with diameters down to 40 nm.

To test the electrical properties of NbAs nanowires, we fabricate four-terminal devices via standard e-beam lithography, using shared facilities in CNF. Notably, our NbAs nanowires exhibit decreasing resistivity with decreasing size, which is opposite to the trend observed in conventional metals such as Cu. Specifically, 40 nm diameter NbAs nanowires show a room-temperature resistivity of $10.5 \pm 2.4~\mu\Omega\cdot\text{cm}$, which is ~3 times lower than single-crystal bulk. Based on theoretical calculations, we attribute this resistivity reduction to a significantly longer carrier lifetime in surface states compared to bulk states.

Since the nanomolding process relies on interfacial diffusion, it becomes increasingly challenging to produce samples with large cross-section areas. To complement the nanowire study, we fabricate NbAs thin slabs using FIB milling and study their transport properties across different geometries and surface facets. Despite performing the final milling at a low accelerating voltage of 2 kV, Ga⁺-induced damage leads to the formation of an Nb-rich surface shell, which causes a superconducting transition at ~2 K. In contrast to the nanomolded nanowires, these FIB-prepared slabs show higher resistivity than bulk, suggesting the absence of the surface-dominant transport observed in nanowires, possibly due to surface damage.

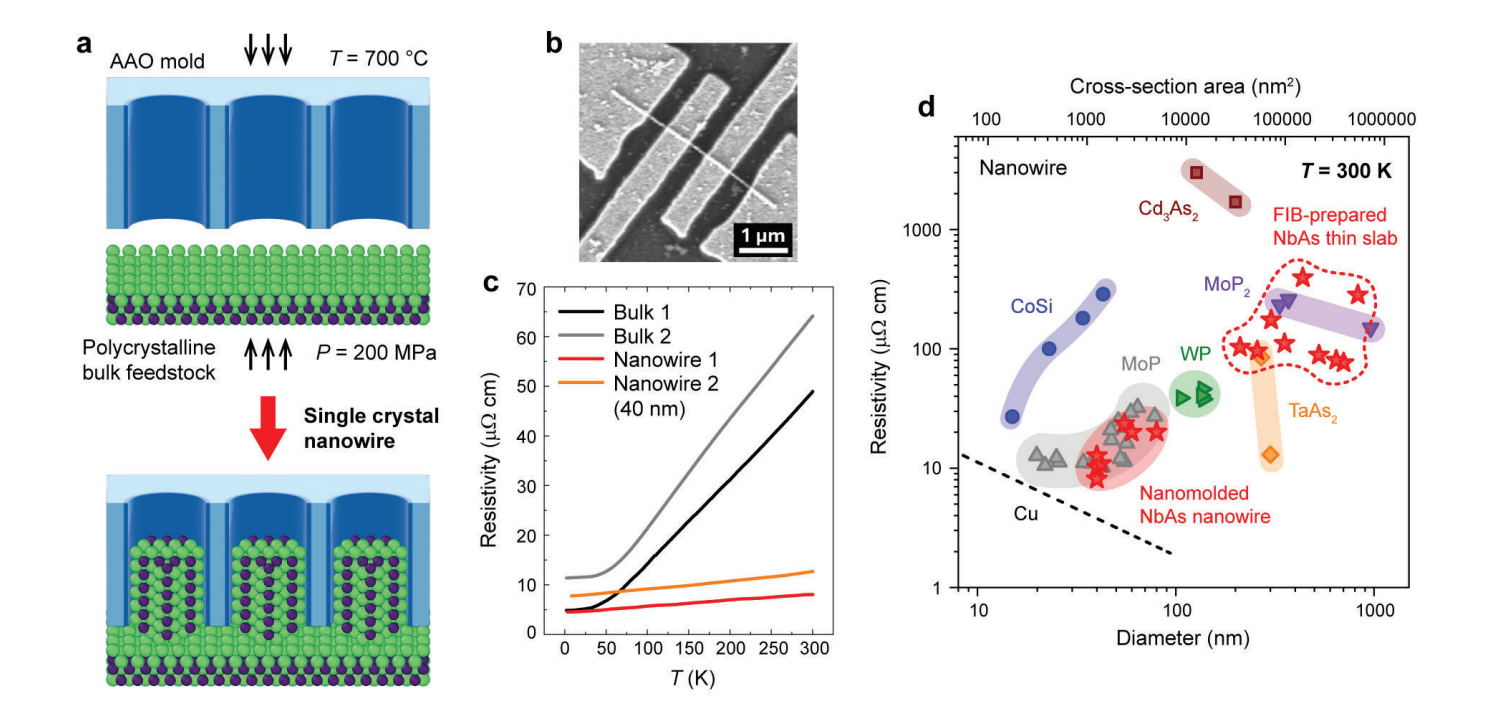


Figure 1. (a) Schematic of the thermomechanical nanomolding process. (b) Representative SEM image of a four-terminal NbAs nanowire device. (c) Temperature-dependent electrical resistivity of bulk single crystals and nanowires. (d) Room-temperature resistivity as a function of diameter (cross-section area) for NbAs nanowires, NbAs thin slabs, and various other topological semimetal nanowires.

Our results demonstrate surface-dominant transport in NbAs nanowires, highlighting the significant role of topologically protected surface states at reduced dimensions. We will continue measuring nanowire and thin slab devices of varied sizes, with particular focus on further reducing nanowire diameters to enhance surface-state contributions. In addition, we plan to systematically investigate how the surface orientations of NbAs thin slabs influence transport behavior.

References:

[1] Cheon, Y. et al. Surface-dominant transport in Weyl semimetal NbAs nanowires for next-generation interconnects. arXiv:2503.04621 (2025).

Resistivity Scaling of CuAl2-x Nanowires for Post-Cu Interconnects

CNF Project Number: 303222

Principal Investigator(s): Jeeyoung Judy Cha

User(s): Quynh Sam

Affiliation(s): Department of Materials Science and Engineering, Cornell University

Primary Source of Research Funding: Semiconductor Research Corporation SUPREME JUMP2.0 Center

Contact: judy.cha@cornell.edu, qps2@cornell.edu

Website: https://cha.mse.cornell.edu/

Primary CNF Tools Used: Nabity, Zeiss Supra SEM, AJA Sputter 1 and 2, Odd-hour evaporator

Abstract:

The dimensions of copper interconnects in current microelectronic integrated circuits have decreased below copper's electron mean free path (40 nm), leading to high resistivity and thus detrimental increases in power dissipation and signal delays. To continue the downscaling of electronics while maintaining performance, a material with better resistivity is needed to replace copper in interconnects. CuAl2 is a promising candidate due to its low bulk resistivity $(6.5 \mu\Omega \cdot cm)$,1 small mean free path (14 nm),1 and high electromigration resistance compared to copper.2 CuAl2 has demonstrated promising resistivity scaling in thin films,3 however, the scaling behavior of nanowires has not been studied. We report the resistivity of coreshell CuAl2-x nanowires with diameters ranging from 30 nm to 70 nm. The CuAl2-x nanowires are fabricated using thermomechanical nanomolding and possess a 5 - 10 nm thick CuAl shell with a CuAl2 core. At diameters below 45 nm, the resistivities range between 20 - 35 μΩ·cm while larger diameter nanowires show slightly higher resistivities. This scaling behavior along with improved electromigration resistance suggest that CuAl2 may be a promising post copper interconnect candidate.

Summary of Research:

We fabricated four-point probe devices on SiO2/Si substrates using the molded CuAl2-x nanowires as shown by the schematic in Figure 1a. Figure 1b shows a high angle annular dark field scanning transmission electron microscopy (HAADF-STEM) image of a nanowire device cross-section. There is a distinct contrast between the nanowire perimeter and core, revealing that the nanowires have a core-shell structure. STEM electron energy loss spectroscopy (EELS) composition mapping shown in Figure 1c shows that the core is CuAl2 while the shell is CuAl. Resistivity

measurements are carried out in a cryogenic probe station at 10-6 mbar after annealing the devices at 400 K for 1 hour. A 4-point I-V curve is shown in Figure 2a, and size-dependent resistivity data for 10 nanowire devices is summarized in Figure 2b. The majority of the resistivity values of the CuAl2-x nanowires are much higher than that of bulk CuAl2 and effective Cu. Possible causes of the increased resistivity include surface roughness and compositional variations in the nanowires.

Conclusions and Future Steps:

We present the size-dependent resistivity scaling of core-shell CuAl2-x nanowires fabricated using thermomechanical nanomolding. The resistivity values are higher than that of bulk CuAl2 as well as effective Cu at comparable dimensions, possibly due to surface roughness as well as compositional variation throughout the nanowires that can increase scattering. Without these defects, it is possible that the resistivity and line resistance of stoichiometric CuAl2 nanowires could become competitive against effective Cu at nanoscale dimensions.

- [1] J. Appl. Phys. 136, 171101 (2024)
- [2] J. Alloys and Compounds, 918, 165615 (2022).
- [3] J. Vac. Sci. Technol. B 37, 031215 (2019).

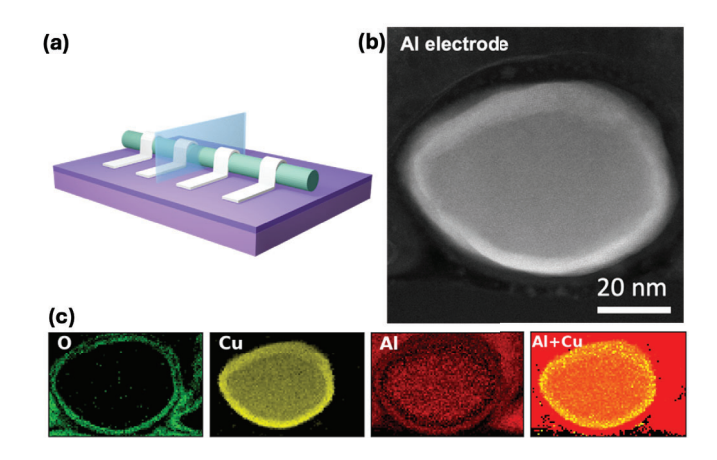


Figure 1. Cross-section analysis of core-shell CuAl2-x nanowire device. (a) Schematic showing CuAl2-x nanowire (teal) on SiO2/Si substrate (purple) with Al contacts (white). The blue plane denotes the cross-section plane of the STEM analysis. (b) HAADF-STEM image of the crosssection of CuAl2-x nanowire device. (c) STEM-EELS maps of cross-section showing O, Cu, Al, and Al and Cu elemental fractions.

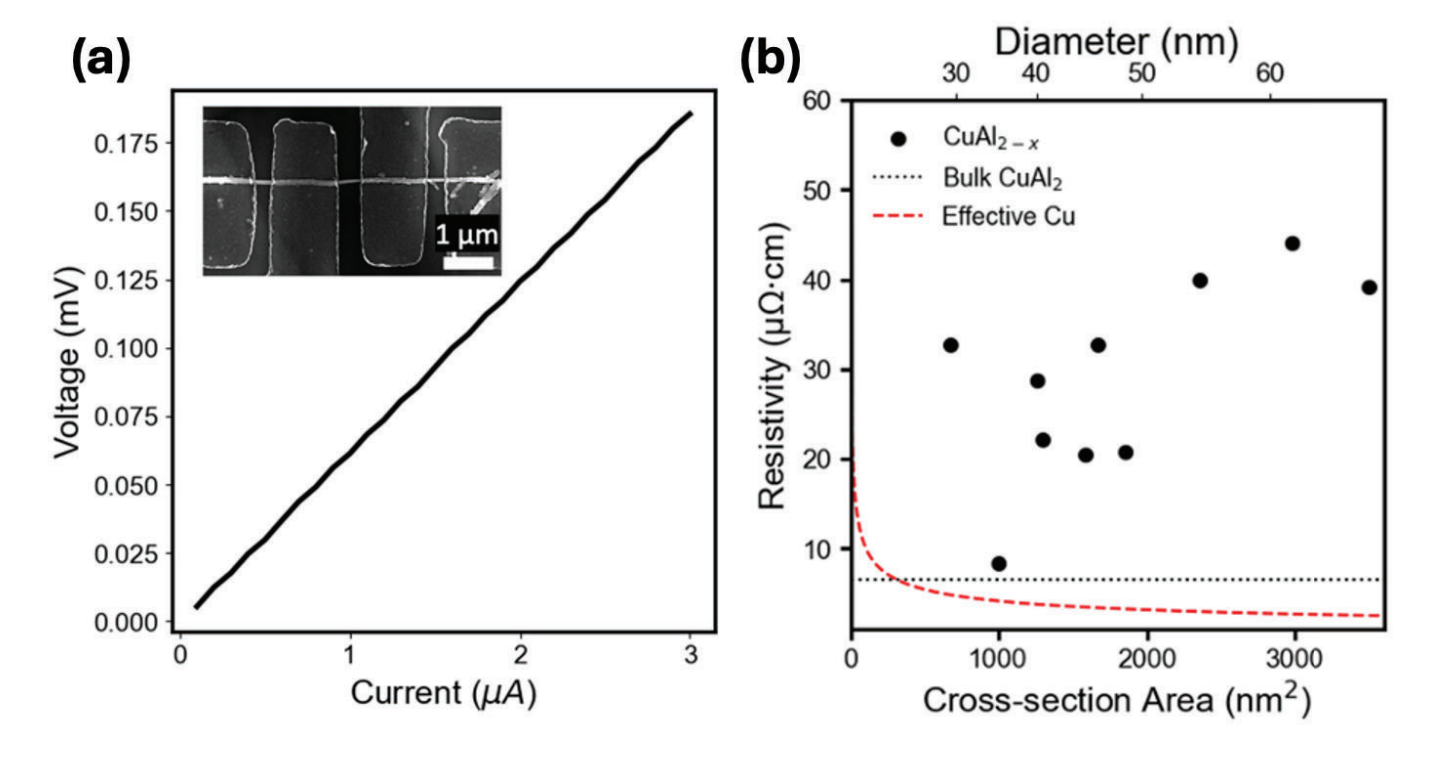


Figure 2. Transport data for CuAl2-x nanowire devices. (a) Four-point I-V curve of a CuAl2-x nanowire device. The inset shows an SEM image of the device. (b) Resistivity vs. size for ten CuAl2-x nanowire devices compared with bulk CuAl2 and effective Cu. The total core-shell cross-section area is used to calculate resistivity values.

Characterization of Fluxonium Qubits

CNF Project Number: 306723

Principal Investigator(s): Ivan Pechenezhskiy User(s): Benjamin Byrd, Kesavan Manivannan

Affiliation(s): Syracuse University

Primary Source of Research Funding: Army Research Office Contact: ivpechen@syr.edu, babyrd@syr.edu, kmanivan@syr.edu

Primary CNF Tools Used: ASML DUV Stepper, JEOL 6300, PT770 Plasma Etcher, Heidelberg

DWL2000 Mask Writer

Abstract:

Quasiparticles are a significant intrinsic decoherence channel in superconducting qubits. Although their characterization and mitigation have been extensively studied in transmon qubits, their impact on fluxonia remains comparatively unexplored. To investigate this, we generate excess quasiparticles in fluxonia by injecting pair-breaking phonons and photons via on-chip injectors. In this controlled injection, we observe the qubit population dynamics that warrant separate extraction of qubit excitation and relaxation rates.

Summary of Research:

Superconducting quantum systems are among the leading platforms for implementing quantum computing. Josephson tunnel junctions provide the necessary nonlinearity for the spectral isolation of qubit computational states. The fluxonium qubit specifically comprises a small Josephson junction shunted by a capacitor and a large inductance realized with an array of Josephson junctions. This qubit design exhibits long coherence times and large anharmonicity [1, 2].

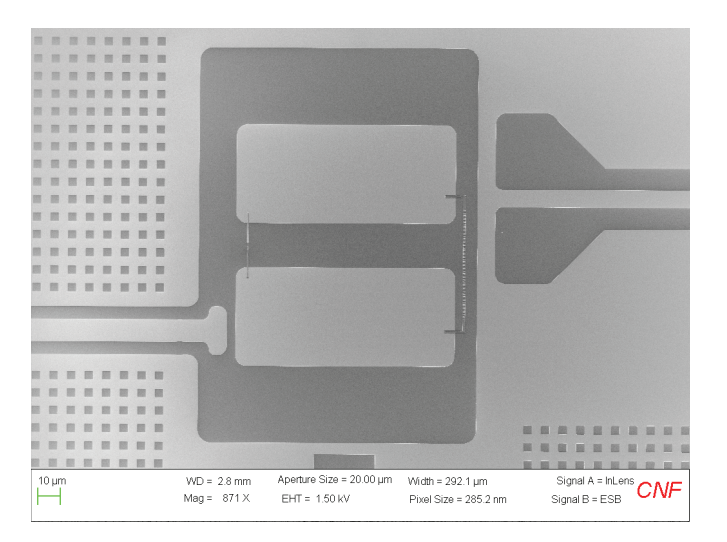
Figure 1a shows an SEM image of our recent design of a fluxonium qubit fabricated at the CNF. The two niobium capacitor pads (40 $\mu m \times 100~\mu m$ each) define the capacitive energy scale $E_{c}/h \sim 1.1~GHz$. The Al/AlOx/Al small Josephson junction (~100nm \times 100 nm) between the pads sets the Josephson energy EJ/h $\sim 2.1~GHz$. The inductor formed by an array of $\sim 200~Josephson$ junctions (~ 0.5 $\mu m \times 1~\mu m$ each) is associated with the inductive energy EL/h $\sim 90~MHz$.

Photolithography and electron-beam lithography were performed at the CNF, and electron-beam evaporation and sputtering were carried out at Syracuse University. The flux bias line can be seen on the right in Fig. 1a. Each qubit is capacitively coupled to a resonator for dispersive readout of the qubit state. Figure 1b displays the design of the injector Josephson junction, which is

voltage biased to produce pair-breaking phonons and photons that subsequently produce quasiparticles at the qubit junctions [3].

The qubits are measured in a dilution refrigerator at 10 mK. Under certain injection biases, we observed an apparent increase in energy relaxation time T1 extracted from standard free decay measurements, as shown in Fig. 2a. This is because the excitation rate becomes comparable to or even exceeds the relaxation rate, causing the excited-state population to decay toward a steady state above the background. Fitting such dynamics to a simple exponential that neglects this offset can yield an apparent increase in the extracted T1, necessitating a direct extraction of the individual transition rates. In Fig. 2b, we show background and post-injection population dynamics after the qubit initialization to states |0> and 11>. We use this protocol to investigate the increase in transition rates caused by quasiparticle poisoning, including the effects arising from the efficient coupling of pair-breaking photons from the injector to the qubit, mediated by spurious antenna modes of the injector and qubit geometries [4].

- A. Somoroff et al. Millisecond Coherence in a Superconducting Qubit. Phys. Rev. Lett. 130, 267001 (2023). https://doi.org/10.1103/PhysRevLett.130.267001
- [2] L. Nguyen et al. High-Coherence Fluxonium Qubit. Phys. Rev. X 9, 041041 (2019). https://doi.org/10.1103/ PhysRevX.9.041041
- [3] V. Iaia et al. Phonon downconversion to suppress correlated errors in superconducting qubits. Nature Communications, 13, 6425 (2022). https://doi.org/10.1038/s41467-023-35986-3
- [4] C. Liu et al. Quasiparticle Poisoning of Superconducting Qubits from Resonant Absorption of Pair-Breaking Photons. Phys. Rev. Lett. 132, 1 (2024). https://link.aps.org/doi/10.1103/PhysRevLett.132.017001



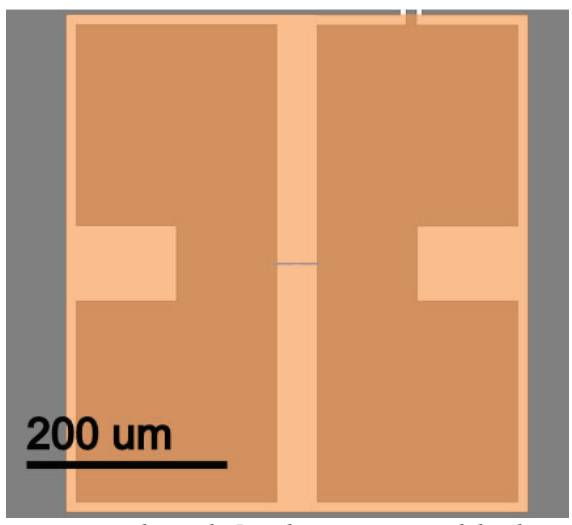


Figure 1: (a) Scanning electron micrograph of the fluxonium qubit showing the capacitor pads, single Josephson junction, and the chain of Josephson junctions. (b) Design of the Josephson junction injector.

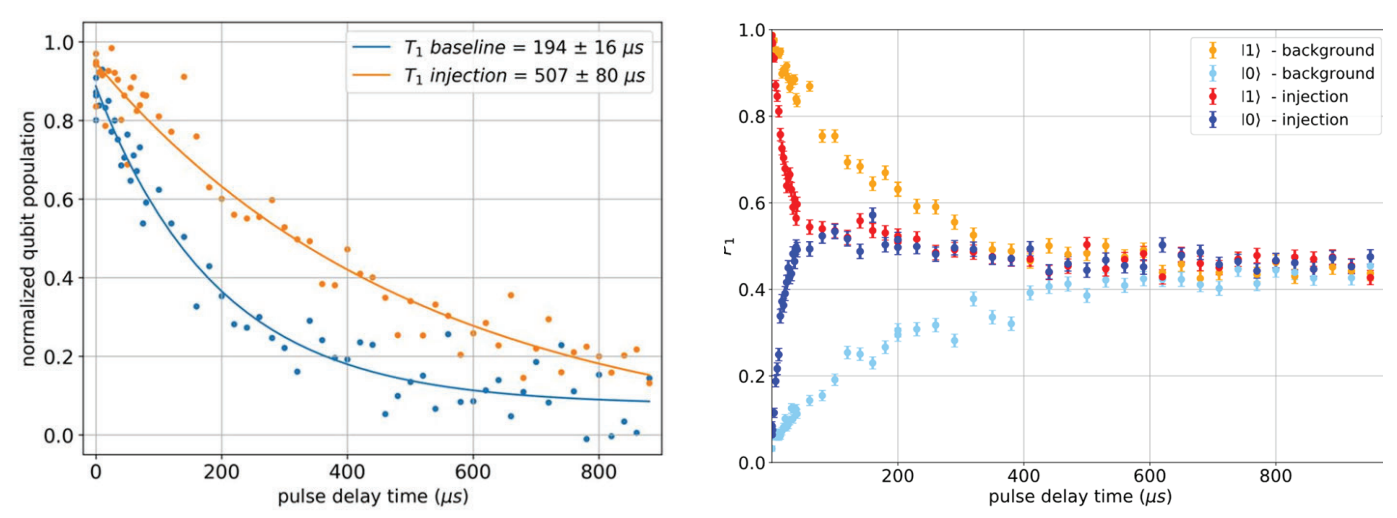


Figure 2: Two different measurement protocols for the baseline and injection cases. (a) Conventional free decay T1 measurement. (b) Qubit populations measured after initialization in the $|0\rangle$ and $|1\rangle$ states.

Epitaxial Nitride Josephson Junctions

CNF Project Number: 311723

Principal Investigator(s): Valla Fatemi

User(s): Benjamin Byrd, Kushagra Aggarwal

Affiliation(s): School of Applied and Engineering Physics, Cornell University

Primary Source of Research Funding: AFOSR Contact: vf82@cornell.edu, ka543@cornell.edu Website: https://fatemilab.aep.cornell.edu

Primary CNF Tools Used: Heidelberg MLA 150 Maskless Aligner, PT 770, ICP Etcher, JEOL-9500FS E-beam

Lithography System, Zeiss Ultra SEM, SC4500 Even-hour Evaporator, AJA Sputter 1.

Abstract:

Superconducting quantum technologies have traditionally relied on aluminum-based devices because of the ease of fabrication and the self-limiting growth of aluminum oxide. However, aluminum has a relatively low critical temperature (1.2K) requiring helium-3 refrigeration, and it suffers from surface oxides and dielectric loss. In this work, we focus on fabricating Josephson junctions from nitride-based materials grown by molecular beam epitaxy (MBE). These crystalline materials are more resistant to surface oxidation and have the potential to reduce material-related losses in superconducting qubits, thereby enabling significantly improved coherence times.

Summary of Research:

A trilayer stack comprising NbN (7 nm) – AlGaN (3 nm) – NbN (7 nm) is grown using MBE. The Josephson junction is fabricated using a bottom-up approach, as shown in Figure 1. In a first step, the stack is etched to define the bottom layer. Then, a central region is defined as the junction and the top two layers are etched everywhere else, defining the bottom electrode. The top electrode is connected using an Nb wiring layer. Since there is a possibility of the top wiring layer getting connected to the bottom NbN, a spacer layer made of SiO2 acts as an electrical isolation between the top Nb and bottom NbN.

Conclusions and Future Steps:

In this work, we have completed the lithography steps of the junction with proper alignment and isolation achieved between the layers. In the next steps, we will work on removing the SiO2 to eliminate any source of dielectric losses and improving the quality of the MBE grown films.

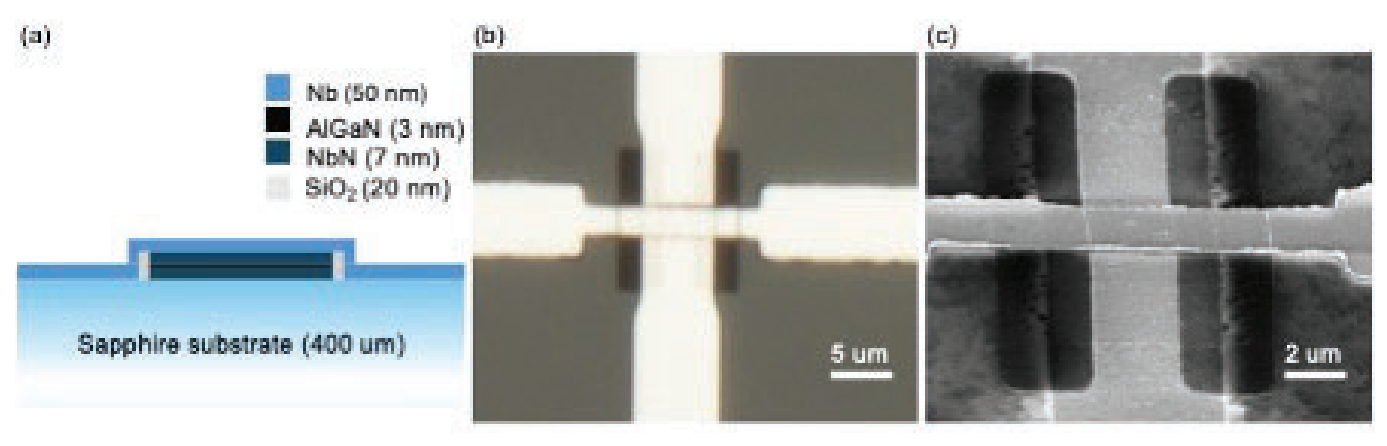


Fig. 1: Epitaxial nitride Josephson junction: (a) NbN (7 nm) -AlGaN (3 nm) -NbN (7 nm) stack grown using MBE on a sapphire substrate. (b) An optical image of the patterned junction. (c) A scanning electron microscope image showing the junction, where a top Nb wiring layer is connected and SiO2 isolates the Nb wiring layer from the bottom.

Fabrication of 2D Graphene Devices for Low Temperature Transport Measurement

CNF Project Number: 312523

Principal Investigator(s): Kenji Yasuda

User(s): Benjamin Byrd, Lujin Min, Zhen Yang

Affiliation(s): School of Applied and Engineering Physics, Department of Physics, Cornell University

Primary Source of Research Funding: Lab Start-up Fund

Contact: kenji.yasuda@cornell.edu, db923@cornell.edu, lm936@cornell.edu, zy467@cornell.edu

Website: sites.google.com/view/kenjiyasuda

Primary CNF Tools Used: Heidelberg MLA 150, Zeiss Supra SEM, Nabity Nanometer Pattern Generator System (NPGS), SC4500 Odd/Even-Hour Evaporator, Oxford PlasmaLab 80+ RIE System (Oxford 81)Lithography System,

Zeiss Ultra SEM, SC4500 Even-hour Evaporator, AJA Sputter 1.

Abstract:

It can be said that many of the most exotic correlated many body states can be found in the phase diagram of magic angle twisted bilayer graphene (MATBG), including unconventional superconductivity [1] and the quantum anomalous hall effect (QAHE) [2]. In order to study the now broad range of emerging 2D materials, these devices must undergo a careful sample preparation and fabrication procedure. We report the successful fabrication and measurement of a variety of graphene based devices, including some twisted bilayer graphene (TBG).

Summary of Research:

By measuring the longitudinal and hall resistance of a material we can probe the most important aspects of its electronic properties. In a dual-gated hall bar device architecture, with the instruments available in our lab, it is possible to measure these two resistances versus a versatile 4D phase space of carrier density, electric displacement field, out of plane magnetic field, and temperature. We can search for and define interesting phenomena within this phase space, as well as characterize their properties. In this report we present data from two different TBG devices.

Before fabrication can be done, our samples must be stacked into the correct device architecture. A schematic of this device structure can be seen in Figure 1a. In short, we have a top and bottom graphite gate along with two pieces of hBN to act as the dielectric, with a middle device layer. An image of a TBG device in the middle of the stacking procedure can be seen in Fig 1b. Additionally, we can characterize the moiré pattern

formed by the twisted bilayer graphene using an atomic force microscopy technique (AFM), torsional force microscopy (TFM), during this step as shown in Fig 1c.

Once the stacking procedure is complete we fabricate the resulting device into a hall bar shape and make electrical contacts. Figure 2a shows the device coated in Polymethyl methacrylate (PMMA), patterned into a hall bar shape with electron beam lithography (EBL). Figure 2b shows the final result after etching the device into a hall bar, followed by another round of EBL as well as metal deposition. Finally, the device can be installed onto our sample holder, wirebonded, and installed onto our low temperature probe for transport measurements, as seen in Fig 2c.

Figure 3 shows the longitudinal resistance measurement for two different devices at a temperature of 1.5K. Fig 3a shows the landau fan diagram of the TBG sample which is detailed in Fig 1 and 2. The full filling peak is very well developed and some landau fan features can be observed, including some coming from the full filling. However, the integer peaks are blurred, likely due to being far from the magic angle and the device angle not being homogeneous. Fig 3b shows the landau fan for another TBG device. This one seems to have many different peaks and landau levels. It is not clear whether these peaks correspond to the integer peaks, full filling from twist angle inhomogeneity, or hBN alignment in the device. None-the-less, low noise transport data resolving clearly the features of both devices are able to be taken

We have been able to implement a complete fabrication procedure in order to perform low temperature transport measurements on our devices. With these fabrication and measurement methods well established we are planning to expand our sample fabrication to a variety of materials and device structures in the search for interesting correlated and symmetry breaking phenomena.

- [1] Y. Cao, V. Fatemi, S. Fang, K. Watanabe, T. Taniguchi, E. Kaxiras, and P. Jarillo-Herrero, Unconventional superconductivity in magic-angle graphene superlattices, Nature 556, 43 (2018).
- [2] M. Serlin, C. L. Tschirhart, H. Polshyn, Y. Zhang, J. Zhu, K. Watanabe, T. Taniguchi, L. Balents, and A. F. Young, Intrinsic quantized anomalous Hall effect in a moiré heterostructure, Science 367, 900 (2020).

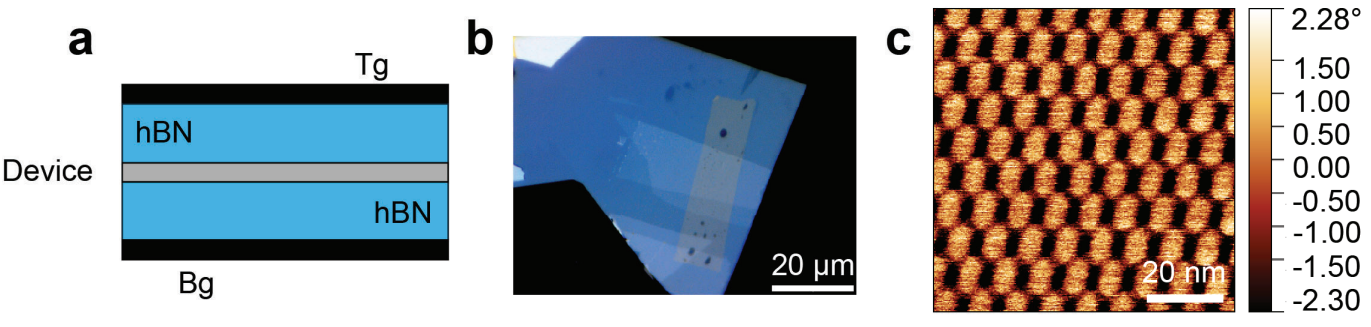


Figure 1: a. Device structure, including two graphite gates, hBN as the dielectric, and the device layer. b. Optical images of a partially stacked device. Scale bar - 20 µm. c. TFM-phase image of the moiré pattern formed by the twisted graphene layers. Scale bar - 20 nm.

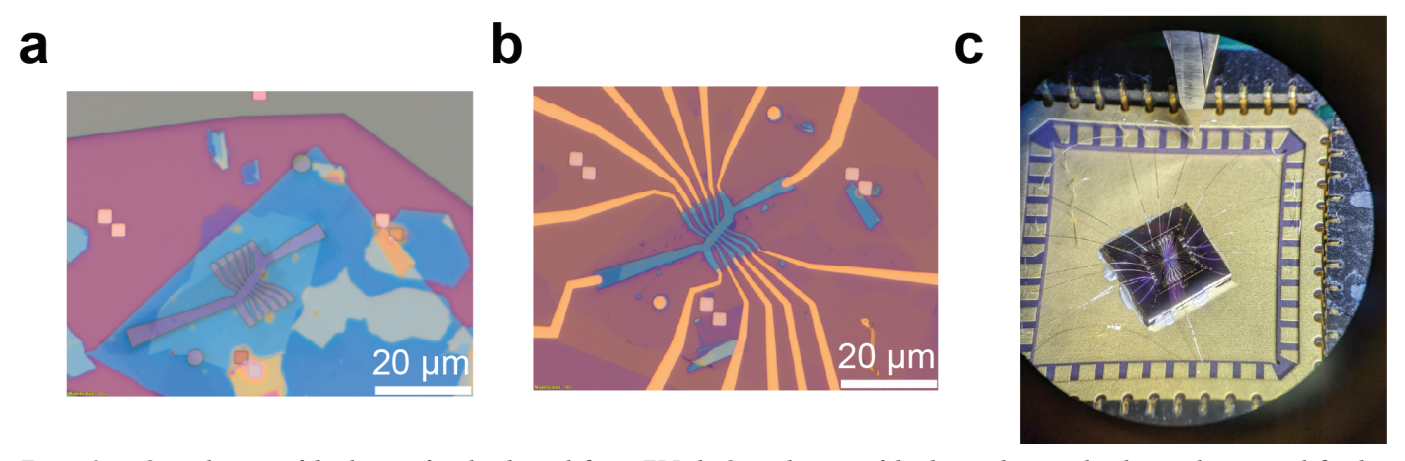


Figure 2: a. Optical image of the device after the shape defining EBL. b. Optical image of the device showing the electrical contacts defined using EBL. c. Image of the sample installed onto our sample holder with the pads being wirebonded for electrical contact.

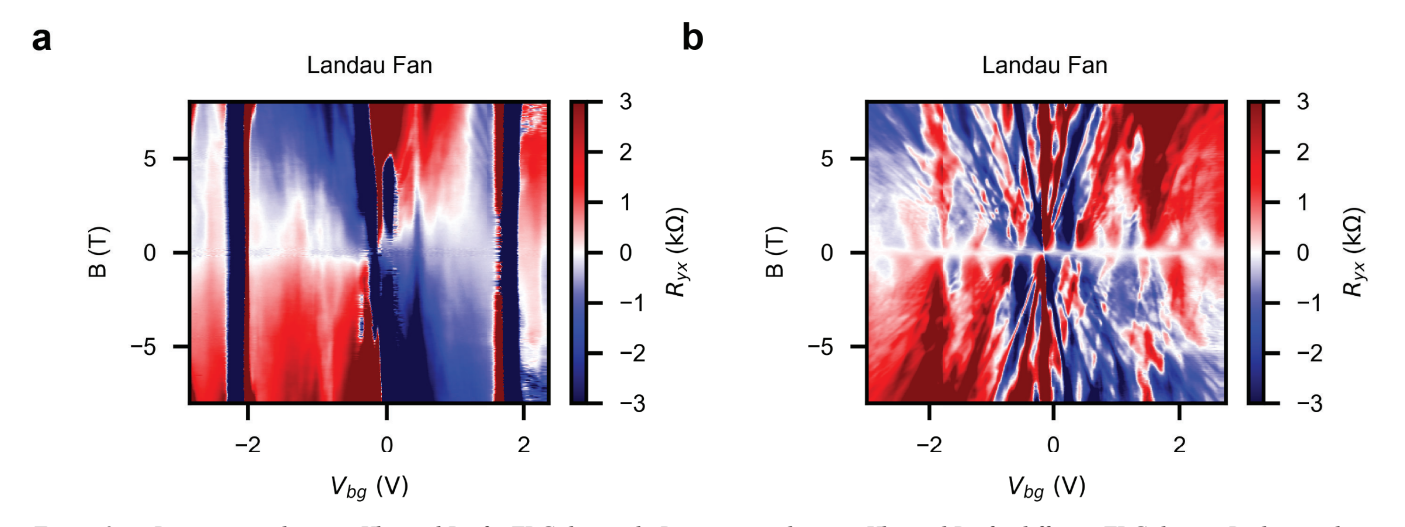


Figure 3: a. Ryx measured versus Vbg and B of a TBG device. b. Ryx measured versus Vbg and B of a different TBG device. Both are taken at 1.5K.

Electrical Transport in Graphene Heterostructures

CNF Project Number: 316224

Principal Investigator(s): Xiaomeng Liu

User(s): Jinghao Deng, Jiabin Xie, Chang Chang, Alexander Sanchez

Affiliation(s): Laboratory of Atomic And Solid State Physics, Department of Physics, Cornell University

Primary Source of Research Funding: National Science Foundation, College of Arts and Sciences

Contact: xiaomengliu@cornell.edu

Website: https://www.xiaomengliu.com/

Primary CNF Tools Used: Heidelberg DWL 2000, Photolithography Spinners, GCA AutoStep 200 DSW i-line Wafer Stepper, E-Beam Lithography Spinners, Zeiss Supra SEM, Nabity Nanometer Pattern Generator System, Oxford

81/82 Etcher, SC4500 Even/Odd, Oxford ALD Flexal

Abstract:

Graphene heterostructures continue to provide myriad opportunities for researching new strongly correlated and topological physics. We fabricate three different types of graphene heterostructure, to facilitate study of this physics. We will examine magic-angle twisted bilayer graphene in close proximity to few-layer graphene, an electronic double-layer of bilayer graphene separated by thin boron nitride, and rhombohedral stacked graphene. Each of these configurations is host to unique phenomena to be surveyed using low temperature electrical transport measurements. Imperative to our ability to process these graphene heterostructures into electronic devices which can be measured in a dilution refrigerator are a variety of tools available to us through the Cornell nano-scale science and technology facility.

Summary of Research:

We are conducting low temperature electrical transport measurements on three different categories of graphene heterostructures, magic-angle twisted bilayer graphene, insulated graphene bilayers, and rhombohedral-stacked graphene.

The pairing mechanism of superconductivity in magicangle twisted bilayer graphene remains unclear, whether it be a conventional phonon-mediated pairing or a more exotic unconventional pairing. Previous work has used bilayer graphene in close proximity to but insulated from magic angle twisted bilayer graphene to tune the strength of the Coulomb interaction, thereby tuning the superconducting phase[3]. We will use multilayer graphene to further investigate the effect of Coulomb screening on magic angle twisted bilayer graphene. Figure 1 shows a graphene heterostructure device, intended to be used for this purpose.

Using bi-layer graphene separated by a thin piece of boron nitride, an exciton condensate phase has previously been demonstrated[2]. We have fabricated bi-layer graphene heterostructure devices to analyze this. Figure 2 shows a graphene heterostructure device for studying exciton condensation in a graphene bi-layer heterostructure. To prevent the formation of PN junctions between differently doped graphene bi-layers, we used the Oxford ALD Flexal to deposit an AL2O3 thin film on top of the graphene heterostructure, and then evaporated additional metal electrodes, to dope the graphene contacts.

Rhombohedral-stacked graphene's unique electronic properties promote the role of electron-electron interactions, giving rise to topological and strongly correlated quantum phases [4, 1]. These phases are not yet fully understood, but could have a variety of applications in future electronics. We have fabricated few-layer Rhombohedral-stacked graphene heterostructures and performed low temperature electronic transport measurements on them. A rhombohedral-stacked graphene heterostructure device is shown in Figure 3.

Crucial to our work studying graphene heterostructures has been the Cornell nano-scale science and technology facility. All of our graphene heterostructure devices use a similar nano fabrication procedure, which is carried out entirely within the Cornell nano-scale science and technology facility's clean room. First, a completed graphene/boron nitride heterostructure is deposited onto a silicon substrate outside the clean room, using transfer techniques standard to van der Waals heterostructure assembly[5]. Alignment markers are evaporated onto this substrate in the clean room before deposition, they are patterned using a quartz photomask prepared with the Heidelberg DWL200, and then exposed using the

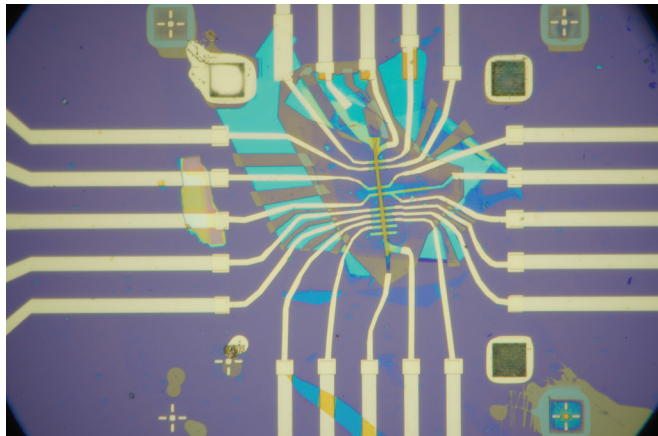


Figure 1: A graphene heterostructure device consisting of magicangle twisted bilayer graphene in close proximity to few-layer graphene. The heterostructure has been etched into a Hall bar geometry using clean room tools.

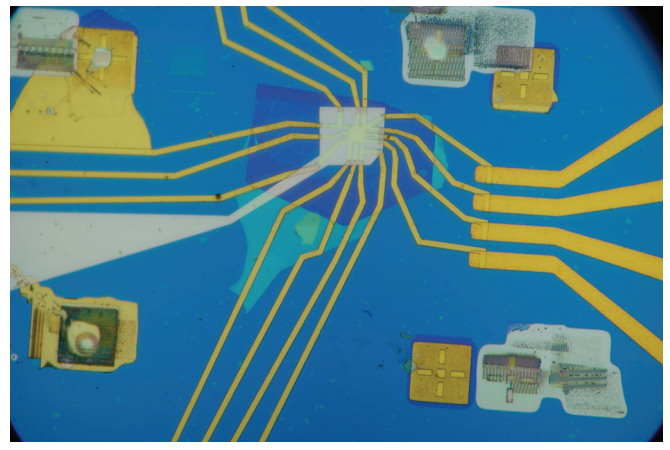
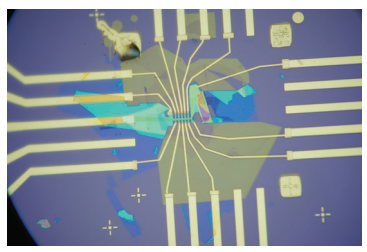


Figure 2: An electronic double layer device made with bilayer graphene separated by thin boron nitride. Al2O3 has been deposited on top of it, and gold has been evaporated to dope the graphene contacts.



A rhombohedral-stacked multilayer graphene heterostructure which has been etched into a Hall bar geometry using nanofabrication facilities.

GCA AutoStep 200 DSW i-line wafer stepper. Using the E-Beam lithography spinners, PMMA A4-950 is spun onto the sample, and then the graphene/boron nitride heterostructure is patterned into an appropriate electrical geometry using successive electron beam lithography steps with the Zeiss Supra SEM and Nabity Nanometer Pattern Generator system and etching steps with the Oxford 81/82 Etchers, wherein O2 and CHF3 plasmas are used to etch. When the graphene/BN heterostructure has been patterned appropriately, the SC4500 Even/Odd-Hour evaporators are used to deposit chromium,

palladium, onto the silicon substrate and create metal electrodes. To aid with lift-off after metal evaporation, layers of PMMA A4-495 and A4-950 are used, or M2-950.

Conclusions and Future Steps:

Our work studying magic-angle twisted bilayer graphene in close proximity to few-layer graphene, an electronic double-layer of bilayer graphene separated by thin boron nitride, and rhombohedral stacked graphene probes topological and strongly correlated physics. We have carried out measurements of completed rhombohedral stacked graphene heterostructure devices, but have not yet done so on the other two configurations of graphene device we have fabricated. Future work will include electrical measurements of these configurations, and further assemblage of graphene devices to improve measurement quality and certainty. The Cornell nanoscale science and technology facility provides access to tools essential to our continued research.

- [1] Tonghang Han, Zhengguang Lu, Zach Hadjri, Lihan Shi, Zhenghan Wu, Wei Xu, Yuxuan Yao, Armel A. Cotten, Omid Sharifi Sedeh, Henok Weldeyesus, Jixiang Yang, Junseok Seo, Shenyong Ye, Muyang Zhou, Haoyang Liu, Gang Shi, Zhenqi Hua, Kenji Watanabe, Takashi Taniguchi, Peng Xiong, Dominik M. Zumbühl, Liang Fu, and Long Ju. Signatures of chiral superconductivity in rhombohedral graphene. Nature, 643(8072):654–661, Jul 2025.
- [2] Xiaomeng Liu, Kenji Watanabe, Takashi Taniguchi, Bertrand I. Halperin, and Philip Kim. Quantum hall drag of exciton condensate in graphene. Nature Physics, 13(8):746–750, Aug 2017.
- [3] Xiaoxue Liu, Zhi Wang, K. Watanabe, T. Taniguchi, Oskar Vafek, and J. I. A. Li. Tuning electron correlation in magicangle twisted bilayer graphene using coulomb screening. Science, 371(6535):1261–1265, 2021.
- [4] Zhengguang Lu, Tonghang Han, Yuxuan Yao, Aidan P. Reddy, Jixiang Yang, Junseok Seo, Kenji Watanabe, Takashi Taniguchi, Liang Fu, and Long Ju. Fractional quantum anomalous hall effect in multilayer graphene. Nature, 626(8000):759–764, Feb 2024.
- [5] L. Wang, I. Meric, P. Y. Huang, Q. Gao, Y. Gao, H. Tran, T. Taniguchi, K. Watanabe, L. M. Campos, D. A. Muller, J. Guo, P. Kim, J. Hone, K. L. Shepard, and C. R. Dean. Onedimensional electrical contact to a two-dimensional material. Science, 342(6158):614–617, 2013.

Reliable Scanning Tunneling Microscopy Prepared Fabrication for 2D Quantum Material Device Research

CNF Project Number: 319924

Principal Investigator(s): Xiaomeng Liu User(s): Yiming Sun, Jinghao Deng

Affiliation(s): Laboratory of Atomic And Solid State Physics, Department of Physics, Cornell University

Primary Source of Research Funding: The College of Arts & Sciences, Cornell University, National Science Foundation

Contact: xl956@cornell.edu

Website: https://www.xiaomengliu.com/

Primary CNF Tools Used: Heidelberg DWL 2000 Mask Writer, GCA AS200 i-line Stepper, Oxford Plasmalab 81/82

RIE, SC4500 Odd-Hour Evaporator, DISCO Dicing Saw

Abstract:

This report introduces a novel fabrication methodology enabling the reliable production of scanning tunneling microscopy (STM) prepatterned chips for micro-level 2D material flake identification. By integrating precision photomask design, optimized interfacial metal stacks, and defect-minimized processing, we achieved >95% yield in devices capable of targeting sub-5µm flakes. The process establishes a new baseline for reproducible quantum material research platforms.

Summary of Research:

STM achieves atomic resolution but suffers from an intrinsically small field of view (~1 μm), rendering navigation to specific micron-scale samples (e.g., 2D flakes) slow and prone to tip crashes. External localization aids are impractical in extreme environments [1, 2]. In CNF, we developed recipes for prepatterned chips with integrated registration markers to resolve this by enabling reliable STM navigation to target flakes without external systems.

1. Precision Photomask Engineering

Critical to pattern making was developing quartz 5-inch photomasks with alignment markers resolvable at 199 nm scales. Using the Heidelberg DWL 2000, AutoCAD-designed patterns underwent .dxf to .gds conversion in KLayout with manual correction of alphanumeric fiducials (design pattern see Fig. 1). This eliminated coordinate dri $\bar{\rm O}$ during stepper alignment, enabling consistent placement of μm level registration markers essential for 2D quantum device targeting. Post-write verification included Hamatech Process 2 cleaning and 60s Cr etching (Process 1) to ensure defect-free surfaces.

2. Lithography for Flake-Scale Features

A bilayer resist system (LOR3A/SPR700) was optimized for STM-specific undercut profiles, comprising an adhesion layer of P20 at 3000 rpm (15s), undercut control via LOR3A (4000 rpm, 180°C/5min bake), and an imaging layer of SPR700 (3000 rpm, 90°C/1min bake). GCA iline exposure at focus = -6, dose = 0.22 produced 800 nm apertures with tapered sidewalls (70° angle), verified by cross-section SEM. Post-development O₂ descum (Oxford RIE, 60W, 25s) prevented resist scumming around critical edges.

3. Interfacial Engineering for Flake Contact

Two metallization strategies enabled reliable flake-electrode interfaces: edge contacts with 3.5nm Cr / 15nm Pd evaporated at 0.5Å/s (1×10⁻⁶ Torr), and scanning pads with 50nm Cr at 4Å/s (4×10⁻⁶ Torr). The Cr/Pd bilayer provided oxidation-resistant surfaces while maintaining atomic-scale flatness, critical for STM tip stability during flake characterization.

4. Damage-Mitigated Device Release

LiŌoff utilized inverted 1165 solvent immersion (3hr) to preserve delicate flake-search electrodes, followed by dicing protection via PMMA 495 A4 coatings (2000 rpm, 170°C bake) to reduce edge fractures, with backpolishing to manually remove the insulating SiO₂ layer. Cutting was conducted under a DISCO Dicing saw along predefined lines, and final plasma cleaning employed sequential 200W O₂ strips (Oxford RIE) to remove organics without ion bombardment damage.

Final chips showed >90% electrode integrity (Fig. 2) and have been used for more than 100 STM 2D quantum device making. Reliability validation involved \sim 200 STM_v2 chips processed across two wafer lots, demonstrating functionality in locating 2-10 μ m flakes (Fig. 3), zero registration failures during 2D material transfers, and half a year shelf-life stability (N_2 storage).



Fig. 1: STM v2 mask design showing 3µm alignment markers.

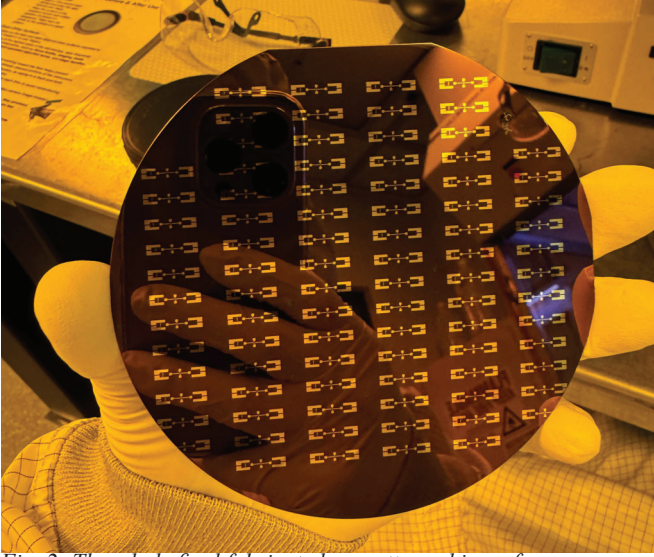


Fig. 2: The whole final fabricated prepattern chip wafer.



Fig. 3: Optical micrograph of a graphene-based 2D device on an STM prepattern chip.

The established process enables reliable fabrication of STM prepatterned chips for microscale 2D flake discovery, achieving >95% yield in registration-critical devices. Future work will extend this methodology to air-sensitive materials (e.g., CrPS₄) via glovebox-compatible integration, requiring conductance-optimized electrodes through testing new electrode categories to minimize conductance reduction and geometric redesign through modifying pad geometries to prevent bonding-induced circuit shorts.

- [1] Li, G., Luican, A., & Andrei, E. Y. Rev. Sci. Instrum. 82, 073701 (2011)
- [2] Liu, X., et al., Science 375, 321-326 (2022)

Sensor Development for Picosecond Timing

CNF Project Number: 321324

Principal Investigator(s): Marina Artuso

User(s): Bridget Mack

Affiliation(s): Department of Physics, Syracuse University

Primary Source of Research Funding: National Science Foundation

Contact: martuso@syr.edu
Website: https://hep.syr.edu/

Primary CNF Tools Used: DISCO Dicing Saw, Westbond 7400A Ultrasonic Wire Bonder

Abstract:

Future particle detectors will require fast timing capabilities to handle the high luminosities planned for collider experiments. Research and development into low gain avalanche diodes is needed to reach resolutions on the order of 10 picoseconds. Multiple fabrication parameters, including implantation energy, thickness, and mask area need to be optimized for sensing large quanties of particles in high radiation environments. Several of these design parameters are being tested, with goals to characterize design parameters of low gain avalanche diodes for precision timing applications in high energy particle detectors. Prototype development is currently underway; the first wafers will be ready within the next six months.

Summary of Research:

The future of particle physics as a field will rely on heavy research and development in instrumentation motivated by the physics goals of the next generation of experiments. Proposed future collider experiments boast higher luminosities, meaning – from a detector standpoint – large influxes of particles and radiation over short timescales. The ability to attach a precise time stamp on the order of 10 picoseconds to position or energy measurements becomes crucial, with broad potential to be transformative not only in particle physics instrumentation, but also in other research areas such as medical imaging [1-3].

Low Gain Avalanche Diodes are good candidates for use in both tracking detectors and hybrid calorimeters including layers with high granularity and timing resolutions. The added gain layer at the junction creates a high electric field, leading to charge multiplication and an amplified signal with a sharp rise time, yielding good

timing resolution [4]. Multiple parameters – including active area, thickness, and gain – must be tailored to the specific granularity, radiation hardness, and acceptance requirements of a given detector system. Ten 4-inch wafers with arrays of silicon sensors are at various stages of production with varying fabrication parameters. Figure 1 shows a rough schematic of the masks used, which include sensors with active areas between 3 and 10 square millimeters.

Manufacture-side delays in wafer productions due to issues with contact metallization have limited production progress, thus limiting facility use. These technical hurdles are now resolved, and no further roadblocks are anticipated. A full set of pre-diced prototypes by the manufacturer are expected within the next six months; some smaller samples and partial wafers are already available and will need to be diced with the DISCO dicing saw. The Westbond 7400A Ultrasonic Wire Bonder has been used for wire bonding some of these samples to printed circuit boards.

Preliminary electrical testing of 3mm and 10mm square pads shows that increasing active area, and thus, capacitance, allows for more current to flow through the device, while the depletion voltage stays the same. Figure 2 shows a current vs voltage characterization curve that compares the two devices. In the coming weeks, the devices will be tested using transient current technique to study the differences in signal formation and to determine spatial and timing resolutions.

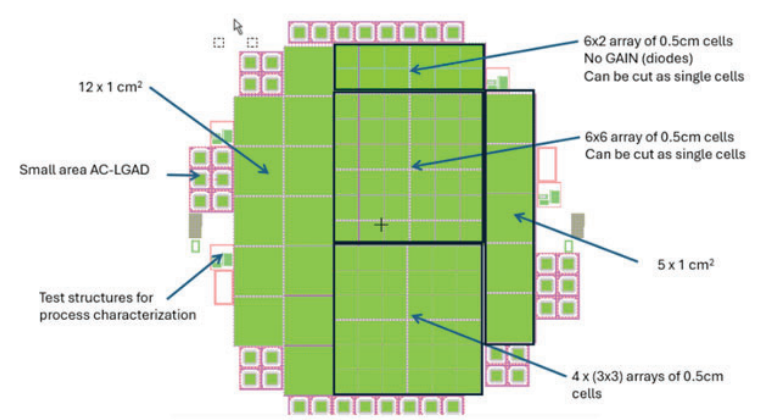


Figure 1: Rough schematic of masks used for wafer fabrication. Each wafer has a set of test structures, as well as diodes and low gain avalanche diodes of different sizes. Pairs of wafers are being fabricated with different implantation energies and epitaxial thicknesses.

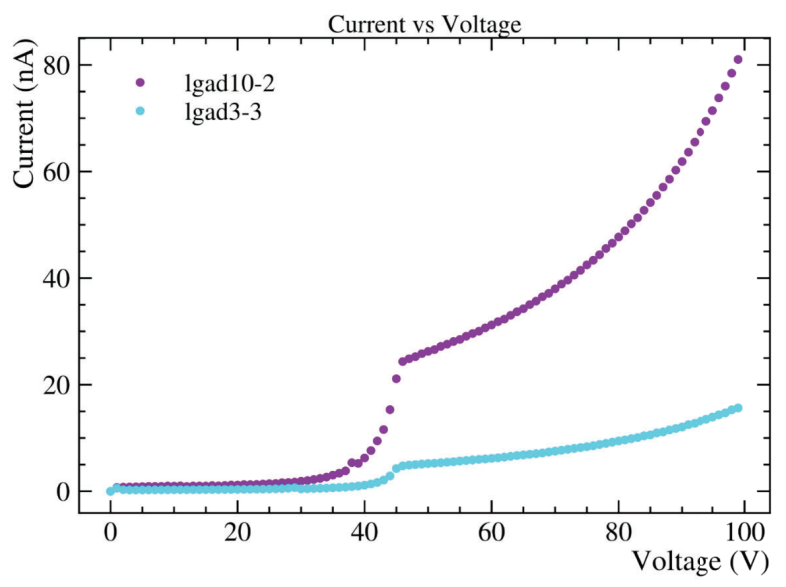


Figure 2: Current vs applied voltage for 10mm (lgad10-2; top curve) and 3mm (lgad3-3; bottom curve) devices. Both low gain avalanche diodes tested are from the same wafer and have the same epitaxial thickness and implantation energy.

As more devices become available, they will be tested before being wire bonded at Syracuse University. For the periods of time in which the Syracuse wire bonder is down, the Westbond 7400A Ultrasonic Wire Bonder will be used. In addition to the prototypes from the manufacturer, several partial wafers from Hamamatsu with standard silicon diodes are being prepped to be diced using the DISCO Dicing Saw. After dicing, they will undergo electrical tests before they are also wire bonded to readout boards for further study. Comparisons between the low gain avalanche diodes and the standard silicon diodes will be made to further explore the capabilities and limitations of solid-state detectors for particle physics applications.

- [1] W. Krüger et al., "Lgad technology for hades, accelerator and medical applications", Nuclear Instruments and Methods in Physics Research Section A: Accelerators, Spectrometers, Detectors and Associated Equipment 1039, 167046 (2022).
- [2] S. Dharani, "Particle Identification using Time of Flight in the International Large Detector ILD", Bachelorarbeit (Universit at Leipzig, 2018), p. 41, https://bib-pubdb1.desy.de/record/414330.
- [3] S. V. Chekanov et al., "Physics potential of timing layers in future collider detectors", JINST 15, P09021 (2020), arXiv:2005.05221 [physics.ins-det].
- [4] A. Apresyan et al., "Measurements of an AC-LGAD strip sensor with a 120 GeV proton beam", JINST 15, P09038 (2020), arXiv:2006.01999 [physics.ins-det].

Fabrication of superconducting qubits at CNF

CNF Project Number: 323724

Principal Investigator(s): Prof. Valla Fatemi

User(s): Simon Reinhardt, Maciej Olszewski, Lingda Kong, Gabriele Di Gianluca

Affiliation(s): Cornell Applied and Engineering Physics (AEP)
Primary Source of Research Funding: Nordtech (SQFAB)

Contact: vf82@cornell.edu

Website: https://fatemilab.aep.cornell.edu/

Primary CNF Tools Used: Angstrom-Q, JEOL 6300, Zeiss Ultra SEM, AJA-Q

Abstract:

We demonstrate fabrication of superconducting qubits using CNF tools. Josephson junctions of Dolan and Manhattan type are defined using shadow masks. Evaporation and in-situ oxidation are performed using the Angstrom Quantum evaporator.

Summary of Research:

The objective of this project is to demonstrate fabrication of state-of-the-art superconducting qubits at CNF. We fabricate transmon qubits on base layers of tantalum thin films on 100mm highly resistive silicon wafers. The fabrication of the tantalum base layer structures is covered in a separate report.

The main step in the fabrication of superconducting qubits is the deposition of Josephson junctions (JJs). The JJs are fabricated using shadow evaporation and liftoff. In a first step the shadow masks are defined using electron beam lithography (JEOL 6300) in a bilayer resist stack (MMA/PMMA). Using the JEOL6300 ebeam writer we perform lithography on 100mm wafers. The ebeam writer allows loading of two 100mm wafers for each writing session.

We demonstrate both Dolan-type JJs (Fig. 1) which use a suspended PMMA bride as well as Manhattan-type JJs without a suspended bridge (Fig. 2). Initially we used the AJA-Q evaporator for the deposition of Dolan-type JJs providing superconducting qubits with highly promising characteristics.

As part of the CNF-REU summer project we characterized the new Angstrom-Q tool, which is dedicated for the fabrication of Josephson junctions for superconducting qubits (REU student Gabriele Di Gianluca). The Angstrom-Q provides several benefits for the fabrication of JJs:

- fully programmable recipes, high degree of automation
- precise alignment of stage rotation and tilt, ideal for shadow deposition
- in-situ argon ion milling and oxygen plasma descum
- evaporation of ultra-clean aluminum films directly from the copper hearth, without graphite crucibles
- low base pressure p < 1e-8 torr after chamber baking and titanium gettering
- both static and dynamic in-situ oxidation with a tunable Ar/O2 pressure settings

After deposition the fabrication is finalized by a liftoff in a hot solvent. The JJs can be characterized at room temperature using a probe station. After optimization of the recipes in the REU project we obtain resistance variations as low as 2% over single dies. The JJs can be imaged using the Zeiss Ultra SEM, see images Fig. 1 and Fig. 2 below.

Acknowledgement:

Funding (or Partial funding) for shared facilities used in this prototype was provided by the Microelectronics Commons Program, a DoD initiative, under award number N00164-23-9-G061.

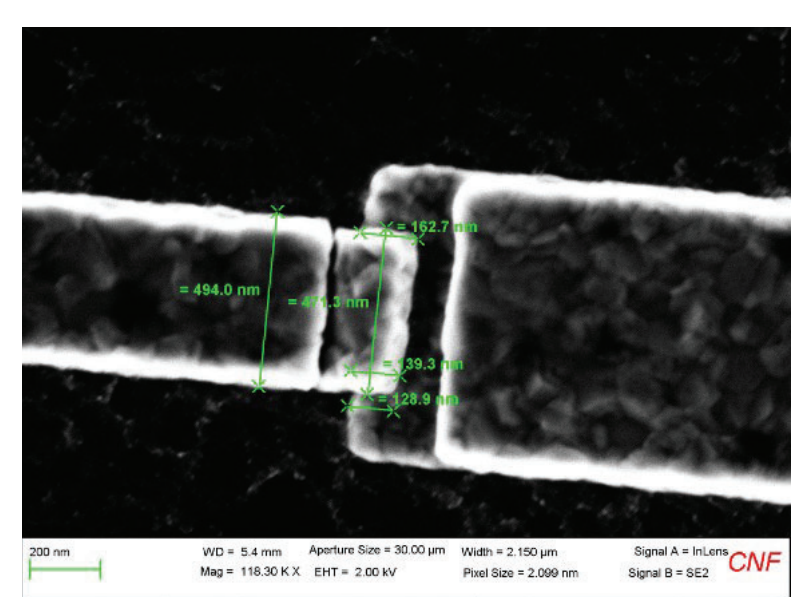


Figure. 1: Dolan-type Josephson junction. This type of junction uses a suspended bridge formed by electron beam lithorgaphy in MMA/PMMA resist. The evaporation of aluminum electrodes and in-situ oxidation is performed in the newly installed Angstrom-Q evaporator.

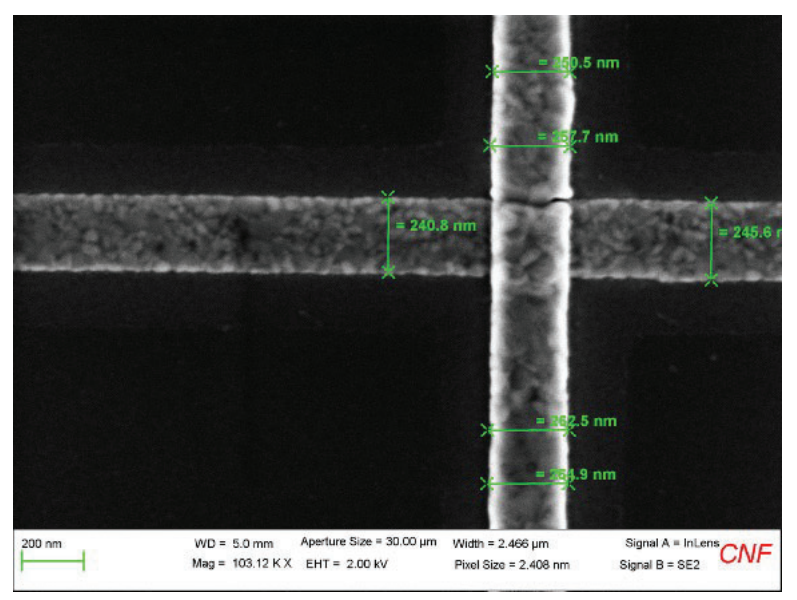


Figure. 2: Manhattan-type Josephson junction with an area of 250nm x 250nm. Lithography of the shadow mask is performed using the JEOL 6300 ebeam writer. The evaporation of aluminum electrodes and in-situ oxidation is performed in the newly installed Angstrom-Q evaporator.

Study of vortex dynamics in Josephson junction arrays

CNF Project Number: 326525

Principal Investigator(s): Katja Nowack

User(s): Cequn Li

Affiliation(s): Laboratory of Atomic and Solid State Physics, Cornell University

Primary Source of Research Funding: US Department of Defense

Contact: kcn34@cornell.edu

Website: https://nowack.lassp.cornell.edu/

Primary CNF Tools Used: JEOL JBX-6300FS, Heidelberg MLA 150 Maskless Aligner, Angstrom E-Beam Evaporator,

AJA sputter, Zeiss Ultra SEM, Zeiss Supra SEM, Glen 1000 Resist Strip

Abstract:

An array of superconducting islands deposited on a normal metal film forms the so-called Josephson junction arrays, providing a tunable platform for studying quantum critical phenomena. This system enables the investigation of competing vortex states and the phase transitions [1-4]. Here, we fabricate Nb-Au Josephson junction arrays and study vortex dynamics by combining electrical transport measurements and scanning superconducting quantum interference device microscopy. Our preliminary data shows the presence of periodic vortex lattice formed in the square and hexagonal arrays. Experiments on the vortex dynamics driven by an external current will be studied.

Summary of Research:

We fabricated Nb-Au Josephson junction arrays (JJA) and studied the formation of periodic Josephson vortex lattices using electrical transport measurements and scanning superconducting quantum interference device (SQUID) microscopy at low temperatures. Figure 1 illustrates the process to fabricate Nb-Au JJAs. First, we patterned Au/Ti (40/5 nm) films on Si substrates using optical lithography and electron-beam evaporations. Then we performed electron-beam lithography and sputtered Nb/Ti (70/2 nm) on the pre-patterned Au/Ti. Figure 2 shows an optical image of an exemplary Nb-Au square JJA device. The Nb islands are only connected by the underneath Au films, forming superconductornormal metal-superconductor networks.

The JJAs were characterized by low-temperature transport measurements. We confirmed the JJAs are superconducting with the critical temperatures ranging between 5 K and 7 K. Furthermore, we observed maxima in the critical currents as a function of the external magnetic fields, indicating the formation of

periodic vortex lattices [2]. We also performed scanning SQUID measurements to visualize the vortex lattices at different magnetic fields.

Conclusions and Future Steps:

We successfully fabricated Nb-Au JJAs with the critical temperatures ranging between 5 K and 7 K. Through electrical transport measurements and scanning SQUID microscopy, we detected the presence of vortex lattice in the JJAs, leading to enhancements of the critical currents at specific magnetic fields. We will visualize the motion of vortices driven by an external current for the understanding of the vortex dynamics [3, 4].

- [1] S. Teitel and C. Jayaprakash, Josephson-junction arrays in transverse magnetic fields, Phys. Rev. Lett. 51, 1999 (1983).
- [2] N. Poccia, T. I. Baturina, F. Coneri, et al., Critical behavior at a dynamic vortex insulator-to-metal transition, Science 349, 1202 (2015).
- [3] C. Bøttcher, F. Nichele, M. Kjaergaard, et al., Superconducting, insulating and anomalous metallic regimes in a gated two-dimensional semiconductor–superconductor array. Nat. Phys. 14, 1138–1144 (2018).
- [4] C. Bøttcher, F. Nichele, J. Shabani, et al., Dynamical vortex transitions in a gate-tunable two-dimensional Josephson junction array, Phys. Rev. B 108, 134517 (2023)

1. E-beam deposit 40nm Au/5nm Ti Au Ti SiO₂/Si

Figure 1: Schematics of fabrication process of Nb-Au Josephson junction arrays.

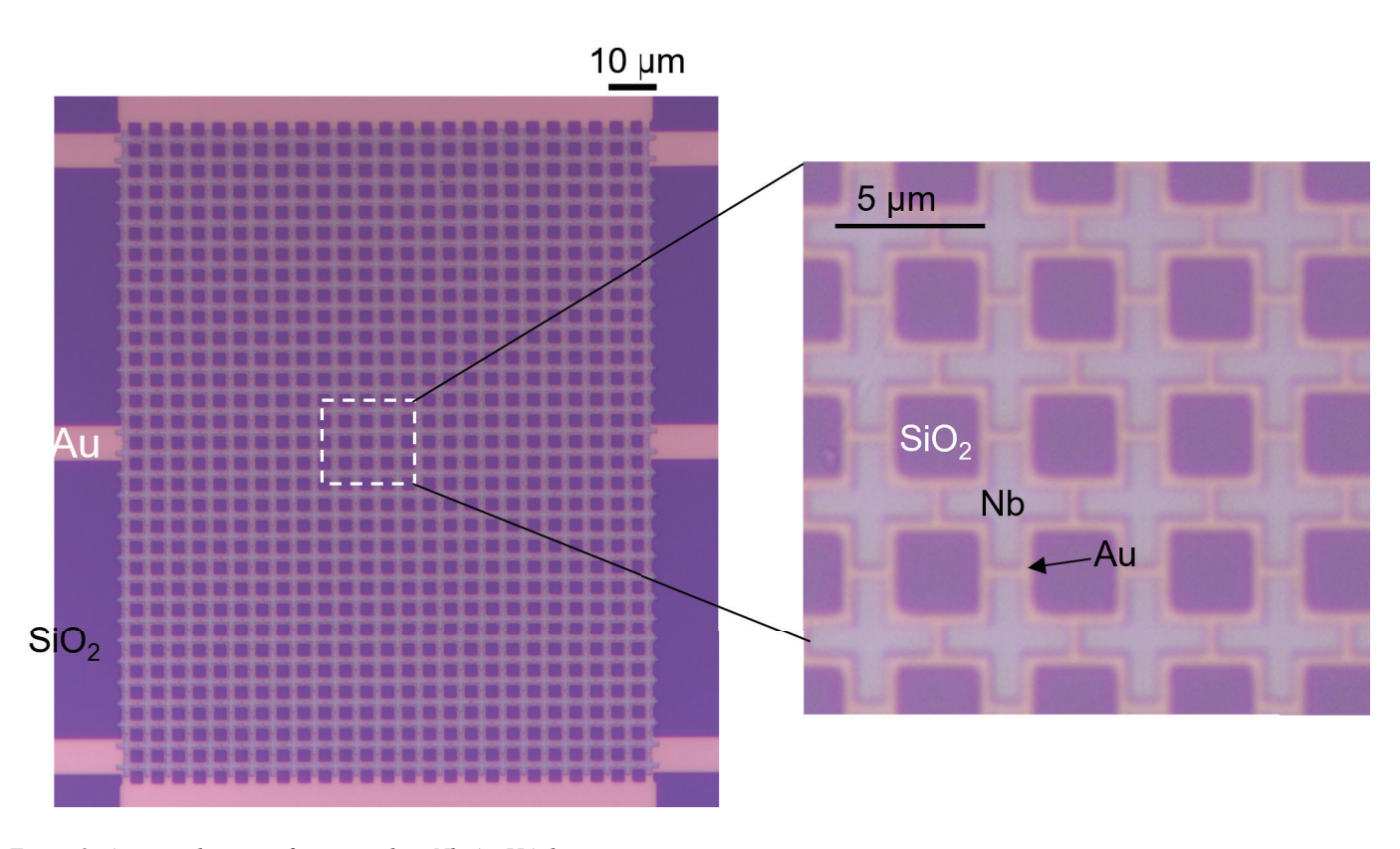


Figure 2: An optical image of an exemplary Nb-Au JJA device.

Silicon Carbide Nanophotonic Cavities for Integration with Color Centers

CNF Project Number: E718638

Principal Investigator(s): Greg Fuchs

User(s): Ying Yang

Affiliation(s): School of Applied and Engineering Physics, Cornell University

Primary Source of Research Funding: NSF

Contact: gdf9@cornell.edu

Primary CNF Tools Used: Oxford COBRA, Oxford 81 Etcher, JEOL 6300, Nabity, Dicing saw -- Disco, Glen 100, CVC

SC4500 Odd hour Evaporator, Zeiss Supra SEM, Zeiss Ultra SEM, LPCVD HTO & LTO

Abstract:

Silicon carbide (SiC) has emerged as a promising platform for quantum photonics due to its excellent material properties and intrinsic color centers. We demonstrate the fabrication of two complementary cavity architectures in SiC: plasmonic silver nanopan cavities and dielectric ring-waveguide resonators on SiC-on-insulator (SiCOI). These structures are designed to provide cavity modes with field confinement and high-quality factor. The cavity modes are coupled with SiC color centers to enhance collection efficiency and emission rate through the Purcell effect. We report significant advances in addressing fabrication challenges including sidewall tapering through optimized e-beam lithography using dual PMMA layers and refined etching recipes.

Summary of Research:

Silicon carbide hosts optically addressable spin defects that exhibit excellent quantum properties, including long spin coherence times (>1 ms) and nearinfrared emission compatible with telecommunication infrastructure (1,2). However, the collection efficiency of photons from these color centers is limited by their low Debye-Waller factor (5% for divacancies) and the high refractive index of SiC (n = 2.6), which causes most emitted light to undergo total internal reflection. Photonic cavities can overcome these limitations through Purcell enhancement, increasing both the emission rate and the fraction of photons collected into desired optical modes (3,4). Here, we develop two cavity platforms that leverage different enhancement mechanisms: plasmonic nanopan cavities offering ultrasmall mode volumes and dielectric ring resonators on insulator providing high quality factors.

For the plasmonic nanopan cavity fabrication in Figure 1, we begin with 8×8 mm pieces of 4H-SiC. Prior to any fabrication steps, samples undergo thermal annealing at

650°C in vacuum for 1 hour to remove inherent defects and damage. The process is given in Figure 1. It first employs electron beam lithography with a bilayer resist structure consisting of 220 nm PMMA 495 A4 (spun at 1600 rpm) and 120 nm PMMA 950 A4 (spun at 6000 rpm) to create undercut profiles that mitigate sidewall angles, and each baked at 170°C for 15 minutes. An e-spacer layer (~25 nm) is applied without baking to prevent charging. Circular patterns with diameters ranging from 200-800 nm are exposed using a Nabity at 10kV with doses of 400-850 μC/cm². After development in 1:3 MIBK:IPA for 60s, we deposit 100 nm of nickel using the CVC SC4500 evaporator at 1.3 Å/s with intermittent cooling (20 nm deposition followed by 77s pause). Lift-off is performed in acetone overnight, followed by 5s brief ultrasonication.

The etching process utilizes Oxford COBRA ICP-RIE with an SF \square /O \square chemistry (30:15 sccm) at 2000W/40W and 8 mTorr pressure, achieving an etch rate of ~5.5 nm/s. We address the sidewall taper issue by utilizing the undercut profile from the PMMA495/PMMA950 bilayer, which provides better pattern transfer fidelity compared to MMA/PMMA495 bilayer in our previous recipe. After etching to depths of 400 nm, the nickel mask is removed using Type 1 nickel etchant at 40°C for 10s. The SiC nanopillars are then encapsulated with 500 nm of silver deposited by CVC SC4500 evaporator, creating the plasmonic cavity structure. The devices (Figure 2a-d) demonstrate strong out-of-plane field confinement in FDTD simulations in Figure 2e, enabling the efficient coupling to c-axis oriented VSi dipoles and realizing photoluminescence enhancement (5).

For the SiCOI ring-waveguide resonators in Figure 3, we use commercially available 4H-SiCOI pieces with 540 nm SiC, 3044 um SiO2 and 680 µm Si layers (6). The fabrication is given in Figure 3. It first employs the same dual PMMA resist approach. To remove the edge

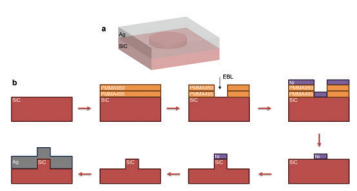


Figure 1: (a) Schematic of the SiC nanopan cavities. (b) Fabrication process flow for SiC nanopan cavities showing resist deposition, e-beam lithography, metal deposition, etching, and silver encapsulation steps.

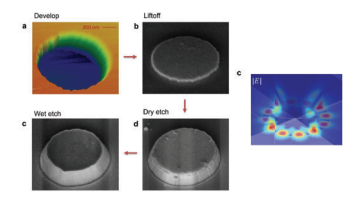


Figure 2: (a) AFM and SEM image of the fabricated SiC nanopan cavities of developing the resist, liftoff Ni mask, dry etching the SiC, wet etching the Ni mask. (b) FDTD simulation of SiC nanopan cavity's E field profile showing the whispering gallery mode TM12,0,0 the field concentration at SiC-silver interface. (c) Photoluminescence spectrum from silver nanopan cavity (red) compared to bare SiC substrate (black), showing enhancement of V1 and V1' emission lines around 860 nm.

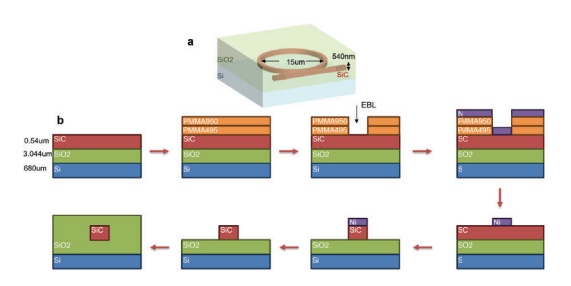


Figure 3: a) Schematic of the SiCOI ring-waveguide-grating devices. (b) Fabrication process flow for SiCOI ring-waveguide-grating devices showing resist deposition, e-beam lithography, metal deposition, etching, and silica cladding steps.

beads on the 5×5 mm SiCOI pieces, the sample piece is bond to the center of a dummy wafer and a dummy piece is bond side by side. Ring resonators with radii of $10\text{-}20~\mu\text{m}$, waveguide width of 300-500~nm and grating couplers with of 2 μm width, 50% duty cycle and 420~nm pitch (7,8), are patterned by JEOL 6300 system in 10nA 60nm aperture with doses of $300\text{-}500~\mu\text{C/cm}^2$. We deposit 100~nm nickel masks with the same duty-cycled evaporation to minimize thermal stress. The etching recipe was optimized to reduce the taper by adjusting SF_6/O_2 to 30:10~sccm.

The fabricated ring resonators exhibit smooth sidewalls. Coupling gaps of 300-700 nm between the ring and bus waveguides are achieved with good uniformity, to guarantee the critical coupling. After nickel mask removal, we deposit a SiO2 cladding layer using a two-step LPCVD process: first, 600 nm of high-temperature

oxide (HTO) deposited at 1.5 nm/min to conformally cover the etched structures and fill narrow gaps, followed by 2 μ m of low-temperature oxide (LTO) at 10 nm/min to provide a thick upper cladding for mode confinement and environmental protection. In Figure 4, preliminary transmission simulations show whispering gallery modes $TM_{m,0,0}$ with high quality factors due to the large refractive index mismatch of SiC and SiO2 layers. The grating coupler's simulated transmission gives a broad stop band centered at 860 nm close to V1 centers in SiC, which can provide good injection and reading of laser beam into the device.

Conclusions and Future Steps:

We have demonstrated two complementary approaches for creating photonic cavities in silicon carbide: plasmonic nanopan structures and SiCOI ring resonators for maximum field enhancement and high-Q operation. The optimized dual PMMA resist system and refined etching processes effectively address the sidewall taper challenges for us to tune the device performance. Future work will focus on precise spectral and spatial alignment of color centers with cavity modes through controlled ion implantation after cavity fabrication. We plan to perform detailed Purcell factor measurements using time-resolved photoluminescence and explore coherent control of cavity-coupled spins. Additionally, we will investigate hybrid integration approaches combining the high field enhancement of plasmonic structures with the low loss of dielectric cavities to approach the strong coupling regime necessary for deterministic quantum gates.

- [1] Castelletto, S. et al. Nat. Mater. 21, 67-73 (2022)
- [2] Lukin, D. et al. Nat. Photonics 14, 330-334 (2020)
- [3] Castelletto, S. et al. ACS Photonics, 9, 1434-1457 (2022)
- [4] Ou, H. et al. Materials, 16, 1014 (2023)
- [5] So, J. P. et al. Nano Letters, 24, 11669-11675 (2024).
- [6] Yi, A. et al. Optical Materials, 107, 109990 (2020).
- [7] Lukin, D. et al. arXiv preprint, 2504, 09324, (2025).
- [8] Afridi, A. A. et al. Applied Physics Letters, 124 (2024).